

DEVELOPMENT OF HIGH-ACCURACY VIDEO MICROSCOPY-BASED  
SUBCELLULAR TRACKING IN CHARACTERIZING CELLULAR DYNAMIC  
PROCESSES

By

PEI-HSUN WU

A DISSERTATION PRESENTED TO THE GRADUATE SCHOOL  
OF THE UNIVERSITY OF FLORIDA IN PARTIAL FULFILLMENT  
OF THE REQUIREMENTS FOR THE DEGREE OF  
DOCTOR OF PHILOSOPHY

UNIVERSITY OF FLORIDA

2010

© 2010 Pei-Hsun Wu

To my wife and my family

## ACKNOWLEDGMENTS

I would like to thank my advisor, Dr. Yiider Tseng, for his guidance and support. He has consistently provided me with valuable professional and personal advice and has always guided me to work successfully. I deeply appreciate all the opportunities he has offered to me. I am also thankful for my graduate study committee members, Dr. Richard Dickinson, Dr. Tanmay Lele, and Dr. Edward Chan for their valuable experience and expertise that has helped me to finish my work.

I would like to express my special thanks to all of my group members for their great assistance in many ways, Dr. Hengyi Xiao, Wei Cheng, Shen-Hsiu Hung, Sinan Dag, and Patrick Burney. Many thanks also go to James Hinnant, and Dennis Vince for their help in equipment maintenance. Special thanks to Mr. Stephen Hugo Arce for helping to prepare my dissertation.

Finally, I want to thank my wife, Yun-Ting Hung, my parents, and my other family members for their love and great support in these years.

This dissertation could not have been accomplished without the help of so many. I truly appreciate everyone.

# TABLE OF CONTENTS

	<u>page</u>
ACKNOWLEDGMENTS.....	4
LIST OF TABLES.....	8
LIST OF FIGURES.....	9
LIST OF ABBREVIATIONS.....	11
ABSTRACT.....	12
CHAPTER	
1 INTRODUCTION.....	14
1.1 Motivation.....	14
1.1.1 Video-Based Particle Tracking and Mean Square Displacement.....	14
1.1.2 Electron-Multiplying CCD.....	15
1.1.3 Optimum Estimate of the True Trajectory among Noise.....	16
1.1.4 Nuclear Architecture and Gene Regulation.....	18
1.2 Study Outline.....	19
2 A METHOD TO ACHIEVE HIGH ACCURACY MICRORHEOLOGY.....	21
2.1 Background.....	21
2.2 Material and Methods.....	23
2.2.1 Preparation of Glycerol Samples with Embedded Fluorescent Particles.....	23
2.2.2 Microscope and CCD Acquisition System.....	23
2.2.3 Particle Tracking Algorithm.....	24
2.2.4 Mean Square Displacement.....	25
2.2.5 Extracting the Noise Amplitude and Estimating the Mean Signal Intensity.....	25
2.2.6 Monte Carlo Simulation.....	26
2.2.7 Rheometer.....	28
2.2.8 Intracellular Particle Tracking and Cytoplasmic Rheology.....	28
2.3 Results.....	29
2.3.1 Light Source Affects the MSD Values.....	29
2.3.2 Interplay of Several Factors Determines the Static Error.....	31
2.3.3 Direct Parameter-Mapping can be used to Accurately Estimate the Static Error.....	33
2.3.4 Procedure Verification using <i>in vitro</i> and <i>in situ</i> Experimental Systems ..	35
2.3 Discussion.....	37
2.4 Conclusion.....	39

3	A GENERAL METHOD FOR IMPROVING SPATIAL RESOLUTION BY OPTIMIZATION OF ELECTRON MULTIPLICATION IN CCD IMAGING.....	47
3.1	Background.....	47
3.2	Methods and Results .....	49
3.2.1	The EM Gain can Influence Quantitative Image Analysis.....	49
3.2.2	EM Gain Characterization .....	50
3.2.3	The Signal to Noise Ratio (SNR) can be used to Optimize the EM Gain Setting .....	54
3.2.4	EM Gain Effects on Multi-Pixel Analysis.....	55
3.2.4.1	Optimal EM Gain Depends on the Size and Background Intensity of the Object.....	57
3.2.4.2	Particle Tracking Experiments Verify the EM Gain Effect on Image Analysis .....	58
3.3	Discussion .....	59
3.3.1	The Working Range and Effectiveness of EM Gain.....	59
3.3.2	Analysis of the Estimated Values in this Study.....	60
3.3.3	Assessment of EM Gain in Subcellular Particle Tracking Experiments ...	60
3.3.4	Application of Proper EM Gain to Biophysical Measurements beyond Particle Tracking .....	61
3.5	Conclusion.....	63
4	ANALYSIS OF VIDEO-BASED MICROSCOPIC PARTICLE TRAJECTORIES USING KALMAN FILTERING .....	70
4.1	Background.....	70
4.2	Theory of Kalman Filtering in Particle Tracking .....	72
4.2.1	The Parameters of the Kalman Filter Related to a Particle Tracking Trajectory .....	72
4.2.2	The Kalman Filter Gain is Determined by the Ratio $Q/R$ but not $Q$ or $R$ ..	75
4.2.3	MSD Estimates from a Filtered Trajectory are Equal to the True State ...	77
4.3	Materials and Methods.....	78
4.3.1	Application of the Kalman Filter to Simulated Trajectories .....	78
4.3.2	Microscopic Particle Tracking System.....	79
4.3.3	Particle Tracking Experiments in Glycerol Solutions .....	79
4.3.4	Particle Tracking Experiments in Gliding Motility Assays .....	79
4.4	Results.....	80
4.6	Discussion .....	86
4.7	Conclusion .....	89
5	CHARACTERIZATION OF THE NAC-1 NUCLEAR BODY DYNAMICS AND CHROMATIN ASSOCIATION.....	96
5.1	Background.....	96
5.2	Methods and Results .....	98
5.2.1	Characterization of NAC-1 NB in nucleus.....	98
5.2.2	Typical Motion of NAC-1 NB in Nucleus .....	100

5.2.3 NAC-1 NB Dynamics Relates to the Chromatin Architecture and ATP Level .....	103
5.3 Discussion and Conclusion.....	107
6 CONCLUSIONS .....	116
6.1 Accurate MSD Estimation in Video-Based Tracking .....	116
6.2 Optimizing Image Acquisition.....	116
6.3 Optimum Estimation of Biophysical Properties .....	117
6.4 Dynamics of Nuclear Organelles Associated with Chromatin Structure.....	117
LIST OF REFERENCES .....	119
BIOGRAPHICAL SKETCH.....	128

## LIST OF TABLES

<u>Table</u>		<u>page</u>
3-1	List of sections contain The values of the effective EM gain (k), excess factor ..	64
3-2	List of sections contain The values of the effective EM gain (k), excess factor (F), intensity offset ( $I_{offset}$ ), and relative working range at several EM gain settings estimated for experimental system.....	64

## LIST OF FIGURES

<u>Figure</u>	<u>page</u>
2-1	The mean square displacement (MSD) is correlated to the peak intensity ( $I'$ ) of microspheres tracked by a charge-coupled device (CCD) camera..... 41
2-2	Static error ( $2\varepsilon^2$ ) can be estimated using simulated Gaussian beads..... 42
2-3	The method to relate extracted static error from simulated beads to experimental microsphere images is demonstrated.. ..... 43
2-4	A Gaussian bead with the parameters determined by the mapping procedure in this paper can represent the experimental microsphere. .... 44
2-5	Static error can be corrected for the MSD of microspheres embedded in glycerol..... 45
2-6	Static error can be corrected for the MSD of 100-nm carboxylated polystyrene particles embedded in MC3T3-E1 fibroblast cells under red-fluorescence.. ..... 46
3-1	EM gain causes contradictory effects on the spatial resolution of protein clusters. .... 65
3-2	EM gain parameters are determined experimentally. .... 66
3-3	The optimal setting of the EM gain depends on the intensity of the signal.. ..... 67
3-4	The relation of the $k$ and $\varepsilon_s$ is affected by $I_{peak}$ ..... 68
3-5	The EM gain performance in particle tracking depends on experimental conditions. .... 69
3-6	Plot of $\varepsilon_{S,1000}$ vs. $\varepsilon_{S,0}$ ..... 69
4-1	Schematic illustration of the principle of Kalman filter in estimating the accurate trajectory in a cellular dynamic process. .... 90
4-2	Estimation of the true trajectory from positioning errors using Kalman filter. .... 91
4-3	Schematic illustration of the procedure of implementing Kalman filter into a microscopic particle tracking system to improve the spatial resolution..... 92
4-4	Characterization of the performance of Kalman filter on estimating particle tracking trajectories. .... 93
4-5	Improving the positioning error of particle tracking in glycerol solution..... 94

4-6	Improving the positioning error of particle tracking in gliding motility assays using Kalman filter. ....	95
5-1	Fixed and stain images show the location of NAC-1 NB in a nucleus.. ....	109
5-2	Dynamics structure of NAC-1 NBs was analyzed by Fluorescence recovery after Photobleaching.....	110
5-3	Characterize the NAC-1 NB dynamics from their MSD response.....	111
5-4	A vector map shows the NB Movement over three different time scale, 0.1s, 1s and 5s (from top to bottom).....	112
5-5	Reconstructed NAC-1 NB image. ....	112
5-6	NAC-1 NB mobility is associated with its size.....	113
5-7	Drug treatment affects NAC-1 NB kinetics.. ....	114
5-8	MSD plots show the NAC-1 NB dynamics over time in response to drug treatment.. ....	115

## LIST OF ABBREVIATIONS

ActD	Actinomycin D
ACF	Auto correlation function
CCD	Charge-coupled device
EMCCD	Electron-multiplication CCD
ICCD	Intensified CCD
LatB	Lactrunculin B
MSD	Mean square displacement
MT	Microtubule
NB	Nuclear body
NOC	Nocodazole
PMT	Photon-multiplication tube
ROI	Region of interest
SNR	Signal noise ratio

Abstract of Dissertation Presented to the Graduate School  
of the University of Florida in Partial Fulfillment of the  
Requirements for the Degree of Doctor of Philosophy

DEVELOPMENT OF HIGH-ACCURACY VIDEO MICROSCOPY-BASED  
SUBCELLULAR TRACKING IN CHARACTERIZING CELLULAR DYNAMIC  
PROCESSES

By

Pei-Hsun Wu

May 2010

Chair: Yiider Tseng  
Major: Chemical Engineering

Video-based particle tracking monitors the microscopic movement of labeled biomolecules, subcellular organelles and fluorescent probes within a complex cellular environment. Measurements obtained by this technique, mainly the mean square displacement (MSD) of the tracers, enable us to extract the dynamic information of subcellular processes and the intracellular mechanical properties. However, MSD measurements are highly susceptible to static error introduced by noise in the image acquisition process that leads to an incorrect positioning of the particle. An approach that greatly increases the accuracy of MSD measurements is developed herein by combining experimental data with Monte Carlo simulations. In addition, the trajectories obtained from video-based particle tracking can provide insight into transient subcellular transportation such as endocytosis. In this work, it is shown that the Kalman filter, a robust algorithm to estimate the state of a linear dynamic system from noisy measurements, can be applied to particle tracking to dramatically reduce positioning error while retaining the intrinsic fluctuations of a cellular dynamic process. Hence, the Kalman filter can serve as a powerful tool to infer a trajectory of ultra-high fidelity from

noisy images, revealing the details of dynamic cellular processes. Finally, the short time dynamics of NAC-1 nuclear bodies (NB) are measured to study their interactions with chromatin since the chromatin architecture is suspected to be highly associated with gene regulation. I demonstrate that the dynamics of NAC-1 NBs are determined by these associations with chromatin as well as the organization of the chromatin structure through the utilization of the developed high accuracy particle tracking analysis method.

## CHAPTER 1 INTRODUCTION

### 1.1 Motivation

#### 1.1.1 Video-Based Particle Tracking and Mean Square Displacement

Video-based particle tracking monitors the real-time motion of tracer particles. The mean square displacement (MSD) of these tracer particles may be used to interpret cellular biophysical properties, including the diffusivities of lipid membrane and transmembrane proteins<sup>1,2</sup>, intracellular mechanics<sup>3,4</sup> and the dynamics of chromatin and nuclear bodies<sup>4-10</sup>. However, as more confined spaces are probed with higher temporal resolution, the ability of particle tracking to perform with consistent accuracy is diminished by an inherent measurement error<sup>11,12</sup>. For example, when imaging with a charge-coupled device (CCD) camera, the noise can fluctuate between individual pixels within tracking frames causing a positioning error. This error will propagate as static error to affect the accuracy of MSD analysis because the MSD is calculated from a particle's displacement<sup>12-14</sup>.

The characteristics of static error have been previously discussed from a theoretical perspective<sup>11-13</sup>. Webb's group investigated the magnitude of positioning error as a function of the number of detected photons and the spot size, demonstrating that the most reliable results stem from brighter, well-defined particles<sup>13</sup>. In their studies, a formula was derived to calculate the spatial resolution. This formula enables a quick estimation of the spatial resolution with approximately 70% accuracy when compared to their own experimental results from tracking immobilized particles<sup>13</sup>. The resolution of tracking is related to the appearance of particles in images, which is determined by factors including focal plane position and the morphology of a tracer.

Even while tracking the same size of beads, the static error of each probe in an image will be different as a result of their z-distance to the focal plane. Therefore, a method to precisely extract static error for each tracked particle *in situ* will greatly advance this technique, providing a way to estimate a more accurate MSD by the removal of the static error individually.

In chapter 2, a new approach is developed to accurately quantify static error. Using a Monte Carlo approach incorporated with experimental imaging noise, the resolution of each individual tracer is successfully estimated. An advantage of this strategy is that it solely relies on experimental outcomes, bypassing the details of complicated tracking algorithms and the various hardware specifications of tracking systems<sup>12, 13, 15</sup>. More importantly, this method significantly improves the resolution of particle tracking experiments, greatly reducing ambiguities and potential errors in the interpretation of experiments.

### **1.1.2 Electron-Multiplying CCD**

In modern microscopic systems, the most common and economical device adopted as a photon detector is the charge-coupled device (CCD) camera, which can simultaneously sense the intensity profile of light emitted from objects within the visual field of the microscope using more than one million parallel arrays. With this device, cell images with detailed information can be captured and later analyzed. However, the performance of the CCD camera drops quickly with a decreasing of photon signal<sup>16</sup>, and, as a consequence, significantly reduces the accuracy of low intensity subcellular measurements in a condition such as single molecule fluorescence imaging. Through the use of much more expensive avalanche photodiode detectors (APD) or photomultiplier tubes (PMT)<sup>17, 18</sup> to acquire images, the resolution of low intensity

measurements can be greatly improved; however, these types of detectors do not have large numbers of individual sensing units in contrast with the parallel array of the CCD camera. When acquiring information from the visual field of the microscope, an APD or a PMT sensor uses a scanning mode, which is usually much slower than the CCD camera. Hence, if the spatial resolution of low intensity images in a CCD camera can be improved, the CCD camera becomes the best choice of camera due to its accessibility and high acquisition rate.

Several intensity-enhanced techniques have been developed to obtain high contrast images from low intensity signals such as intensified CCD (ICCD) and electron multiplying CCD (EMCCD)<sup>16</sup>. The new generation of EMCCD camera has outperformed the ICCD and become a popular choice for imaging the dynamics of single molecules in cells<sup>19, 20</sup>. EMCCD utilizes several specialized extended serial registers on the CCD chip to apply a high voltage and produce multiplying gain through the process of impact ionization in silicon<sup>21</sup>. This capability to elevate the photon-generated signal above the readout noise of the device even at high frame rates has made it possible to meet the need for ultra-low-light imaging applications without the use of external image intensifiers. In Chapter 3, a general quantitative method is developed for optimizing the EMCCD performance in the measurement of biophysical parameters including the single particle tracking.

### **1.1.3 Optimum Estimate of the True Trajectory among Noise**

Cellular and subcellular dynamics control cell physiology<sup>22, 23</sup>. These dynamic processes include not only protein diffusion and transport but also the motion of intracellular organelles<sup>22, 24</sup>. The invasion process of bacteria into the intracellular regions of mammalian cells has also been discovered to involve in the intracellular

dynamics of the host cells <sup>25</sup>. Therefore, the dynamic processes play a critical role in understanding the molecular mechanisms of a subcellular event and should not be ignored. The most direct way to study a cellular dynamic process is to monitor the motion of the observed object, and to further correlate this physical motion to the biochemical functions of the composed biomolecules of the object. For example, the analysis of the step size of the motor protein-driven transport cargoes led to the understanding of how the motor proteins function <sup>26-29</sup>. The connection between the bacteria motion and the function of the bacterial protein, ActA, elucidates how bacteria move inside the host <sup>30, 31</sup>. In these studies, particle tracking serves as the most direct technique for studying the real time movement of objects in live cells.

Particle tracking has been applied to study various subcellular events, such as the genomic dynamics <sup>32</sup>, viral infection <sup>33, 34</sup>, cellular endocytosis <sup>35</sup>, membrane protein trafficking <sup>36</sup>, and cargo transport <sup>37</sup>. Besides the studies of dynamic events in a live cell, particle tracking is also applicable to probe the mechanical properties of the intracellular region of the live cells via particle tracking microrheology <sup>38</sup>, which analyzes the dynamic fluctuation of displacement of an inert particle embedded in the cytoplasmic region of a live cell. Through the microrheology theorem <sup>39, 40</sup>, the rheological parameters of a cell, such as creep compliance, elastic modulus, and viscous modulus, can be explored <sup>38, 41</sup>. Compared to other existing techniques, such as atomic force microscopy, intracellular microrheology introduces minimal perturbation to acquire the physical properties of the intracellular region of the cells. Using this technique, the mechanical properties of various cell lines under different extracellular stimuli (chemical <sup>41</sup> and mechanical <sup>42</sup>) and micro-environmental topology (two-dimensional vs. three-

dimensional <sup>43</sup>) have been probed. The motion from objects can contribute valuable insights into many biological events, and the accuracy of trajectory from particle tracking is critically important for the effectiveness of those studies.

In the system and control field, the theory to estimate an appropriate state of a dynamic system from noisy measurements is well-established. In particular, the Kalman filter algorithm provides the optimal state estimate for linear dynamic systems in the presence of Gaussian noise generated from measurements. The Kalman filter has been successfully applied to wide variety in engineering and science fields <sup>44, 45</sup>, And the potential use of a Kalman filter to study cell motion has been mentioned in the past <sup>46</sup>. In Chapter 4, I explore in detail the application of the Kalman filter algorithm to improve the estimation of the particle trajectory obtained from a microscopic particle tracking experiment.

#### **1.1.4 Nuclear Architecture and Gene Regulation**

The accomplishments of several genome projects provide great insights into the genomics and nuclear architecture <sup>47-49</sup>. However, the regulatory mechanism of a gene is not solely determined by the genome sequence <sup>49-51</sup>. For example, the DNA-protein complex, chromatin, can pack into multiple levels of condensed states through DNA-associated proteins, which are believed to be associated with the gene regulation <sup>50, 52</sup>. In addition, the cell nucleus also features several distinct architectures and functional compartments, including the nucleoli, PML bodies, Cajal bodies, nuclear speckles and lamina <sup>53-55</sup>. Since the transcription process requires a protein complex to interact to the gene <sup>56</sup>, the gene expression is determined by the accessibility of the genetic materials to the transcriptional protein complexes, which may be associated to the changes of nuclear architecture.

It has been reported that the development of cancer cells are also associated with nuclear architecture changes<sup>57</sup>. The evolution of cancer cells is a multi-step process and it has been shown that an alteration in gene expression plays a central role<sup>58</sup>. Epigenetics hypothesizes that the alteration in gene expression of cancer cells may be mediated without mutations in the primary DNA sequence of a gene<sup>59</sup>. Together, the nuclear architecture change might also be associated with tumorigenesis. Currently, much of the structural information of nuclear organization is based on the analysis of fluorescent labeling in fixed cells<sup>50</sup>. However, the real time response of the chromatin structure is not well understood due to experimental difficulty. In Chapter 5, the dynamics of a newly discovered nuclear body (NB), which contains a cancer cell associated protein NAC-1, is studied in live cells by utilizing single particle tracking. This chapter provides intra-nuclear dynamics information, determined by the association between chromatin and the NAC-1 protein-containing NB (NAC-1 NB).

## **1.2 Study Outline**

This dissertation includes four research topics, which are described in detail from chapter 2 to 5, respectively. In this chapter (chapter 1), I have explained the rationale for studying these topics. In Chapter 2, the foundation for describing how to extract the positioning error from image analysis in later chapters is introduced. In chapter 3, the method to quantitatively determine the optimum settings of electron multiplication from a charge-coupled device for particle tracking is addressed. In chapter 4, I develop a method using the Kalman filter, a recursive algorithm used successfully in systems and control theories, to estimate a high-resolution trajectory when tracking under the optical limitations. In chapter 5, the investigation of the real time movement of NAC-1 nuclear

bodies in living cells is presented, based on the developed methods described in prior chapters. Finally, the last chapter (chapter 6) concludes this dissertation.

## CHAPTER 2 A METHOD TO ACHIEVE HIGH ACCURACY MICRORHEOLOGY

### 2.1 Background

Video-based particle tracking monitors the real-time motion of tracer particles. The mean square displacement (MSD) of these tracer particles may be used to interpret cellular biophysical properties, including the diffusivities of lipid membrane and transmembrane proteins<sup>1, 2</sup>, intracellular mechanics<sup>3, 4</sup> and the dynamics of chromatin and nuclear bodies<sup>4-10</sup>. However, as more confined spaces are probed with higher temporal resolution, the ability of particle tracking to perform with consistent accuracy is diminished by the inherent measurement error<sup>11, 12</sup>. For example, when imaging with a charge-coupled device (CCD) camera, the noise can fluctuate between individual pixels within tracking frames causing a positioning error. This error will propagate as static error to affect the accuracy of MSD analysis because the MSD is calculated from a particle's displacement<sup>12-14</sup>.

The characteristics of static error have been previously discussed from a theoretical perspective<sup>11-13</sup>. Webb's group investigated the magnitude of positioning error as a function of the number of detected photons and the spot size, demonstrating that the most reliable results stem from brighter, well-defined particles<sup>13</sup>. In their studies, a formula was derived to calculate the spatial resolution. This formula enables a quick estimation of the spatial resolution with approximately 70% accuracy when compared to their own experimental results from tracking immobilized particles<sup>13</sup>. Later, Savin and Doyle also developed a theoretical model to describe the static error based on a signal-independent Gaussian noise. Their work suggested that more accurate MSD's could be obtained by directly subtracting the extracted static error from

experimental MSD results<sup>12</sup>. These works approximated the static error in tracking systems, demonstrating the critical importance of correcting a potentially significant bias. However, a method to precisely extract static error from individual experimental systems is not currently known, and the accuracy of the MSD information used to decipher the biophysical properties of cellular systems has thus been limited.

Herein, a new method is developed to accurately quantify static error. Using a Monte Carlo approach over a statistically meaningful number of trials, the standard deviation (the spatial resolution,  $\epsilon$ ) of the tracked positions of a static particle in an image was used as a quantitative measurement of the static error ( $2\epsilon^2$ )<sup>12-14</sup>. In this way, the dependence of static error on a particle's signal intensity, background intensity, radius, and center position within a pixel was individually quantified. Simulated images constructed from these controlling parameters were empirically mapped to experimental images so that the static error extracted from simulations could be applied to correct the MSD of actual experiments. An advantage of this strategy is that it solely relies on experimental outcomes, bypassing the details of complicated tracking algorithms and the various hardware specifications of tracking systems<sup>12, 13, 15</sup>. More importantly, this method significantly improves the resolution of particle tracking experiments, greatly reducing ambiguities and potential errors in the interpretation of experiments.

The effectiveness of this approach was successfully tested by tracking particles in glycerol. Rheological measurements using this novel approach compare very well with conventional macroscopic rheological measurements. Creep compliance measurements of the cytoplasmic region of serum-starved MC3T3-E1 fibroblasts using this method revealed a greater degree of free diffusion in a shorter time scale than

originally observed. Thus, this correction enhances our capacity to assess accurate MSD and offers a powerful approach for the significant advancement of particle tracking techniques used for the studies of cellular dynamics and microrheology.

## **2.2 Material and Methods**

### **2.2.1 Preparation of Glycerol Samples with Embedded Fluorescent Particles**

Glycerol samples with suspended 100-nm carboxylated polystyrene fluorophores (Invitrogen, Carlsbad, CA) were made by well mixing with ethanol at a 1/1000 volume-ratio on a center area of a glass bottom dish (MatTek, Ashland, MA). Slides for tracking immobile particles were prepared by air drying the mixture onto a glass coverslip. The coverslip was mounted onto a glass slide with a drop of Fluoromount-G (SouthernBiotech, Birmingham, AL) and allowed to dry for 4 hrs before being sealed with nail polish.

### **2.2.2 Microscope and CCD Acquisition System**

A Nikon TE 2000-E inverted microscope equipped with a 60× oil-immersion, N.A. 1.4 objective lens (Nikon, Melville, NY) and a Cascade 1k camera (Roper scientific, Tucson, AZ) was used to acquire the time course images of fluorescent particles for each sample. UV-visible light from X-Cite 120 PC (EXFO, Mississauga, Ontario, Canada) incorporated with a G-2E/C filter (528-553/590-630 excitation/emission, Nikon) was used to excite the particles. Three by three binning, which increased the increment of pixel size three times to 390 nm, and region of interest control were used to increase the frame rate to 30 frames per second (fps) and enhance the signal-to-noise ratio (SNR). On-chip multiplication gain functionality of the CCD was activated to effectively reduce the CCD readout noise and further enhance the SNR. Video was captured at 30

fps over the course of 21.5 sec, allowing 1.5 sec for the frame rate to stabilize after initiation and 20 sec for a single particle tracking realization.

### 2.2.3 Particle Tracking Algorithm

Tracking images not only contain the signals from the objects that were being analyzed, but also the system's inherent noise and background signals. To distinguish the object signals from the noise and background, the images needed to be filtered to reduce the noise and to subtract the background. In this study, a Gaussian kernel filter<sup>15</sup> was selected to process the images. Many filters are designed for this purpose, such as an Airy disk<sup>2</sup> for the point-spread function; however, a Gaussian kernel filter is mathematically more tractable and shows an insignificant difference in practice.

In this study, MSD obtained by three positioning algorithms, centroid, Gaussian-fitting, and cross correlation (COR), have been cross-compared for fixed particles (Presumably the true MSD is equal to zero). The results suggested that the position determined by the Gaussian-fitting algorithm possessed the smallest static error because it generated the lowest MSD values for fixed particles. Moreover, the Gaussian-fitting algorithm not only yields an estimated particle position but also a peak intensity and radius, which can further be utilized in this simulation approach for predicting the static error (see the Monte Carlo simulation section below).

Thereafter, the filtered images were subjected to direct Gaussian curve fitting, as it had shown that this was the preferred method for particle localization in comparison to the Centroid and Cross-Correlation methods<sup>14</sup>. Direct Gaussian curve fitting utilizes a least squares algorithm on the logarithmic 2-dimensional Gaussian distribution formula,

$$\log I_p(x, y) = \log(I') - \frac{(x - \mu_x')^2 + (y - \mu_y')^2}{2 \times R_a'^2} \quad (2-1)$$

to fit the particle intensity on the filtered images and to locate the particle position from the local maximum intensity pixel and its adjacent four pixels<sup>14</sup>. In the equation,  $I_p$  represents the pixel intensity of an image and the fitted parameters  $I'$ ,  $R_a'$ ,  $\mu_x'$  and  $\mu_y'$  represent the particle peak intensity, particle image radius, and center position of the particle in x- and y-direction, respectively.

#### 2.2.4 Mean Square Displacement

Captured videos of fluctuating microspheres were analyzed by custom particle tracking routines incorporated into MATLAB (The MathWorks, Inc., Natick, MA).

Individual time-averaged MSD's are expressed by the formula,

$$\langle \Delta r^2(\tau) \rangle = \langle [x(t + \tau) - x(t)]^2 + [y(t + \tau) - y(t)]^2 \rangle, \quad (2-2)$$

where  $x(t)$  and  $y(t)$  are the time dependent coordinates of a nanoparticle in the x- and y-directions,  $t$  is the elapsed time,  $\tau$  is the time lag, and the brackets represent time averaging<sup>60</sup>.

#### 2.2.5 Extracting the Noise Amplitude and Estimating the Mean Signal Intensity

Various combined sources of noise can occur in a CCD camera. The dominant varieties of noise are shot noise, readout noise, and background noise from out-of-focus particles<sup>12, 61</sup>. Under a uniform light source, each sensing unit (i.e., a pixel) should receive the same quantity of photons to be converted to the digital intensity output  $I_p$ . However, the fixed pattern noise suggested that each pixel unit inherently possesses an incomparable random bias in photon measurement<sup>61</sup>. The mean signal intensity ( $I_{PS}$ ) of the whole image can be estimated from the mean intensity over all pixels ( $I_P$ ). To eliminate the bias caused by fixed pattern noise, intensity subtraction between two frames with the same amplitude of illumination power is used. Therefore, the standard

deviation (STD) of pixel intensity ( $I_P$ ) can mathematically represent the noise amplitude ( $I_{PN}$ ).

$$I_{PN} = \frac{STD(I_{P1} - I_{P2})}{\sqrt{2}} \quad (2-3)$$

To estimate the background intensity ( $I_B$ ) from an experimental CCD image with fluorescent particles present, the same method described in the previous paragraph was applied but using only the particle-signal-free region instead of the entire image. The particle signal region was found by looking for a difference larger than one between two convolved images, i.e., Gaussian kernel of half width (1 pxl) and Gaussian kernel of consistent size ( $2w+1$ , 7 pxl)<sup>12</sup>. Therefore, the region where the signal difference was less than one was selected for further background intensity analysis.

### 2.2.6 Monte Carlo Simulation

Gaussian particles were simulated in the central area of a zero-intensity, 31 pixel  $\times$  31 pixel zone image. A two-dimensional Gaussian distribution was used to describe the intensity profile of a simulated Gaussian bead. A noise free Gaussian particle ( $I_P$ ) can be expressed as

$$I_P(x,y) = I \times \exp\left(-\frac{(x - \mu_x)^2 + (y - \mu_y)^2}{2 \times R_a^2}\right) + I_B, \quad (2-4)$$

where  $I_P(x, y)$  is the pixel intensity value at the  $x, y$  position of an image,  $I$  represents the peak intensity,  $\mu_x$  and  $\mu_y$  are the sub-pixel location of Gaussian particle in  $x$ - and  $y$ -direction respectively, and  $R_a$  indicates the apparent radius of particle intensity profile. Further, homogenous background intensity ( $I_B$ ) is added to each pixel in order to mimic real imaging. The  $I_P$  intensity array represents the simulated noise free image. Based on the experimental noise extracted from the microscopic tracking system used,

the  $I_{PN}$  of each pixel is correlated with its  $I_{PS}$ , the individual pixel signal intensity (see Fig. 2-1D). Therefore, simulated images (IMG) that mimic real imaging conditions can be represented by

$$IMG(x,y) = [I_p(x,y)] + StoN(I_p(x,y)) \times R(0, 1). \quad (2-5)$$

In the preceding function, StoN represents the empirically measured correlation between  $I_{PS}$  and  $I_{PN}$  (in the case herein, it is a 4th order polynomial; see Fig 2-1C).  $R(0,1)$  represents a normally distributed random number with zero mean and unit variance. Here a Gaussian noise was used to represent the system noise over the full intensity spectrum. The noise sources in a pixel of CCD are mainly dominated by readout and photon shot noise. The noise intensity histogram of the CCD camera of the experimental system displayed a Gaussian distribution throughout the entire CCD signal sensing range from 1300 arbitrary units (AU) to 65535 AU. The R-squared value from fitting a Gaussian distribution to the entire spectrum of  $I_{PS}$  in the experiment was always higher than 0.98, suggesting that the use of a Gaussian random number in the Monte Carlo simulation to represent  $I_{PS}$  could be justified. This is in agreement with previous independent studies, which demonstrated that the combined noises, including shot noise, dark noise and readout noise, show a Gaussian distribution for a high influx of photons<sup>13, 61</sup>.

The simulated image was further processed through the particle-tracking algorithm to estimate the simulated particle's position. Six hundred trials were tested for each condition in order to estimate the uncertainty in positioning and the relative error for this estimation was found to be below 3%. The position error ( $\varepsilon_p$ ) is defined as the distance between the true position and the position estimated by the tracking algorithm. Spatial

resolution ( $\epsilon$ ), and hence static error ( $2\epsilon^2$ ), is estimated from the summation of standard deviation in the x- and y-directions.

### **2.2.7 Rheometer**

Conventional rheology studies on the glycerol samples were conducted using an AR-G2 stress-controlled software-operated rheometer (TA Instruments, New Castle, DE). Glycerol was loaded into a 60 mm cone-and-plate sampler module (cone angle =  $1^\circ$ ). To determine the viscoelastic properties of glycerol, the sample was subjected to 0.05% sinusoidal shear strains with the frequency gradually increasing from 0.01 to 50 Hz (frequency sweep test) under isothermal conditions ( $23^\circ\text{C}$ ).

### **2.2.8 Intracellular Particle Tracking and Cytoplasmic Rheology**

MC3T3-E1 (Riken Cell Bank, Tokyo, Japan) were cultured in  $\alpha$ MEM supplemented with 10% fetal bovine serum (FBS, Hyclone, Logan, UT), 100 IU/ml penicillin and 100  $\mu\text{g/ml}$  streptomycin and maintained at  $37^\circ\text{C}$  in a humidified, 5%  $\text{CO}_2$  environment. Cells were passed every 3-4 days and seeded (approximately  $1 \times 10^4$  cells/ml) onto 10-cm cell culture dishes. Before particle tracking experiments, MC3T3-E1 cells were plated on 35-mm cell culture dishes and subjected to ballistic injection of 100-nm carboxylated polystyrene fluorophores (Invitrogen) using a Biolistic PDS-1000/HE particle-delivery system (Bio-Rad, Hercules, CA). In the ballistic injection process, nanoparticles were placed on macrocarriers and allowed to dry for 2 hrs. A rupture disk with 1800-psi rupture pressure were used in conjunction with a hepta adapter<sup>3</sup>. After injection, cells were plated again using  $\alpha$ MEM supplemented with 5% FBS on dishes coated with 20  $\mu\text{g/ml}$  fibronectin (EMD Chemicals, Gibbstown, NJ). Culture medium was replaced the

next day with serum-free  $\alpha$ MEM. Cells were serum-starved for 48 hrs prior to the particle tracking experiments.

After the particle tracking experiment, the MSD of each probed nanosphere was directly related to the local creep compliance<sup>62</sup> of the cytoplasm,  $\Gamma(\tau)$ , by

$$\Gamma(\tau) = \frac{3\pi a}{2k_B T} \langle \Delta r^2(\tau) \rangle \quad (2-6)$$

The creep compliance (expressed in units of  $\text{cm}^2/\text{dyne}$ , the inverse of a modulus) describes the local deformation of the cytoplasm induced by the thermally excited displacements of the nanoparticles. If the cytoplasm around a nanosphere has fluid-like behavior (e.g. glycerol), then the creep compliance increases continuously and linearly with time, with a slope that is inversely proportional to the shear viscosity,  $\Gamma(\tau) = \tau/\eta$ . If the cytoplasm has local solid-like behavior (e.g. a gel), then the creep compliance is a constant with a value inversely proportional to the elasticity of the gel,  $\Gamma(\tau) = 1/G_0$ . The local frequency-dependent viscoelastic parameters of the cytoplasm,  $G'(\omega)$  and  $G''(\omega)$  (both expressed in units of  $\text{dyne}/\text{cm}^2$ , a force per unit area), were computed in a straightforward manner from the MSD<sup>4</sup>. The elastic modulus,  $G'$ , and viscous modulus,  $G''$ , describe the propensity of a complex fluid to resist elastically and to flow under mechanical stress, respectively.

## 2.3 Results

### 2.3.1 Light Source Affects the MSD Values

The consistency of a purely homogeneous medium should be reflected by an identical MSD value for each tracked particle at any given time lag. This was not observed for glycerol, which had a distribution of MSD's inconsistent with a homogeneous medium, especially at shorter time lags (Fig. 2-1A). Analysis of this

discrepancy revealed a correlation between MSD ( $\tau = 33$  msec) and the peak intensity for individual microspheres (Fig. 2-1B). Emission outside of the microscope's focal plane or interference from other randomly distributed particles obstructing the light path may affect the light intensity emitted from a microsphere to the photon detector, causing a distribution of peak intensity within a sample. Additionally, the digitization of photon signals by the detector introduces shot noise, and may also involve other types of noise<sup>61</sup>. The presence of this combined noise could introduce significant bias in image analysis, making it essential to correct MSD values in particle tracking experiments.

Subsequently, it was investigated whether the error revealed by the variation in MSD directly stems from the intensity fluctuations of the overall recorded signal. This was accomplished by extracting the signal and noise information from individual pixels throughout the whole image. Different pixels do not generate purely random noise under the same projected light due to noise inherent to the measurement device such as dark current variation and fixed pattern noise<sup>61</sup>, which are consistently associated with an individual pixel and independent of outside signals. To eliminate this bias from each pixel, one reference image was set as a standard, and a successive image with the same illumination was then subtracted from the reference image<sup>61</sup>. This procedure resulted in an even-weight (one bit of data per pixel) array with non-biased random noise. The random noise had an approximate Gaussian distribution and zero mean (consistently biased noise and the background intensity are filtered by the reference image subtraction). Therefore, the intensity of homogeneous light emitted from a halogen bulb can be determined by the mean pixel intensity ( $I_{PS}$ ) for pixels over the whole image, and a distribution profile of random noise corresponding to the illumination

source can be determined to obtain the mean random noise intensity ( $I_{PN}$ ) (see materials and methods).

Using the above method, images of water were taken under a homogeneous field of collimated light from a halogen bulb, either with or without a 590-nm cut-off (red) filter in the light path, or with various concentrations of rhodamine B-labelled dextran with a red filter, to extract the  $I_{PS}$  and the  $I_{PN}$  particular to the microscope being used. Using a CCD camera, a consistent correlation between  $I_{PS}$  and  $I_{PN}$  emerged from each of the three different experimental settings, over the full working range of light intensity (Fig. 2-1C). Therefore, the correlation between  $I_{PS}$  and  $I_{PN}$  suggests that a tracking system could possess a digital output signal dependent noise, which cannot be simply expressed by only shot noise ( $I_{PN} = I_{PS}^{1/2}$ )<sup>14</sup>, Gaussian noise ( $I_{PN} = N$ , where  $N$  is a constant)<sup>12</sup>, nor a combination of both ( $I_{PN} = I_{PS}^{1/2} + N$ )<sup>13</sup>.

Consequently, this information was used to effectively estimate the SNR ( $I_{PS} / I_{PN}$ ) for pixels over the full spectrum of  $I_{PS}$  (Fig. 2-1D). These data further revealed that varying light intensity drastically affects the SNR for the camera readout, with brighter particles yielding better spatial resolutions. Furthermore, because the settings of a CCD camera (such as the gain in on-chip multiplication) can alter the correlation between  $I_{PS}$  and  $I_{PN}$ , the method demonstrated here offers a generic procedure to easily extract the SNR profile from any CCD camera-based tracking system for static error determination.

### **2.3.2 Interplay of Several Factors Determines the Static Error**

The SNR determined for the tracking system was then applied to create simulated images, which were used as a basis for investigating the conditions governing  $I_{PS}$  fluctuations and the degree of particle positioning bias. A Gaussian-shaped simulated bead was constructed (see materials and methods), which had a defined peak intensity

( $I$ ), radius ( $R_a$ ) and subpixel location ( $\mu_x = \mu_y = 0$  for the center of the pixel), with a homogeneous background intensity ( $I_B$ ). Once the bead parameters were assigned, the appropriate level of random noise was added to individual pixels in the simulated image based on the established SNR (Fig. 2-1D). Subsequently, the simulated image containing the “system noise” was added to the particle tracking algorithm to determine the “experimental” tracked position of the bead. These images were reconstructed multiple times to represent separate tracking trials under the given initial parameters, and the spatial resolution (i.e. standard deviation of the positioning distribution) of the bead was obtained after conducting a statistically meaningful number of such trials (Fig. 2-2A).

Using this Monte Carlo approach, an investigation was conducted of the relationship between the peak intensity of particles ( $I$ ) and the resulting positioning distributions. Trials for three different Gaussian bead peak intensities ( $\mu_x = \mu_y = 0$ ,  $R_a = 0.54$  and  $I = 5,000$ ,  $10,000$  and  $50,000$ , respectively) with a uniform background intensity ( $I_B = 3,000$ ) suggested that the positioning error is related to the peak intensities (Fig. 2-2B, left). In addition, the brighter peak intensities resulted in a tighter distribution of tracked positions and a smaller positioning error (Fig. 2-2B, right). Since the spatial resolution ( $\epsilon$ ) can be quantitatively linked to the static error ( $2\epsilon^2$ )<sup>12-14</sup>, the brighter peak intensities directly translate to a diminished static error. Moreover, static error vs. the peak intensity was plotted for Gaussian beads having three sets of  $I_B$  and  $R_a$  values to demonstrate the dependence of static error on these additional parameters (Fig. 2-2C). In each case, the static error always decreased incrementally with Gaussian bead peak intensity.

The final Gaussian bead parameter that could have an effect on the static error profile was the subpixel location. Under a uniform  $I_B$ , Gaussian beads with a fixed  $I$  and  $R_a$  were assigned different subpixel locations, i.e.,  $(\mu_x, \mu_y) = (0, 0)$ ,  $(-0.25, -0.25)$  and  $(-0.5, -0.5)$ , where  $\mu_i = 0$  corresponded to the pixel center and  $\mu_i = -0.5$  corresponded to the pixel edge, respectively. The static error extracted from the set centered within the pixel was used as a reference to observe deviations in the error distribution at other bead locations. Monte Carlo simulations suggested a trend of increasing error as Gaussian beads move closer to the pixel edge (Fig. 2-2D). To further understand this trend, the evaluation of sub-pixelation effects on the static error was repeated throughout a whole pixel quadrant (since there is symmetry about the pixel center in both the x- and y-axis). It was found that the subpixel position can augment static error up to 1.5 fold (from  $\sim 6 \times 10^{-3} \mu\text{m}^2$  to  $\sim 9 \times 10^{-3} \mu\text{m}^2$ ) for a single set of assigned bead parameters (Fig. 2-2E). Thus, the sub-pixel localization of the bead center also contributes to the static error, revealing that several bead parameters collectively contribute to the propagation of such error.

### **2.3.3 Direct Parameter-Mapping can be used to Accurately Estimate the Static Error**

Although the static error extracted from the Monte Carlo trials is affected by the individual manipulation of peak intensity, radius, subpixel location and background intensity values, these parameters may not be independent or constant throughout an actual experiment. As particles move out from the focal plane, their projected image will simultaneously appear to have a larger radius and dimmer peak intensity than if they were in focus<sup>63</sup>. The background intensity also changes for different microscopic and environmental conditions. Furthermore, some microenvironments constrain particles so

that the total displacement of a particle during short lag times can be less than the pixel size (i.e., a particle embedded in highly viscous and/or highly elastic media). In this case, subpixel localization of the particle will be a dominant factor for static error in the tracking analysis. Therefore, the accurate representation of experimental particles necessitates a case by case assignment of the proper Gaussian bead parameters to validate the Monte Carlo approach of extracting the spatial resolution using simulated images.

Particle tracking algorithms independently process microspheres in the acquired images and produce a set of experimental parameters,  $(R_a', I', \mu_x'$  and  $\mu_y')$  to describe each tracked microsphere. However, these parameters cannot represent the true characteristics of particles because they have been processed by convolution of the tracking algorithm, and cannot be directly used to extract the static error by Monte Carlo simulation. A novel mapping procedure has been developed to estimate the true parameters  $(R_a, I, \mu_x$  and  $\mu_y)$  of the original microsphere from the convolved images of the non-linear algorithm tracking analysis (Fig. 2-3A). During this process, the addition of extracted system noise to the simulated images was omitted in order to avoid generating additional variation in the image data that would only corrupt the comparisons.

The mapping begins by assuming that the absolute position of a simulated Gaussian bead,  $(\mu_x, \mu_y)$ , is the same as the experimentally tracked positions,  $(\mu_x', \mu_y')$ . This assumption has previously been evaluated with the conclusion that the pixelization effects can only generate up to 0.02 pixels of error<sup>12</sup>. Several simulated Gaussian bead images generated by a series of  $R_a$  values (from 0.38 to 1.80 pixels) and different peak

and background intensities were subjected to the tracking algorithm to retrieve the corresponding apparent radii ( $R_a'$ ). A scatter plot of  $R_a$  to  $R_a'$  fit by a 4th-order polynomial with perfect regression ( $R^2 = 1$ ) (Fig. 2-3B) is evidence that the correlation of  $R_a$  and  $R_a'$  depends only on the tracking algorithm and is independent of the peak intensity of the Gaussian bead and the background pixel intensity. Having accounted for all other Gaussian bead parameters, the relationship between  $I$  and  $I'$  was uncovered using a linear curve fitting (Fig. 2-3C). The entire mapping procedure was repeated for a range of Gaussian bead parameter configurations until a clear link between simulated and experimental tracking images was evident. Through this simple process, any typical microsphere experimental image can be precisely simulated by a corresponding Gaussian bead image (Fig. 2-4). The mapped values of the pixel intensity in a 3 pixel  $\times$  3 pixel region are comparable between the simulated bead and the experimentally tracked microsphere. This result demonstrates that the correlations determined by this procedure can be used to define experimentally relevant Gaussian beads to determine static error.

#### **2.3.4 Procedure Verification using *in vitro* and *in situ* Experimental Systems**

The accuracy of the mapping procedure was verified by imaging static particles. Several microspheres were immobilized onto a coverslip and their MSDs were tracked. Immobilized microspheres should exhibit approximately no movement, and the detected MSD values are expected to represent the static error. The mapping procedure was applied to estimate the static error from the experimental images. Comparing the experimental static error of each microsphere to its peak intensity revealed that static

error invariably reduces when the peak intensity of the corresponding microsphere increases (Fig. 2-5A). Using the Monte Carlo simulation trials, the static error ( $2\varepsilon^2$ ) was extracted and correlated to the experimental static error in a log-log plot showing that the simulated static error is in agreement with the experimental results (MSD), having a strong linear correlation ( $R^2 = 0.99$ ) (Fig. 2-5B). This strong correlation confirms that the Monte Carlo simulation approach explained herein can successfully estimate real-time static error.

MSD data from a standard tracking analysis in glycerol was corrected using this technique by directly subtracting the estimated static error value. Comparison between the raw and corrected results under low (25%) and high (100%) illumination suggests that the correction produce significantly more precise results, reflecting the true nature of the homogeneous Newtonian fluid (Fig. 2-5C). When the generalized Stokes-Einstein Relation was used to convert the MSDs to the viscous modulus, it was found that the values are underestimated in the raw MSDs of low illumination, but are accurate when the MSDs are calibrated or are obtained from high illumination experiments (Fig. 2-5D). This provides another validation of the fact that static error is important in tracking experiments, and should be eliminated using the correction algorithm (Fig. 2-5E).

Further investigations demonstrated the use of the correction technique for tracking particles inside cells and calculating the creep compliance from the MSD data. One-hundred-nm diameter, carboxylated fluorescent microspheres were ballistically bombarded into the cytoplasm of a MC3T3-E1 fibroblasts culture. After serum-starving for 48 hrs, the majority of particles were evenly distributed into the cytoplasmic region of the cells (Fig. 2-6A). In comparison with a standard cell culture, serum-starved cells lack

massive actin-cytoskeletal structures in most of their cytoplasmic region<sup>64</sup>, and in this cytoskeletal-depleted zone, particles are permitted to exhibit a relatively greater degree of free diffusion. Yet, the time scaling profile of the raw MSDs obtained from particle tracking indicate that almost all such particles in the cytoplasmic region move sub-diffusively (Fig. 2-6B). In contrast, the corrected MSD values obtained by the approach herein suggest that these particles are less sub-diffusive (Fig. 2-6C). This analysis strongly advocates the necessity of eliminating static error from MSD measurements for correctly probing the cellular biophysical properties using particle tracking.

### **2.3 Discussion**

MSD inaccuracy due to static error is ubiquitous in CCD camera-based particle tracking systems. However, the complex interplay between multiple tracking parameters had precluded the development of a practical method to minimize the errors. The correction approach explained herein significantly minimizes static error. This approach circumvents the complication of direct static error calculation by employing a simulation-based method to correct experimental particle tracking measurements. This considerably enhances the accuracy of the MSD and improves the subsequent estimation of diffusivity as well as rheological properties.

Tracking of particles in a homogenous glycerol solution resulted in a wider MSD distribution at short lag times with decreasing light source intensity. This result indicates that static error can significantly bias the MSD profile, potentially causing a misinterpretation of the underlying physical properties<sup>11</sup>. Static error in the tracking system used herein can be estimated to be between  $\sim 2 \times 10^{-5} \mu\text{m}^2$  and  $\sim 10^{-3} \mu\text{m}^2$  by tracking immobilized microspheres, suggesting that measured MSD values within this

range are clearly unreliable. However, elimination of this static error allows for an accurate MSD measurement with a resolution of  $\sim 10^{-6} \mu\text{m}^2$  from a sufficiently bright particle.

In the simulation approach, the simulated Gaussian bead has a single “point” position expressing the peak intensity, which is an appropriate model to match with the Gaussian fit algorithm. The particle diameter used in this study was 100 nm while many *in vitro* studies have applied particles of a larger size for tracking. Compared to larger particles, the 100-nm particle is more suitable to be considered as a “point” light source. Meanwhile, my unpublished data suggested that the estimated static error is comparable to the measured MSD obtained from fixed 1-micron particles. In essence, this method can be applied to the current particle tracking experiments regardless of the particle size.

However, there are some additional advantages to the use of 100 nm particles that were chosen for this work. Light scattering by tracking particles can directly affect the background signal in a tracking video while simultaneously depleting the detectable peak intensity within the exposure time. These effects can have a detrimental outcome on the proper estimation of MSD. Based on the Mie theory, the main parameter to consider in elastic light scattering is the size parameter,  $x = 2\pi R/\lambda$ , where  $\lambda$  is the wavelength and R is the radius of the particle. The wavelength of the light used in the video-based particle-tracking experiment ranges between  $\sim 400$  to  $700$  nm. Therefore, the 100-nm size particle has an  $x \sim 0.5$ , in which the extinction coefficient is negligible and light scattering effects are minimized. Meanwhile, Rayleigh scattering will not affect the particle tracking results unless the size of the particle is reduced to  $\sim 10$  nm.

For a 1-micron particle, the size parameter of light scattering is approximately equal to 5 and the extinction coefficient approaches the maximum value. Therefore, light absorbance by 1-micron particles is inevitable. Nevertheless, the emitted signal from an 1-micron particle is much higher than the detectable threshold (SNR is much greater compared to the 100-nm particle). The larger particle should have much smaller static error. However, when the particle size increases from 100 nm, the extinction coefficient consequently increases as well, which would generate heat and increase the temperature to the microenvironment. Therefore, heat effects on the experiments would need to be assessed.

To ensure that the discrepancy of MSD values of 100 nm particles embedded in glycerol was not an effect of heat generated from different power settings of the light source, particle-tracking was repeated successively three times on a sample at full power of light intensity. In this case, the sample was exposed to constant light for more than 1 minute. The three tracking results were carefully compared to evaluate whether the MSD values shift toward higher or lower values. The result showed that there was no heat accumulation which would affect a change in the MSD (data not shown). The short lag-time MSD values for the first 5-sec period and the last 5-sec period in the same experiment were also evaluated to examine the transient heat build-up and it was concluded that the difference of MSD values were not caused by the heat effect for the 100-nm particles.

## **2.4 Conclusion**

In summary, this correction technique is not limited to the particular system used herein, but is broadly applicable to any tracking system. The transition to another system requires simple steps of determining the correlation between the pixel signal

and noise, and appropriately selecting correct tracking parameters. By closely following the methodology described herein, static error can be significantly eliminated, leading to a greater clarity when interpreting the MSD values from a particle tracking experiment.

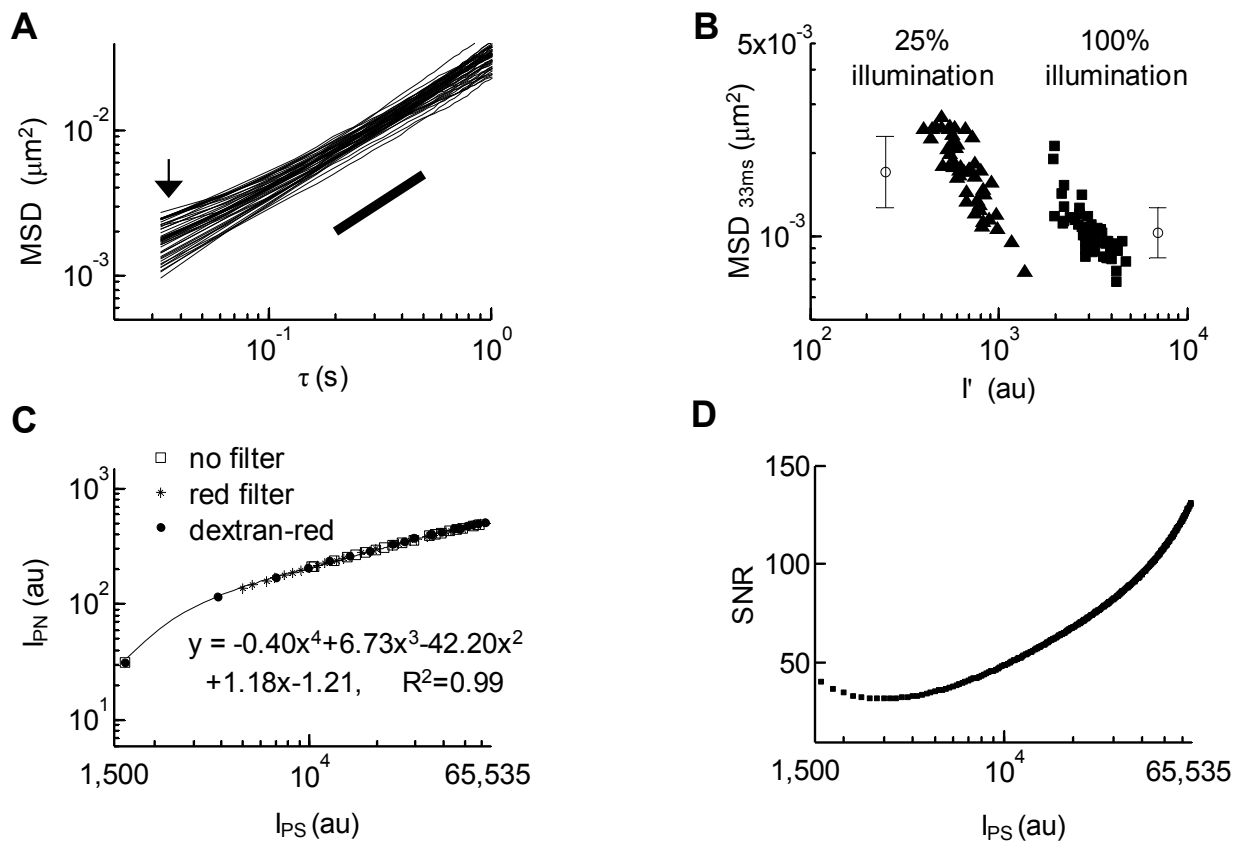


Figure 2-1. The mean square displacement (MSD) is correlated to the peak intensity ( $I'$ ) of microspheres tracked by a charge-coupled device (CCD) camera. (A) A MSD vs. time lag plot of microspheres ( $n = 47$ ) embedded in glycerol shows the presence of MSD variation in a homogeneous aqueous solution (arrow head). The particle tracking experiments were conducted at a time resolution of 33 ms with using 25% of full power of illumination. (B) A logarithm plot of MSD ( $\tau = 33$  ms) vs. peak intensity of microspheres ( $n = 53$ ) embedded in glycerol under 25% ( $\blacktriangle$ ) and 100% ( $\blacksquare$ ) power of illumination suggests a relationship between increasing peak intensity and decreasing MSD value. The error bar shows the mean and standard deviation of the MSD ( $\tau = 33$  ms). (C) Digital intensity signal ( $I_{PS}$ ) and noise ( $I_{PN}$ ) values are extracted from uniform light sources: the head light without a filter ( $\Delta$ ), the head light with a red filter ( $+$ ), and the UV-visible light with a red filter at different concentration of Rhodamine B-tagged 70 kD Dextran ( $\bullet$ ). The IPS-IPN relationship is expressed by a 4th order polynomial fit. (D) Signal-noise-ratio (SNR) vs. digital signal intensity may be determined by the curve fitting described in panel 1C to well-estimate the SNR as a function of the digital signal strength ranging between saturated signal (65535 arbitrary units; i.e., au) and dark current ( $\sim 1500$  au).

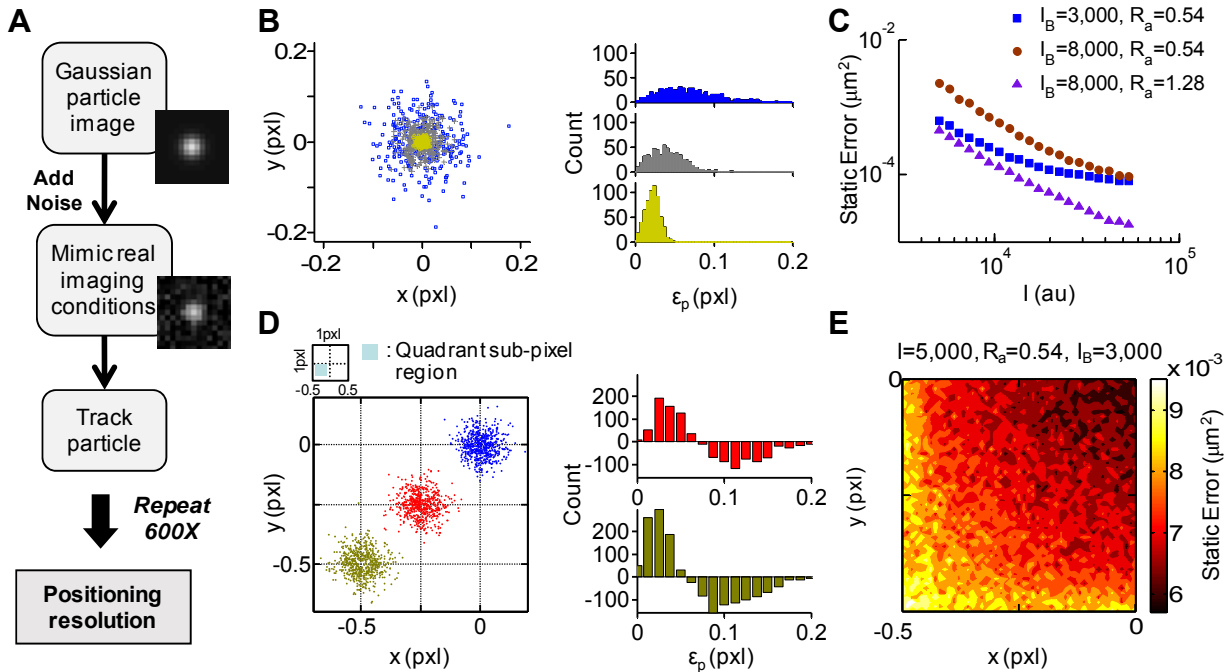


Figure 2-2. Static error ( $2\varepsilon^2$ ) can be estimated using simulated Gaussian beads. (A) A flow diagram demonstrates how to estimate static error by Monte Carlo simulation. (B) Distribution patterns of tracked positions were generated by running 600 independent trials incorporating pixel noise into simulated images using three different intensities of Gaussian beads ( $I = 5,000$  ( $\square$ ),  $10,000$  ( $+$ ), and  $50,000$  ( $\circ$ )) with  $\mu_x = \mu_y = 0$ ,  $R_a = 0.54$  and  $I_B = 3,000$  (left panel). Three histograms in the right panel indicate the distribution of the experimental position error,  $\varepsilon_p$  (the displacement between the experimental center and the assigned center). Beads possessing a higher intensity generate smaller experimental errors with sharper distributions. (C) Static error vs. the assigned peak intensity ( $I$ ) is plotted for the three different Gaussian beads. (D) Left: The distribution of the tracked center after six hundred simulations for Gaussian beads initially in three subpixel locations within the lower-left pixel quadrant ( $(0, 0)$ ,  $(-0.25, -0.25)$  and  $(-0.5, -0.5)$ ) is shown. Right: A histogram of 6,000 positioning error simulations for Gaussian beads located at the pixel center was set as a reference for off-center beads, and differences in count of the tracked displacements suggest that the subpixel location of a microsphere affects the size of its positioning error. (E) The intensity diagram illustrates the correlation between static error and the Gaussian particle subpixel location at a resolution of 0.01 pixels. The intensity bar indicates the range of positioning error.

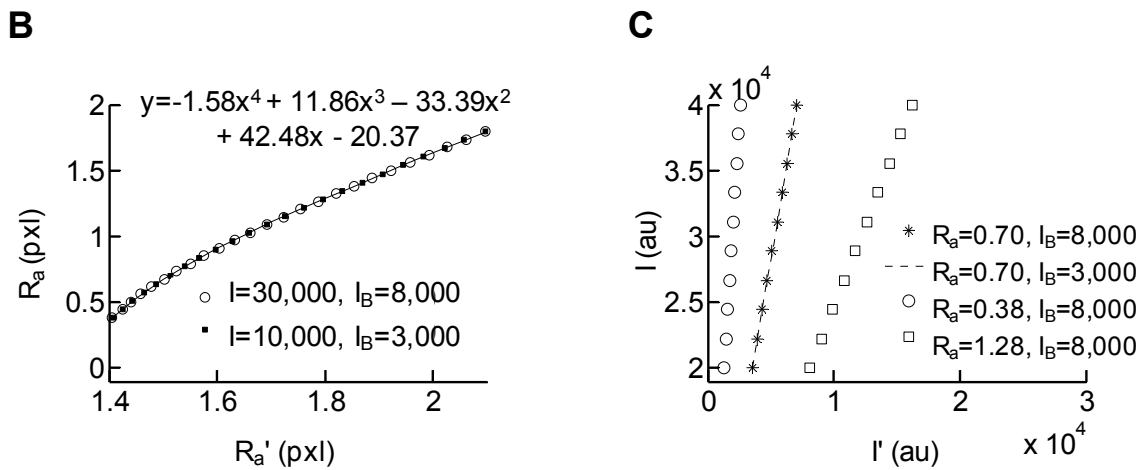
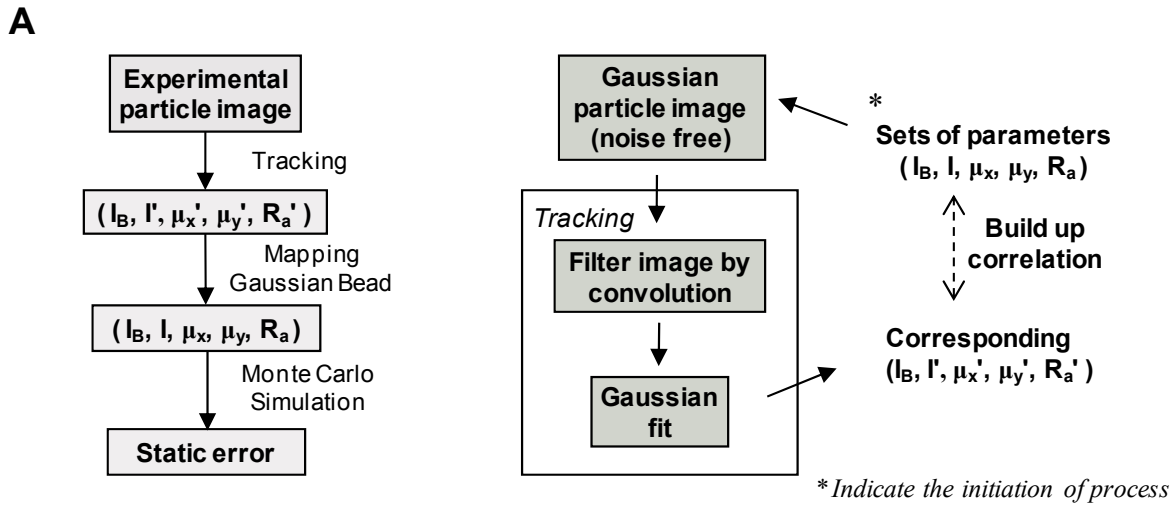


Figure 2-3. The method to relate extracted static error from simulated beads to experimental microsphere images is demonstrated. (A) The left flow chart demonstrates the process of estimating static error from raw particle image. The process retrieves tracked parameters from a raw image, maps the adequate parameters to simulate experimental images with the complementary Gaussian particle, and applies Monte Carlo simulation to estimate the static error. The right flow chart shows the procedure used to map parameters for simulated Gaussian beads to match experimental tracked parameters. (B) A 4th order polynomial equation can be adopted to describe the relationship between the radius of the simulated Gaussian bead,  $R_a$ , and the radius of tracked microsphere,  $R_a'$ , with perfect fitting ( $R^2 = 1$ ). This result is independent of the peak intensity,  $I$ , and background intensity,  $I_B$ . (C) The Gaussian bead peak intensity ( $I$ ) vs. the experimental peak intensity ( $I'$ ), plotted for three different Gaussian bead radii, showing a linear correlation between  $I$  and  $I'$ . The plot also suggests that the correlation is independent of the pixel background since lines are overlaid at the same  $R_a$  despite having pixel backgrounds that are set differently.

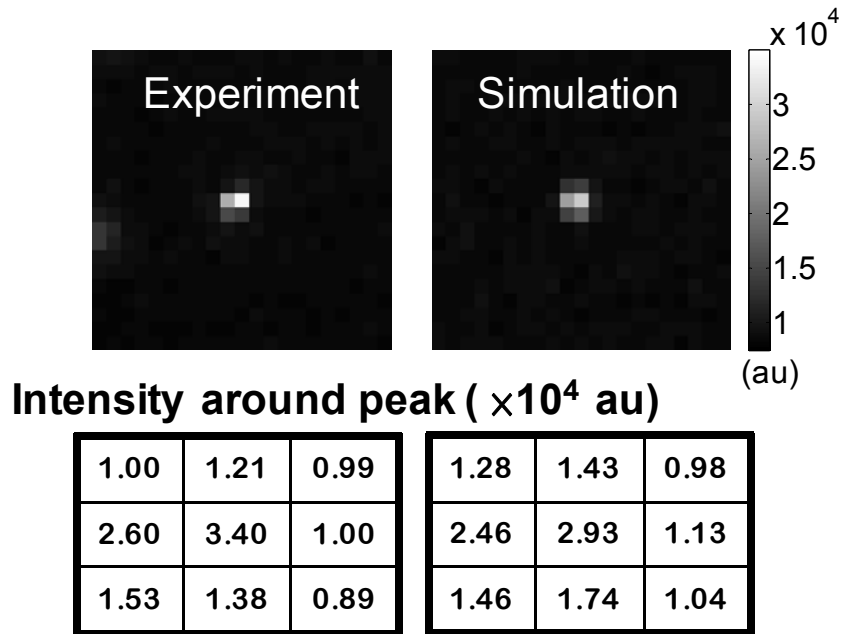


Figure 2-4. A Gaussian bead with the parameters determined by the mapping procedure in this paper can represent the experimental microspheres. The experimental (Left) and simulated (Right) data is in agreement, as evident in their images and the pixel intensity of the 3x3 area surrounding the brightest pixel.

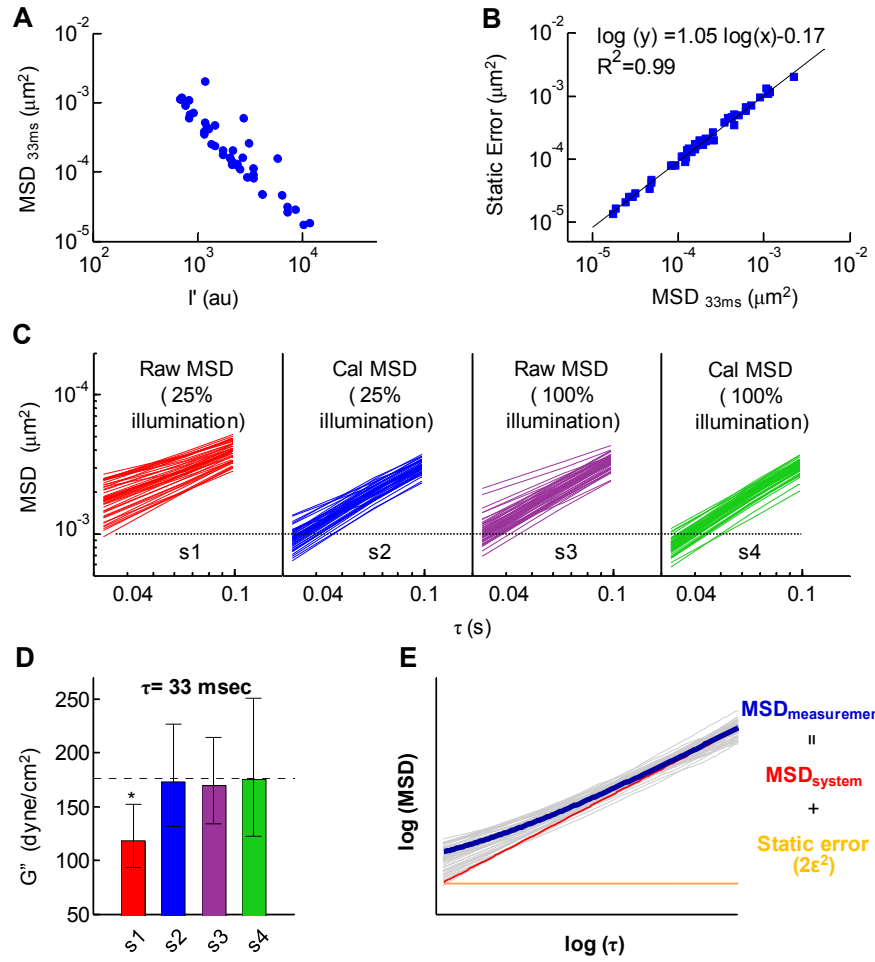


Figure 2-5. Static error can be corrected for the MSD of microspheres embedded in glycerol. (A) A sample of fixed microspheres is used to verify the estimated static error from simulations by representing the tracked MSD values as the spatial error generated from the experimental system. (B) The logarithm of experimental static error (MSD at 33 ms) and the corresponding estimated simulated static error strongly correlate with a linear fit,  $R^2 = 0.99$ . (C) Raw MSD data from particle tracking under 25% power of illumination ( $n = 47$ ) exhibits a degree of heterogeneity in the data, but raw MSD data ( $n = 53$ ) and its corrected MSD both obtained under 100% power of illumination share a similar scale and trend as the corrected MSD from low illumination (25%). (D) The mean viscous modulus,  $G''$ , of glycerol is estimated at time lags of 33 ms from the raw and corrected MSD values at 25% and 100 % power of illumination, respectively. The dashed line indicates the viscous modulus measured by a conventional rheometer and the star denotes the significantly lower  $G''$  of the raw MSD at 25 % power of illumination using a two-tailed t-tests with  $P < 0.05$ . (E) The illustration explains how errors generated from the experimental system can affect the MSD result in the cases of glycerol: Measured MSD is the culmination of system MSD and static error.

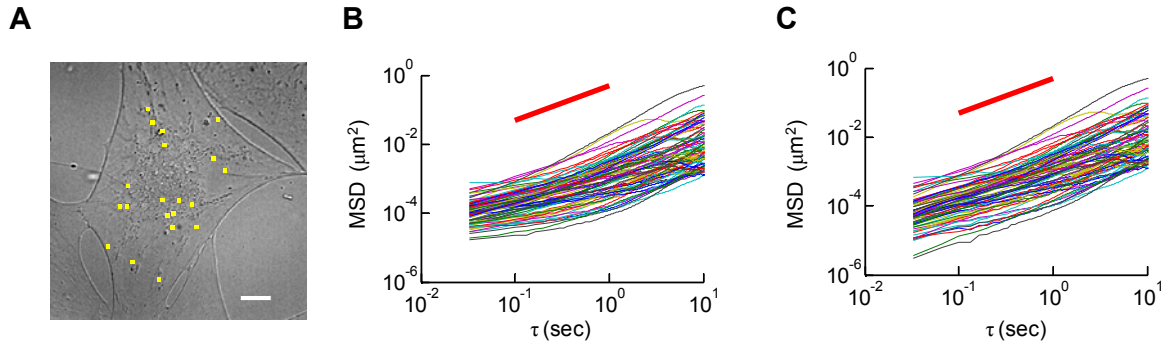


Figure 2-6. Static error can be corrected for the MSD of 100-nm carboxylated polystyrene particles embedded in MC3T3-E1 fibroblast cells under red-fluorescence. (A) An image acquired from the CCD-camera. Square dots indicate the positions of microspheres within the frame. (B) A MSD vs. time lag plot extracted from the cellular system (80 particles in 7 cells) implies subdiffusive particle motion at shorter lag times, indicating a range of local microenvironments that the microspheres are encountering. (C) Using the developed method to subtract out the estimated static error in the system revealed a new MSD profile, which implies more diffusive particle motion throughout the cellular environment at short lag times.

CHAPTER 3  
A GENERAL METHOD FOR IMPROVING SPATIAL RESOLUTION BY OPTIMIZATION  
OF ELECTRON MULTIPLICATION IN CCD IMAGING

**3.1 Background**

Single-cell biophysical assays that quantify size<sup>65</sup>, morphology<sup>66</sup> and movement<sup>67, 68</sup> of subcellular components can provide great insight into macromolecular function and effectively bridge the biological activities at the cellular and the molecular scale together<sup>69</sup>. However, given the heterogeneous nature of the cell structure, single cell measurements need to be performed with high resolution to produce accurate and statistically meaningful data<sup>41, 70</sup>. The most straightforward way to conduct such measurements is through the analysis of individual images or a stack of images acquired with high-resolution microscopy<sup>38, 69, 71</sup>. Therefore, the success of these types of measurements relies on the capability of the camera to obtain high quality cell images. In modern microscopic systems, the most common device adopted as a photon detector is the charge-coupled device (CCD) camera, which can simultaneously use more than one million parallel arrays to sense the intensity profile of light emitted from objects within the visual field of the microscope. With this device, cell images with detailed information can be captured and later analyzed.

Yet, the performance of the CCD camera deteriorates with decreasing light intensity from the sample<sup>16</sup>, and this significantly reduces the accuracy of low intensity subcellular measurements, such as in single molecule fluorescence imaging. This problem can be solved by acquiring images on much more expensive avalanche photodiode detectors (APD) or photomultiplier tubes (PMT)<sup>17, 18</sup>. These types of detectors do not have large numbers of individual sensing units like the parallel array of the CCD camera. When acquiring information from the visual field of the microscope, an

APD or a PMT sensor needs to use a scanning mode, which is usually much slower than the CCD camera. Therefore, if the spatial resolution of low intensity images in a CCD camera can be improved, the CCD camera becomes the best choice due to its accessibility and high acquisition rate.

Several intensity-enhanced techniques have been developed to obtain high contrast images from low intensity signals such as intensified CCD (ICCD) and electron multiplying CCD (EMCCD)<sup>16</sup>. After the back-illuminated EMCCD camera was introduced, the sensitivity of EMCCD has outperformed the ICCD and the EMCCD has become a popular choice for imaging the dynamics of single molecules in cells<sup>19, 20</sup>. EMCCD utilizes several specialized extended serial registers on the CCD chip to apply a high voltage and produce multiplying gain through the process of impact ionization in silicon<sup>21</sup>. This capability to elevate the photon-generated signal above the readout noise of the device even at high frame rates has made it possible to meet the need for ultra-low-light imaging applications without the use of external image intensifiers<sup>72</sup>.

While the EMCCD camera is certainly promising for single particle tracking, a quantitative evaluation of the influence of EM gain on spatial resolution has not been performed. Therefore, Equations to relate the nominal EM gain with image intensity and the variance of image intensity are derived. These equations were fit to experimental data to estimate the relevant image parameters. Quantitative mappings were used along with a Monte Carlo procedure to calculate the dependence of signal to noise ratio (SNR) and spatial positioning error on EM gain. The EMCCD performance to achieve the best spatial resolution and SNR for particle tracking by this approach is successfully optimized. Through this specific example, we have created a general method,

applicable to other types of CCD cameras, which can optimize electron multiplication for subcellular imaging, and provide a quantitative guideline to improve the accuracy of subcellular biophysical assays.

## **3.2 Methods and Results**

### **3.2.1 The EM Gain can Influence Quantitative Image Analysis**

EM gain is an analog signal multiplication feature that multiplies an electronic signal by applying high voltage across several CCD registers before readout<sup>21</sup>. The EM gain setting of the EMCCD camera aims to improve the contrast of the image. Image analysis uses intensity profiles of a group of specific pixels that describe an object. The intensity relations between the adjacent pixels are important for reliable tracking of a single particle. However, the EM gain function does not amplify the SNR equally for objects with different intensities<sup>73</sup>. This suggests that there may be an optimal EM gain setting for achieving the best spatial resolution.

To investigate this in more detail, two types of cellular bodies were probed to determine if the EM gain could preserve or consistently improve the spatial resolution of positioning. Cytoplasmic mRNA processing bodies (also called P-bodies or GW-bodies), labeled by GFP-Ago2<sup>74</sup> through transfection, and nuclear promyelocytic leukemia (PML) bodies, labeled by YFP-Sumo1 (Addgene Inc., Cambridge, MA), were video-tracked without EM gain or with EM gain = 2000 in a fixed NIH 3T3 fibroblast using a TE 2000 microscope (Nikon, Melville, NY), equipped with a Cascade:1K EMCCD camera (Roper Scientific, Tucson, AZ) and a NA 1.45, oil-immersion 60× objective lens (Nikon). For a specific type of EMCCD camera, the EM gain is an arbitrary number correlated to the applied voltage on the CCD registers. The range for our CCD EM gain setting is between 0 and 4095. Through proper assignment of the region of interest (ROI) a high

temporal resolution (30 Hz) can be achieved. In our case, the binning feature in the CCD camera is set as 3×3, resulting in a pixel size of 390 nm. Under these two EM settings, 300 experimental images repeatedly acquired from the same sample were used to assess the variance of positioning via particle tracking<sup>75</sup>. In brief, the raw images were subjected to a Gaussian kernel filter<sup>76, 77</sup> to reduce background noise before being fed into the 2D-particle tracking algorithm. The algorithm determined the particles' positions by least-square fitting their logarithmic intensities in the 3×3 binning area directly into a Gaussian curve:

$$\log I_p(x, y) = \log(I') - \frac{(x - \mu'_x)^2 + (y - \mu'_y)^2}{2 \times R'_a{}^2}, \quad (3-1)$$

where the fitted peak intensity determines the particle's sub-pixel position,  $(\mu'_x, \mu'_y)$ , within the central pixel of the binning area (the origin, (0, 0), is set to the center of the pixel). In Eq. (3-1),  $I_p$  represents the pixel intensity of a particle and the fitted parameters,  $I'$ ,  $R'_a$ ,  $\mu'_x$ , and  $\mu'_y$  represent the particle's peak intensity, apparent radius, and the position in the x- and y-direction of a Cartesian plane, respectively. These results indicate that the positioning error strongly depends on the EM gain setting in a manner that depended on the intensity of the tracked object (Fig. 3-1). Choosing an EM gain of 2000 increased the positioning error by as much as 48% (subcellular body #6) and decreased it by 44% (subcellular body #3).

### 3.2.2 EM Gain Characterization

The above result suggested that an optimal EM gain setting might exist to achieve the minimal positioning error in particle tracking. Thus, a method to characterize the EM gain performance is developed. Previously, we established a method to estimate the

positioning error of particle tracking in an acquired image using Monte Carlo simulation. This method requires the information of a pixel's SNR profile over the whole intensity range. A quantitative mapping between the intensity-dependent SNR and the EM gain is derived as discussed below. This discussion will define many variables that are summarized in Table 1 for reference.

The derivation accounted for the conversion of incident photons into final pixel intensity (Fig. 3-2A). Consider  $N_p$  as the average number of photons per pixel that are incident on the CCD camera coming from the observed object.  $N_p$  photons give rise to  $N_{PE}$  electrons. In addition,  $N_{DE}$  electrons, dark current, are generated over time by thermal energy within the CCD camera, which are independent of the incident light on the detector<sup>78</sup>. Next, a fixed value of EM gain,  $k$ , which depends on the applied voltage<sup>21</sup>, amplifies the electrons by a multiplication factor,  $G_{EM,k}$ . This multiplied electron signal is ultimately sent to the analog-digital converter that converts electron signals to an intensity count by a factor,  $G_{ADC}$ , with an offset,  $I_{offset,k}$ , to give the final average digital intensity per pixel,  $I_{out,k}$ . The described signal processing in an EMCCD camera can be mathematically represented as:

$$I_{out,k} = (N_{PE} + N_{DE}) \times G_{EM,k} \times G_{ADC} + I_{offset,k} \quad (3-2)$$

Because the magnitude of dark current electrons increases with the exposure time<sup>79</sup>, the effect of dark current electrons can be mitigated by decreasing the exposure time of the analyzed image. However, as seen in Eq. (3-2), the signal from dark current is multiplied by the effective EM gain,  $G_{EM,k}$ ; hence, its effect on the magnitude of the output cannot be omitted at high  $k$ . Since the  $I_{offset,k}$  value does not change with the

binning setting of the CCD camera, which can boost the dark current signal several times depending on the integrated pixels, the level of binning is adjusted without incident light and used linear fitting to obtain the  $I_{offset,k}$  in Eq. (3-2).

At ground state ( $k = 0$ ), Eq. (3-2) can be rearranged as:

$$(N_{PE} + N_{DE}) = (I_{out,0} - I_{offset,0}) / (G_{EM,0} \times G_{ADC}). \quad (3-3)$$

Substituting Eq. (3-3) into Eq. (3-2) with  $G_{EM,0} = 1$ , we get the following relation between the output intensity under electron multiplication ( $I_{out,k}$ ) and that in the ground state ( $I_{out,0}$ ):

$$I_{out,k} = G_{EM,k} \times I_{out,0} + I_{offset,k} - G_{EM,k} \times I_{offset,0}. \quad (3-4)$$

We acquired images at varying light source intensities at a fixed  $k$ , and measured average  $I_{out,k}$  per pixel (for 100,000 pixels) corresponding to the different light intensities. These experiments were repeated for identical light source intensities at  $k = 0$ . This resulted in a series of data points ( $I_{out,0}, I_{out,k}$ ) corresponding to different light source intensities that were plotted for  $k$  values varying from 1000 to 4000 (Fig. 3-2B). As seen in Fig. 3-2B, the  $I_{out,k}$  saturates at high light source intensities. Since Eq. (3-4) only represents the relation between  $I_{out,0}$  and  $I_{out,k}$  before  $I_{out,k}$  becomes saturated, this equation is used to fit unsaturated data points, which fit the data smoothly. Thus, the values of  $G_{EM,k}$  were estimated at different values of  $k$  and tabulated in Table 3-1. Notably, the relationship between the effective gain  $G_{EM,k}$  and  $k$  is not linear based on these trends.

We next derived a quantitative relation between the variance in the measured intensity  $I_{out,k}$  and effective EM gain  $G_{EM}$ . To do this, we accounted for noise propagation in the conversion process of  $N_P$  photons to the variance in the final  $I_{out,k}$ . First, photon shot noise and dark current noise occur when photons are detected in each pixel, and their variances are equal to the signal magnitude<sup>78</sup>. This variance is given by  $\sigma_{PS}^2 = \text{var}(N_{PE} + N_{DE}) = N_{PE} + N_{DE}$ . Electron multiplication further increases the variance by  $G_{EM,k}^2$ . In addition, the EM amplification process introduces an accumulated variance ( $F_k^2$ ; where  $F_k$  is called the excess factor) into the signal, which is generated from all the register steps<sup>21</sup>. Finally, the analog to digital converter converts the electronic signal to an output intensity count by the multiplication factor,  $G_{ADC}$ , also generating an additional signal independent read-out variance,  $\sigma_R^2$ . This leaves a total pixel intensity variance,  $\sigma_{out,k}^2$ , described by:

$$\sigma_{out,k}^2 = (N_{PE} + N_{DE}) \times G_{EM,k}^2 \times G_{ADC}^2 \times F_k^2 + \sigma_R^2. \quad (3-5)$$

Substituting the intensity count for the electronic signal, we get:

$$\sigma_{out,k}^2 = I_{out,k} \times G_{EM,k} \times G_{ADC} \times F_k^2 + \sigma_R^2 - I_{offset,k} \times G_{EM,k} \times G_{ADC} \times F_k^2. \quad (3-6)$$

In the above equation, the value of  $G_{EM,k}$  is already known from the previous measurements and fitting. We next measured  $\sigma_{out,k}^2$  as half of the variance of the pixel intensities in the image obtained from two repeated image subtractions (we accounted first for pattern noise, which is systematic variation in pixel intensities). Eq. (3-6) was fit to the measured values of  $\sigma_{out,k}^2$  and  $I_{out,k}$  at  $k = 0$  where  $F_0 = 1$ ; this allowed for the estimation of  $G_{ADC}$  as 1.75 au per electron. This value was not expected to change as a

function of k; therefore, it is assumed constant for fitting Eq. (3-6) to the data at non-zero values of k (Fig. 3-2C). This allowed us to estimate the excess factor,  $F_k$ .

In the high intensity region, the variance obtained by experiments was smaller than that of the theoretically estimated value. This is presumably a result of image saturation. The theoretical calculation does not take the saturation into account; hence, the estimated variance can represent the total shot noise and readout noise at high incident photon levels. In a real case, a signal with intensity higher than the maximum pixel output can cause the pixel to only export that maximum output value, giving rise to a signal loss. Thus, the mean and variance of the output intensity count will be underestimated as the intensity count approaches saturation.

### 3.2.3 The Signal to Noise Ratio (SNR) can be used to Optimize the EM Gain Setting

One can also easily derive the SNR at various incident photon magnitudes as:

$$SNR = N_{PE} \times G_{EM,k} \times G_{ADC} / \sqrt{((N_{PE} + N_{DE}) \times G_{EM,k}^2 \times G_{ADC}^2 \times F_k^2 + \sigma_R^2)}. \quad (3-7)$$

With short acquisition times, the dark electron effect can be neglected. The  $N_{PE}$  value can be calculated by Eq. (3-2) using the value of  $I_{out,k}$ . Therefore, we can estimate the theoretical SNR for different  $N_{PE}$  at a given EM-setting from Eq. (3-7) since all parameters in this equation are known (Table 3-1). As a result, the theoretical SNR for k = 2000 can be calculated over whole working range of light intensity. Meanwhile, this value can also be obtained from the value of  $(I_{out,2000} - I_{offset,2000}) / \sigma_{out,2000}$ , where  $I_{out,2000}$  and  $\sigma_{out,2000}$  can be measured experimentally. A comparison (Fig. 3-3A) shows that the experiments were in very good agreement with the theoretical estimates.

This allowed us to estimate the SNR response for different EM gain settings from Eq. (3-7) at varying magnitudes of intensity. Comparison for the same amount of light intensity (i.e.  $I_{out,0}$ ) but at different k values (Fig. 3-3B) indicates that changing the EM gain setting can result in different SNR values under identical illumination. At higher incident photon levels, SNR can be simplified to  $\sqrt{N_{PE}} / F_k$  by neglecting the readout noise in Eq. (3-7). Hence, no single EM gain achieved the best performance as predicted by the minimization of the excess factor (Fig. 3-3B), but at lower  $N_p$ , increasing k enhances the SNR (Fig. 3-3B inset). The improvement of the SNR at low  $N_p$  plateaus when k is above 2000 for the experimental imaging system, and the SNR crossover takes place around  $I_{out,0} = 1800$  au (Fig. 3-3C).

#### 3.2.4. EM Gain Effects on Multi-Pixel Analysis

The above study revealed the capability of EM gain to improve the SNR at the single pixel level when the intensity of incident light is low, but that it has the opposite effect when the light intensity is high. The extent to which this can influence spatial resolution during particle tracking where multiple groups of pixels are analyzed is unclear. The different pixels may possess various intensities, and the EM process could introduce spatially varying error in the analysis. We therefore determined the effect of EM gain on the positioning error ( $\varepsilon_s$ ; or spatial resolution) of particle positioning of a 100-nm particle using a Monte Carlo method published previously<sup>75</sup>.

A Gaussian particle with a fixed radius was assigned different peak intensities sequentially to mimic real system conditions. Furthermore, proper magnitudes of random noise corresponding to the noise profile of the assigned signal intensity under the specified EM gain condition, were added to each pixel in the simulation<sup>75</sup>. Fixed

pattern noise in our CCD camera has a minimal effect on particle resolution as demonstrated from Monte Carlo simulations (data not shown). Therefore, this type of noise was omitted from further simulations while identifying the  $\varepsilon_S$  of a particle. The extracted  $\varepsilon_S$  values correspond to varying particle peak intensities ( $I_{peak}$  denotes the peak intensity at  $k = 0$ , see Fig. 3-4A), showing that EM gain can significantly improve  $\varepsilon_S$  by more than 10 fold when the  $I_{peak}$  of the object is lower than 100 au. This EM gain effect decreases gradually and eventually reverses at high  $I_{peak}$  ( $\geq 2000$  au). For example, a Gaussian particle with  $I_{peak}$  of 15,000 au possesses 2.3 times smaller  $\varepsilon_S$  at  $k = 0$  than at  $k = 2000$ . Saturation of a pixel can occur when the  $I_{peak}$  of a Gaussian particle is high, and this caused a fluctuating and irregular correlation between  $\varepsilon_S$  and  $I_{peak}$  in the simulation results.

To understand the above phenomenon in more detail, we estimated the critical  $I_{peak}$  value ( $I_{C,k}$ ), which is the intersection point of the  $\varepsilon_S$  curves in Fig. 3-4A at  $k = 0$  and another EM gain setting  $k$  (Fig. 3-4B). Due to the adverse effect of EM gain on  $\varepsilon_S$  in object positioning at high intensity levels, the figure suggests a boundary (the  $I_{C,k} - k$  curve) to separate the regions between where EM gain activation is beneficial for object positioning and where it is not. The profile also sets a quantitative standard for applying adequate EM gain. It is important to note that increasing the EM gain reduces the working range of photon acquisition and therefore leads to a smaller working range of  $I_{peak}$  values.

### 3.2.4.1 Optimal EM Gain Depends on the Size and Background Intensity of the Object

The above study suggests that the  $I_{C,k}$  value depends on  $k$  and can help determine whether EM gain should be applied to improve the resolution of a quantitative biophysical assay probing an object with known  $I_{peak}$ . To explore whether other physical parameters of the object also affect the  $I_{C,k}$  value in particle tracking, the simulated Gaussian particle was used as an ideal and simplified model for mimicking cellular components. Different levels of background signal ( $I_{BG}$ ) were assigned to the simulation to examine how  $I_{C,k}$  changes with  $I_{BG}$ . The results showed that an increase in  $I_{BG}$  leads to a decrease in  $I_{C,k}$  and when the  $I_{BG}$  exceeds 900 au, both the  $I_{C,1000}$  and  $I_{C,2000}$  drop approximately to zero (Fig. 3-5A). Therefore, high background images reduce the advantage of EM gain activation.

We next evaluated the effects of particle size and sub-pixel location on  $I_{C,k}$ . Gaussian particles with different sizes or sub-pixel locations were used again as a simplified model. The simulated results suggested that the  $I_{C,1000}$  and  $I_{C,2000}$  values drop quickly with increasing apparent radius of an object (Fig. 3-5B) but the sub-pixel location of the Gaussian bead does not have a significant effect on the  $I_{C,1000}$  and  $I_{C,2000}$  values (data not shown). In essence, these studies demonstrate that the EM gain is most effective in a biophysical assay such as particle tracking and positioning when the object possesses a small radius, low peak intensity, and low background intensity.

### 3.2.4.2 Particle Tracking Experiments Verify the EM Gain Effect on Image Analysis

These simulation results were verified through the tracking of fixed 100-nm fluorescent microspheres. The  $\varepsilon_{S,k}$ , based on the positioning error in 600 trials of positioning a fixed microsphere, were determined at a fixed EM gain. An x - y diagram was used to describe the results (Fig. 3-6). The x-axis represents the  $\varepsilon_{S,0}$ , while the y-axis represents the  $\varepsilon_{S,1000}$ . In this case, the straight line,  $x = y$ , divides the diagram into two regions: above the line, there is a detrimental EM gain effect (i.e.,  $\varepsilon_S$  becomes larger when EM gain is activated) and below the line, there is a beneficial EM gain effect (i.e.,  $\varepsilon_S$  becomes smaller when the EM gain is activated). If the  $\varepsilon_{S,k}$  value falls on the line, then it means that EM gain has no significant effect on the  $\varepsilon_S$ . Since the concentration of the microspheres can contribute to the  $I_{BG}$ , a sample with a high concentration of fixed, out-of-focus fluorescent microspheres was used to create a high  $I_{BG}$ , which was 2000 au higher than the dark current under the full power of the UV light source. Under such conditions, 35 in-focus particles were tracked (shown as hollow squares) to assess their  $\varepsilon_{S,0}$  and  $\varepsilon_{S,1000}$  values. In parallel, 43 fixed, fluorescent microspheres were tracked in samples with lower particle concentrations and lower excitation light intensity (shown as solid circles), which produced low  $I_{BG}$  (= 1200 au, which contains the intrinsic  $I_{offset,k}$  value, see Eq. (3-2)) and low  $I_{peak}$  (lower than 2000 au). Results obtained from these experiments confirmed that EM gain performance on the  $\varepsilon_S$  of particle-tracking experiments depends on  $I_{BG}$  and  $I_{peak}$ , and that EM gain can damage the resolution of experiments at higher  $I_{BG}$ .

### 3.3 Discussion

#### 3.3.1. The Working Range and Effectiveness of EM Gain

In previous chapter it is demonstrated that accuracy in particle-positioning relies heavily on a high SNR in acquired images<sup>75</sup>. Here, we further explored how the EM gain settings in a CCD camera can affect the SNR in acquired images. Modification in an established method<sup>78</sup> quantified the dependence of the SNR values on the EM gain,  $k$ , of an EMCCD camera and evaluated to which extent the EM gain could affect the outcome of a particle tracking experiment. After comparing the SNR values for different  $k$  values over a full range of incident light, I concluded that the EM gain only enhances the SNR of an output signal when the incident light intensity is lower than a certain critical level (in this case, it is 1900 au as measured at  $k = 0$ ). When the incident light intensity is higher than that critical level, it will diminish the SNR value and damage the fidelity of particle tracking results. I also concluded that the working range of a particle tracking experiment is determined by the maximum  $I_{peak}$  of a group of tracked particles because the electron multiplication of the brightest particle will more quickly result in saturation of the amplified maximum peak intensity ( $I_{out}$ ), reducing accuracy in particle positioning. The maximum  $I_{peak}$  values allowed in our system are 12,840, 1,910 and 71 au (using  $k = 0$  as a reference) for  $k = 2000, 3000$  and  $4000$ , respectively. This demonstrates that the working range for EM gain in particle tracking diminishes quickly with increasing EM gain when  $k$  is larger than 2000.

Although the maximum pixel intensity allowed before saturation at  $k = 2000$  is over 10,000 au in our experimental system as suggested in data shown in Fig. 3-4A, the simulation results suggest that the smaller positioning error compared to that at  $k = 0$  for

particle tracking occurs only when the  $I_{peak} \leq 6000$  au. Hence, application of the highest k allowed by the working range will not necessarily produce the most accurate tracking result. Presumably this is because particle tracking needs to quantitatively analyze the intensity profile over a group of pixels to identify the position or boundary information. Since the SNR of a pixel at different intensities does not linearly depend on the EM gain setting, the relative intensities among the group of pixels representing the object of interest are quantitatively altered, changing the outcome of their calculated positions.

### 3.3.2 Analysis of the Estimated Values in this Study

In my evaluation, the extraction of the  $G_{ADC}$  value plays a critical role to determine the excess factor,  $F_k$ . The range of  $G_{ADC}$  within a 95% confidence interval was found to be 0.028, representing 3.96 times its standard deviation. The standard deviation of  $G_{ADC}$  estimated from this information is 0.007, which is 0.4% of its mean value. This can be quickly verified by calculating the standard deviation for  $G_{ADC}$  using four independent trials, which was found to be less than 0.8%. Therefore, using the extreme values of  $G_{ADC}$  (2 standard deviations from the mean), we could estimate the range of excess factor,  $F_k$ , which was found to be within 0.98 ~ 1.02 times its mean value, or approximately within 2% of the mean in all different conditions. From this analysis, we expect that other parameters that can be derived based on the extracted  $G_{ADC}$  value will also possess very little deviation from their mean values.

### 3.3.3 Assessment of EM Gain in Subcellular Particle Tracking Experiments

The signal is highly sensitive to the EM gain setting, and the results suggest that the EM gain is not very useful for tracking particles that are typically brightly visible and

clearly defined in the image (such as YFP-sumo). These imaging experiments provide an example to demonstrate this phenomenon. A PML-nuclear body labeled by YFP-sumo has high background intensity, presumably caused by the freely diffusive YFP-sumo molecules in the nucleus<sup>80</sup>. This nuclear body also has high intensity and large radius. Therefore, it is not beneficial to track YFP-sumo-labeled PML-nuclear bodies using an EM gain setting. In contrast, electron multiplication favored the tracking of GW-bodies with dimmer intensities and possessing smaller radii. This study provides direct evidence to demonstrate that the EM gain setting of the EMCCD camera can significantly influence the positioning error during subcellular particle tracking.

### **3.3.4 Application of Proper EM Gain to Biophysical Measurements beyond Particle Tracking**

Many biophysical studies utilize signals generated from GFP or their derivatives. The applications of GFP in quantitative cellular biophysics are very powerful but are challenging at low intensities. If the GFP molecules emit light with low intensity, the acquired image possesses a low SNR value and the accuracy of the biophysical assay is reduced. On the other hand, if the exposure time is increased, photo-bleaching effects become unavoidable. In most cases, it is best to minimize the UV-light exposure so a consistent signal output can be maintained. Therefore, a proper EM gain setting could greatly improve the accuracy of biophysical assays for low-intensity signals. Electron multiplication can effectively reduce the required image intensity and extend the possible experimental time frame without affecting spatial resolution. Under optimal EM gain settings, the pixel intensity can be more reliably measured for photon counting histogram analysis<sup>18</sup>. In this regard, the EMCCD camera can be used to improve the detection of molecular fluctuations in micro-scale volumes and improve the reliability of

fluorescence correlation spectroscopy (FCS)<sup>81</sup> or concentration measurements<sup>20</sup>. In these types of studies, the EM gain feature is critical to successfully amplify the photon fluctuation to overcome readout noise since the photon count in the pixel is usually small.

In an effort to achieve the highest accuracy in microscopy-based biophysical measurements, a standard procedure to analyze the EM gain settings of a CCD camera is developed in this study. These quantitative cellular biophysical assays usually focus on imaging subcellular dynamics. Often, a quantitative measurement is required, and the accurate positioning of the subcellular object in image analysis becomes a critical step for the success of the biophysical assay. The parameters that can affect EM performance include the exposure time of image acquisition (temporal resolution), the background intensity and shape of the probed object. To be applicable to a broad range of experimental situations, this EMCCD characterization must be available for a variety of particle shapes, sizes and intensities. The method that is provided in this study is theoretically suitable for all types of EMCCD camera. Since the intensified CCD (ICCD) camera has similar signal amplification processing (photon signal is enhanced first in a similar way and sensed by CCD chip later) but a different physical mechanism; it is expected that some minor modifications to our method may be required to accurately assess the optimal settings for an ICCD camera. However, further verification is required. Nevertheless, this study provides a method to quantitatively choose the appropriate EM gain for maximizing the resolution of biophysical assays. The optimization procedure presented here should greatly improve the accuracy of such measurements.

### 3.5 Conclusion

The EM gain magnifies the photon-signal-induced electron flow in individual pixels of a CCD camera. A higher EM gain can generate more output from the pixel until the pixel reaches its maximum output capacity (saturation). This saturation sets the working range that should be used when amplifying the incident signal. A quantitative method to assess the outcome after using EM gain and evaluate its effectiveness in a biophysical assay is essential to ensure high resolution in subcellular measurements. Therefore, EM gain effects on simulated Gaussian shaped particles are investigated here to gain an understanding of the optimal EM gain settings in cellular particle tracking.

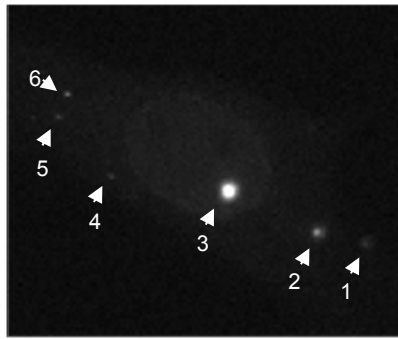
This model system is adopted for three purposes. First, particle tracking is a powerful technique in cellular biophysics. Information gained from this approach can have a direct and immediate impact on the particle tracking community. Second, a Gaussian shaped particle is relatively easy to evaluate. Hence, results obtained from this model can be more easily verified than other models. Last, the evaluation procedure developed by use of this model can be extended as a platform to explore the effectiveness of EM gain on biophysical studies of cellular components with more complicated features.

Table 3-1. The values of the effective EM gain (k), excess factor

Notation (unit)	Description	Notation (unit)	Description
$I_P$ (au)	Pixel intensity of a particle	$I'$ (au)	Fitted particle's peak intensity
$R'_a$ (px)	Fitted particle's apparent radius	$\mu'_x$ (px)	Fitted particle's position in x-direction
$\mu'_y$ (px)	Fitted particle's position in y-direction	$N_P$ (photon)	Average number of incident photons per pixel on the CCD camera
$N_{PE}$ (e <sup>-</sup> )	NP photons give rise to photo-activated electrons	$N_{DE}$ (e <sup>-</sup> )	Dark current electrons
$k$ (-)	EM setting parameter for image acquisition	$G_{EM\ k}$ (-)	Electron multiplication gain at EM setting $k$
$G_{ADC}$ (au/e <sup>-</sup> )	Analog to digital converter gain	$\sigma_{PS}^2$ (e <sup>-2</sup> )	Photon shot noise
$I_{offset\ k}$ (au)	Pixel intensity offset value at EM setting $k$	$I_{out\ k}$ (au)	Average output digital intensity per pixel at EM setting $k$
$F_k$ (-)	Excess factor	$\sigma_R^2$ (au <sup>2</sup> )	Read-out noise
$\sigma_{out\ k}^2$ (au <sup>2</sup> )	Total pixel intensity variance	$\varepsilon_{S\ k}$ (px <sup>2</sup> )	Spatial resolution in particle tracking
$SNR$ (-)	Signal to noise ratio	$I_{peak}$ (au)	Peak intensity of Gaussian particle at $k = 0$
$I_{C\ k}$ (au)	Critical $I_{peak}$ value at EM setting $k$	$I_{BG}$ (au)	Background intensity
$R_a$ (px)	Gaussian particle size		

Table 3-2. The values of the effective EM gain (k), excess factor (F), intensity offset ( $I_{offset}$ ), and relative working range at several EM gain settings estimated for our system.

$K$	Effective EM gain ( $G_{EM}$ )	Excess factor ( $F$ )	$I_{offset}$ (au)	Relative working range to zero EM gain (%)
0	1.00	1.00	1095.2	100.0
200	1.31	1.14	1383.1	75.9
500	1.47	1.17	1406.8	67.7
1000	1.90	1.24	1450.0	52.4
1500	2.80	1.29	1499.4	35.5
2000	4.98	1.34	1551.4	19.9
3000	33.41	1.41	1693.6	3.0
4000	878.82	1.38	2998.1	0.1



Obj	positioning resolution ( $\mu\text{m}^2$ )		ratio
	$k=0$	$k=2000$	
1	$3.01 \times 10^{-3}$	$2.31 \times 10^{-3}$	1.30
2	$5.02 \times 10^{-4}$	$5.04 \times 10^{-5}$	1.00
3	$9.77 \times 10^{-5}$	$1.74 \times 10^{-4}$	0.56
4	$1.12 \times 10^{-2}$	$1.36 \times 10^{-2}$	0.83
5	$5.35 \times 10^{-3}$	$3.72 \times 10^{-3}$	1.44
6	$1.68 \times 10^{-3}$	$1.14 \times 10^{-3}$	1.48

Figure 3-1. EM gain causes contradictory effects on the spatial resolution of protein clusters. An NIH 3T3 fibroblast expressed two different proteins, GFP-Ago2 and YFP-Sumo1, forming two types of protein complexes containing one kind of fusion protein each. These speckle-like complexes ( $n = 6$ ) were tracked to analyze the positioning error after the cell was fixed by formaldehyde. The analyzed results are listed in the table beside the image with the object numbers designated in the image. The effects of EM gain (at  $k = 2000$ ) on the resolution (presented by the variance of tracked positions) was listed as the ratio of the positioning resolution at  $k = 0$  to  $k = 2000$  (far right column).

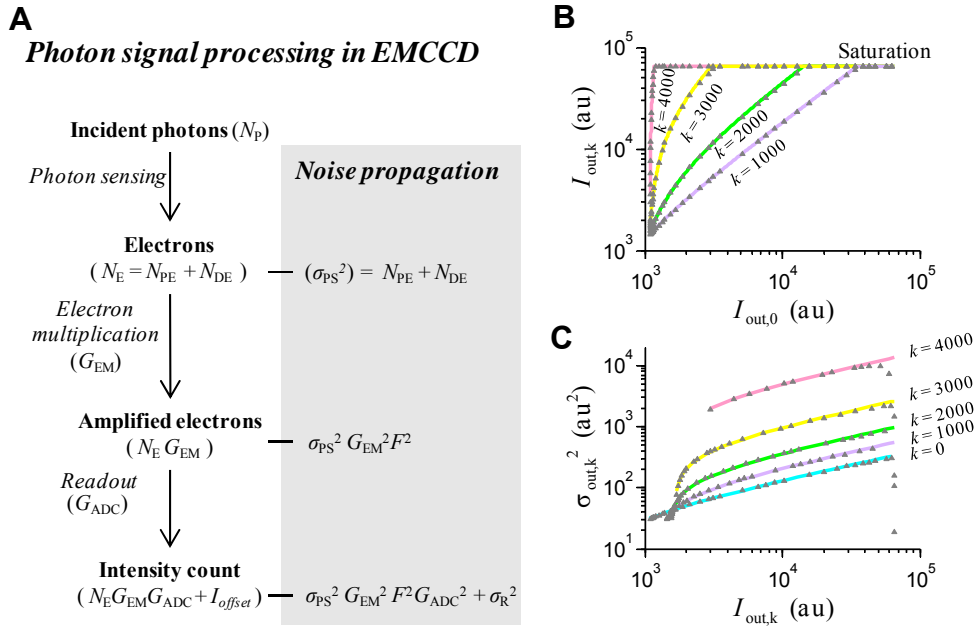


Figure 3-2. EM gain parameters are determined experimentally. (A). Schematic plot of photon conversion and noise propagation in the EMCCD camera. (B). Logarithmic plot of intensity count ( $I_{out,k}$ ) at different EM gain ( $\blacktriangle$ ) versus  $I_{out,0}$  under varying light intensities. The solid line represents the least squared fitting results to the linear model. Actual electron multiplication gain can be estimated from the slope of fitted model. (C). Scatter plot of  $\sigma_{out,k}^2$  versus  $I_{out,k}$  at  $k = 0, 1000, 2000, 3000$  and  $4000$  in the logarithmic scale. Linear model fitting results at different EM gain are shown as a solid line and agree well with experimental data.  $R^2 > 0.99$  for all fitted models.

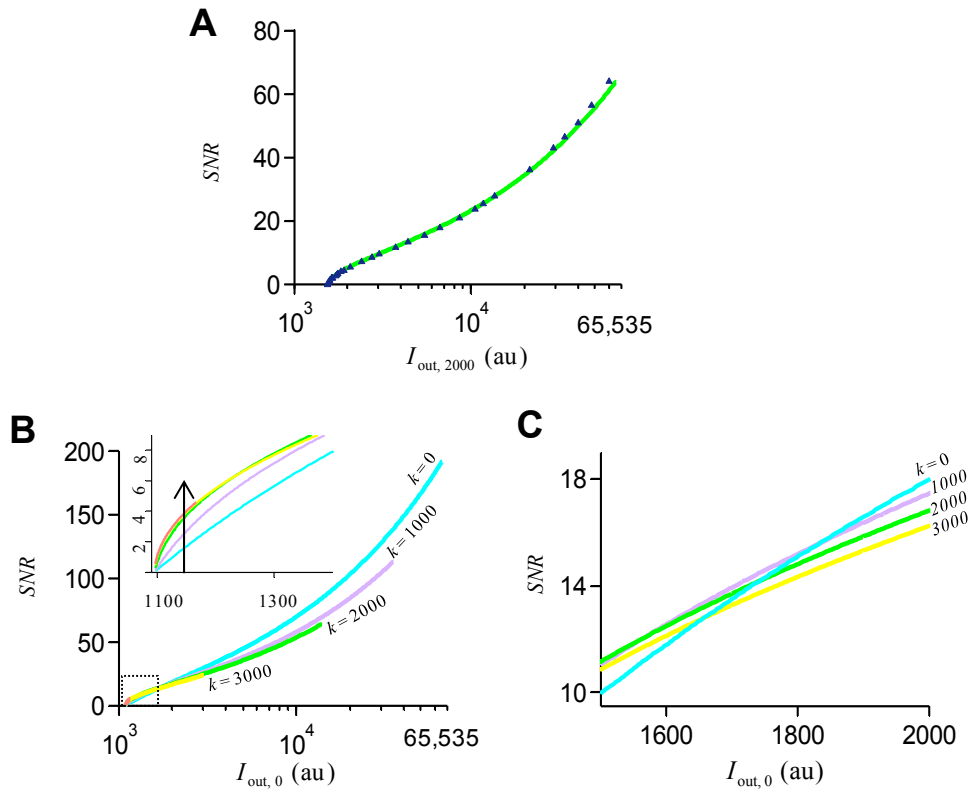


Figure 3-3. The optimal setting of the EM gain depends on the intensity of the signal. (A) The correlation between SNR and  $I_{out,k}$  is plotted for  $k = 2000$ . The theoretically derived SNR curve (solid line) agrees well with experimental data ( $\blacktriangle$ ). (B) Values of the SNR at different EM gain ( $k = 0, 1000, 2000, 3000$  and  $4000$ ) are determined theoretically and plotted at the same amount of light intensity as  $I_{out,0}$ . At a high incident light intensity, the highest SNR is at  $k = 0$ , and the SNR decreases with increasing  $k$ . Inset: the region marked by the dashed box in panel B is shown in more detail. The arrow points in the direction of increasing  $k$ . (C). The SNR crossover between  $k = 0$  and a given  $k$  occurs around  $I_{out,0} = 1800$  au.

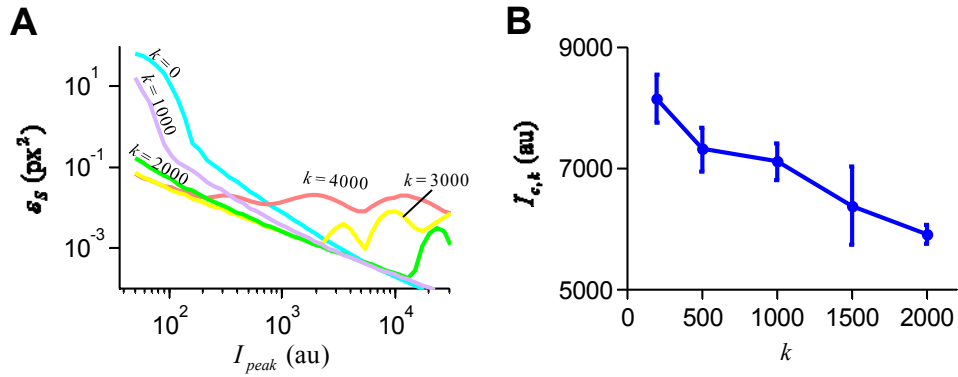


Figure 3-4. The relation of the  $k$  and  $\epsilon_s$  is affected by  $I_{peak}$ . (A) The EM gain setting affects the  $\epsilon_s$  dependency on  $I_{peak}$ . These results show that EM gain effectively improves the  $\epsilon_s$  at low signal intensity, but the effect diminishes with increasing  $I_{peak}$  of the objects. After the  $\epsilon_s$  at a certain  $k$  crosses over that of  $k = 0$  ( $I_{peak} \sim 2000$  au), a contrary effect occurs. (B) The crossover points of the peak intensity at the junction of the positioning error curves of non-zero  $k$  and at  $k = 0$  (●) depend on  $k$ . The crossover points set an upper bound as the critical points for the highest  $I_{peak}$  values at a certain EM gain; at  $I_{peak} < I_{c,k}$ , one can still take the advantage of EM gain to reduce the positioning error in particle tracking experiments. The error bar is the standard deviation from five individual simulation results.

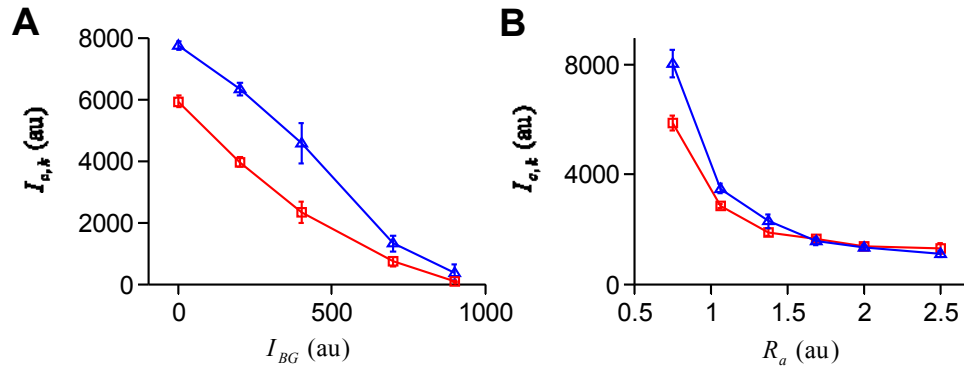


Figure 3-5. The EM gain performance in particle tracking depends on experimental conditions. (A) Background intensity,  $I_{BG}$ , affects the  $I_{C,k}$  significantly. With  $I_{BG} > \sim 900$  au, the EM gain will not improve the  $\varepsilon_S$  for particle tracking. (B). A large apparent radius of particle,  $R_a$ , also affects the  $I_{C,k}$  significantly. Open triangles ( $\triangle$ ) and open squares ( $\square$ ) correspond to  $k = 1000$  and  $2000$ , respectively.

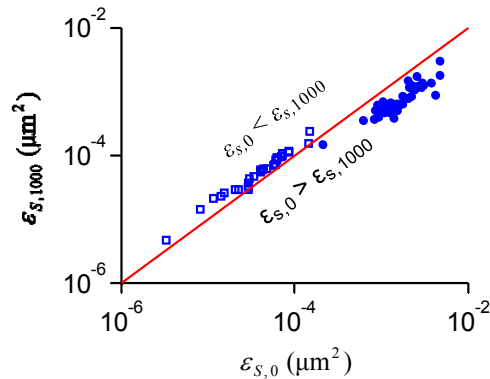


Figure 3-6. Plot of  $\varepsilon_{S,1000}$  vs.  $\varepsilon_{S,0}$ . Two experimental conditions were chosen: 35 microspheres at high  $I_{peak}$  at 100 % light source intensity ( $\square$ ) and 43 microspheres at low  $I_{peak}$  at 25% power of light source intensity ( $\bullet$ ). The solid line corresponds to  $\varepsilon_{S,1000} = \varepsilon_{S,0}$ . Zero EM gain causes a 23% ( $\pm 10\%$ ) improvement in positioning error at 100 % light source intensity in which  $I_{peak}$  is larger than 10,000 au and background intensity is  $\sim 5000$  au. On the other hand, EM gain ( $k = 1000$ ) improved the positioning error by 46% ( $\pm 11\%$ ) for the particle with small  $I_{peak}$  ( $\sim 1000$  au) and minimal background ( $I_{BG} \sim 0$  at 25% light source intensity).

## CHAPTER 4 ANALYSIS OF VIDEO-BASED MICROSCOPIC PARTICLE TRAJECTORIES USING KALMAN FILTERING

### 4.1 Background

Cellular dynamics controls cell physiology<sup>22, 23</sup>. This dynamics process includes not only protein diffusion and transport but also the intracellular organelles motion<sup>22, 24</sup>. Meanwhile, the invasion process of bacteria in the intracellular region of mammalian cells has also been discovered to involve in the intracellular dynamics of the host cells<sup>25</sup>. Therefore, to understand the molecular mechanisms of a subcellular event, the cellular dynamics plays a critical role and cannot be ignored. The most direct way to study a cellular dynamics process is to monitor the physical motion of the observed object, and to further correlate this motion to the biochemical functions of the composed proteins of the object. For example, the analysis of the step size of the cargo-motor protein transport led to the understanding of how the motor proteins function<sup>26-29</sup>. The connection of the bacteria motion to the function of bacterial protein, ActA, elucidates how bacteria move inside the intracellular region of the host<sup>30, 31</sup>. In these studies, particle tracking serves as the most direct method for studying the real time movement of objects of interest in live cells.

Particle tracking has been applied to study various subcellular events, such as genomic dynamics<sup>32</sup>, viral infection<sup>33, 34</sup>, cellular endocytosis<sup>35</sup>, membrane protein trafficking<sup>36</sup>, and cargo transport<sup>37</sup>. Besides the study of the dynamic events of a live cell, particle tracking is also applied to probe the mechanical properties of the intracellular region of the live cells through the particle tracking microrheology<sup>38</sup>, which analyzes the fluctuations in displacement of an inert particle embedded in the cytoplasmic region of a live cell at different time lag. Through the microrheology

theorem<sup>39,40</sup>, the rheological properties of a cell, such as creep compliance, elastic modulus, and viscous modulus, can be explored<sup>38,41</sup>. Compared to other existing techniques, such as atomic force microscopy, intracellular microrheology imposes a minimized perturbation to acquire the physical properties of the intracellular region of the cells. Using this technique, the mechanical properties of various cell lines under different extracellular stimuli (chemical<sup>41</sup> and mechanical<sup>42</sup>) and microenvironmental topology (two-dimensional vs. three-dimensional<sup>43</sup>) can be probed.

Since the particle-tracking technique can contribute valuable insights into many biological events, the accuracy of particle tracking is critically important for the effectiveness of those studies. However, in a particle tracking experiment the sensor noise in the image acquisition system is transformed into a positioning error. As a result, the computed particle trajectory is a noisy version of the true particle trajectory. This hinders a deeper analysis of the trajectory aimed at gaining detailed insights into the dynamic processes related to the observed object (Fig. 4-1)<sup>76</sup>. Accordingly, many advanced instruments were recently developed, which improve the spatial resolution of tracking techniques<sup>19,20</sup>. However, signal filtering and estimation algorithms offer an alternative route to reducing the extraneous noise associated with particle trajectories. These algorithms can be applied regardless of the underlying instrumentation, and thus provide a general approach that can effectively enhance the spatial resolution of particle tracking.

Deriving states of a dynamic system from noisy measurements is a very well-researched problem in control and estimation theory. In particular, the Kalman filter algorithm provides the optimal state estimate for linear dynamic systems from sensor

measurements in the presence of Gaussian noise. The Kalman filter has been successfully applied in a wide variety of situations in engineering and science<sup>44, 45</sup>. The potential use of a Kalman filter to study cell motion has been mentioned in passing<sup>46</sup>. In this paper, we explore in detail the application of the Kalman filter algorithm to improve the estimation of the particle trajectory obtained from a microscopic particle tracking experiment.

At first, it is demonstrated that the Kalman filter can be used to infer intrinsic (noise-free) trajectories. Second, we explain how the input parameters (the variance of process and measurement noise) necessary for the design of the Kalman filter can be estimated for a given experimental situation. Third, we discuss the efficacy of Kalman filter in particle tracking. Finally, I examine *in vitro* particle tracking in glycerol and in a gliding motility assay to validate the application of the Kalman filter. It is concluded that the Kalman filter can effectively eliminate the positioning error generated by measurement noise if the noise variance parameters are chosen appropriately. As a result, the accuracy of the trajectory derived from particle tracking experiments is improved, which can provide the reliable biophysical information critical for the understanding of various biological processes.

## **4.2 Theory of Kalman Filtering in Particle Tracking**

### **4.2.1 The Parameters of the Kalman Filter Related to a Particle Tracking Trajectory**

Video-based particle tracking utilizes the visual information in a sequence of captured images to reconstruct the trajectories of labeled objects and determine their dynamical properties. The temporal resolution in a particle tracking experiment is determined from the time between each frame, represented by  $\Delta t$ . Individual image

frames in the tracking sequence can then be denoted by their respective time step,  $k$ , and a subscript of  $k$  can represent the state of a given variable at time  $k \times \Delta t$ . Conceptually, the position of a tracked object in a new frame is the result of a combination of active motion and random displacements due to thermal fluctuations that acted on the object over  $\Delta t$  since its previous position. In biological systems, the heterogeneous presence of obstacles restricts the magnitude of an object's velocity in a manner that intrinsically fluctuates. Thus, the change in position between time steps can be described by a constant directed movement,  $u_0$ , associated with a fluctuation,  $w_0$ , as well as the intrinsic thermal fluctuations. Using an ensemble fluctuation term,  $w_k$ , to account for  $w_0$  and the thermal fluctuations, the conceptual position,  $x_{k+1}$ , of a tracked object in a new frame can be formulated as:

$$x_{k+1} = x_k + u_0 + w_k. \quad (4-1)$$

This relationship between position, active motion and thermal fluctuations has been previously established in different forms<sup>82, 83</sup>. However, during the image acquisition process there is an intrinsic measurement noise,  $v_k$ , that distorts the measured position,  $z_k$ , from its conceptual value as described by:

$$z_k = x_k + v_k. \quad (4-2)$$

The Kalman filter is a recursive, computational method to make an estimate of the real state of the position,  $\hat{x}_{k|k}$ , from these types of noisy observations while preserving their intrinsic fluctuations<sup>84</sup>. However, having a better understanding of the parameters that govern the motion of an object is necessary before describing the major input factors of the Kalman filter. The measurement noise,  $v_k$ , is better defined as the positioning error, and is assumed to obey:

$$v_k \sim N(0, R_k), \quad (4-3)$$

where  $N(0, R_k)$  is the Gaussian distribution function describing white noise with a zero mean and a variance of positioning error,  $R_k$ . Similarly, the process noise  $w_k$  caused by thermal fluctuations is assumed to obey:

$$w_k \sim N(0, Q_k), \quad (4-4)$$

where  $N(0, Q_k)$  is also the Gaussian distribution function with zero mean and variance of thermal fluctuations,  $Q_k$ . In one-dimensional Brownian dynamics,  $Q_k = 2 \times D \times \tau$ , where  $D$  is the effective diffusivity of a labeled object and  $\tau$  is the diffusion time. If tracking object undergoes pure Brownian motion, the value of  $u_0$  is zero, and the value of  $w_k$  only represents the thermal fluctuations. In the case of directed motion, the magnitude of  $u_0$  can be experimentally estimated by calculating the average displacement between time steps, i.e.,  $u_0 = \langle z_{k+1} - z_k \rangle$ .

Taking all of this into account, the most important parameters of the Kalman filter are the raw trajectory information and the variance terms  $Q$  and  $R$ . The value of  $R$  for a tracked particle can be extracted as previously described<sup>75</sup>, but the value of  $Q$  must be attained using another method. The mean squared displacement (MSD) of the measured trajectory,  $z_k$ , is calculated as the variance of the measured displacement,  $S (\equiv \text{var}(dz))$ , and is related to  $Q$  and  $R$  by<sup>75, 76</sup>:

$$S = Q + 2 \times R. \quad (4-5)$$

Because noise from image acquisition does not directly influence the physical system of interest, the value of  $Q$  is independent of  $R$ , and this relationship serves as an explicit method to estimate  $Q$ .

#### 4.2.2 The Kalman Filter Gain is Determined by the Ratio $Q/R$ but not $Q$ or $R$

The Kalman filter uses a recursive procedure to estimate the true state of a linear process. It preserves the intrinsic fluctuations of the measured object while effectively removing the external noise. Here is a brief discussion of how to use this method to estimate the true trajectory from a measured trajectory obtained from the video-based particle tracking experiment. In the Cartesian coordinate system, the x- and y-components of a particle trajectory moving in the x-y plane are theoretically independent from one another; therefore, the use of the Kalman filter on a typical video-based particle tracking experiment can be simplified to a one-dimensional model of particle motion in each direction. Individual time steps of the Kalman filter process employ two distinct processing phases: predict and update. The elapsed time after onset is represented by  $k \times \Delta t$ , where  $k$  represents the observation time step. Any given variable with a subscript,  $k|l$ , is at time step,  $k$ , and in phase,  $l$ . When  $l = k - 1$  the variable is in its prediction phase, and when  $l = k$  the variable is in the update phase.

Using this format, the position at the current time step,  $\hat{x}_{k|k-1}$ , is first predicted by the sum of the previous position,  $\hat{x}_{k-1|k-1}$ , and the displacement,  $u_0$ , from either the freely diffusive or directed motion of the particle:

$$\hat{x}_{k|k-1} = \hat{x}_{k-1|k-1} + u_0. \quad (4-6)$$

Once the position,  $\hat{x}_{k|k-1}$ , is predicted, it is updated to a more accurate current position,  $\hat{x}_{k|k}$ , in the update phase. This is achieved by adding a correction term that uses an adjustable factor,  $K_k$ , to weigh the difference between the measured position,  $z_k$ , and  $\hat{x}_{k|k-1}$ :

$$\hat{x}_{k|k} = \hat{x}_{k|k-1} + K_k(z_k - \hat{x}_{k|k-1}). \quad (4-7)$$

The factor  $K_k$  is at its optimal value and referred to as the Kalman gain when the  $\hat{x}_{k|k}$  reaches the minimal error covariance,  $P_{k|k}$  ( $\equiv E((\hat{x}_{k|k} - x_k)^2)$ ). At this minimal value,

$$K_k = P_{k|k-1} (P_{k|k-1} + R_k)^{-1}, \quad (4-8)$$

where  $P_{k|k-1}$  ( $\equiv E((\hat{x}_{k|k-1} - x_k)^2)$ ) and  $R_k$  ( $\equiv E((z_k - x_k)^2)$ ) are the magnitudes of the error covariance for  $\hat{x}_{k|k-1}$  and  $z_k$ , respectively<sup>84</sup>. The thermal fluctuation,  $Q_k$ , propagates during this recursive process; therefore,  $P_{k+1|k}$  must also be updated at each time step:

$$P_{k+1|k} = P_{k|k} + Q_k. \quad (4-9)$$

In addition,  $P_{k|k}$  is concurrently updated with  $x_{k|k}$  in subsequent time steps:

$$P_{k|k} = P_{k|k-1} - K_k P_{k|k-1}. \quad (4-10)$$

Substituting Eq. 4-9 into Eq. 4-10, the discrete algebraic Riccati equation is obtained:

$$P_{k+1|k} = P_{k|k-1} - K_k P_{k|k-1} + Q_k. \quad (4-11)$$

In the one-dimensional particle tracking case,  $Q_k$  and  $R_k$  are considered to be independent of  $k$ , so that the number of variables is significantly reduced. Therefore,  $P_{k|k-1}$ ,  $P_{k|k}$  and  $K_k$  can reach their steady state values quickly. In a steady state,  $P_{k|k-1}$  and  $P_{k|k}$  are independent of  $k$ , and equal to each other, which can be denoted as  $P$ .

Together, Eq. 4-8 can be simplified as  $K = K_k = P (P + R)^{-1}$  and be further substituted into the simplified form of Eq. S6, which is expressed as  $KP = Q$ . Therefore, it yields

$$P^2 - QP - QR = 0. \quad (4-12)$$

Since  $P$  is the error covariance, it possesses a positive value. Thus, the solution of  $P$  in Eq. 4-12 is

$$P = Q/2 + \sqrt{Q^2 + 4QR}/2, \quad (4-13)$$

which leads to

$$K = \frac{(Q/R) + \sqrt{(Q/R)^2 + 4(Q/R)}}{2 + (Q/R) + \sqrt{(Q/R)^2 + 4(Q/R)}}. \quad (4-14)$$

Thus,  $K$  is solely determined by the value of  $Q/R$  but not the individual  $Q$ - and  $R$ -values.

#### 4.2.3 MSD Estimates from a Filtered Trajectory are Equal to the True State

When the Kalman filter is at its best performance, i.e., the correct  $Q/R$  value has been applied, the MSD value estimated by filtered position can be expressed as:

$$\hat{MSD} = E[(\hat{x}_{k|k} - \hat{x}_{k-1|k-1})^2]. \quad (4-15)$$

The expression of  $\hat{x}_{k|k}$  and  $\hat{x}_{k-1|k-1}$  in Eq. 4-10 and Eq. 4-11, respectively, is subsequently substituted into Eq. 4-15 and the following equation is obtained:

$$\hat{MSD} = E[(K(z_k - \hat{x}_{k|k-1}) + u_0)^2] = E[(K((z_k - x_k) + (x_k - \hat{x}_{k|k-1})) + u_0)^2]. \quad (4-16)$$

From Eq. 4-3 of the main text, we know that  $z_k - x_k = v_k$ . we further use  $\tilde{x}_{k|k-1}$  to represent  $(x_k - \hat{x}_{k|k-1})$  and obtain

$$\hat{MSD} = E[(K(v_k + \tilde{x}_{k|k-1}) + u_0)^2] = K^2 E[(v_k + \tilde{x}_{k|k-1})^2] + 2u_0 K E[(v_k + \tilde{x}_{k|k-1})] + u_0^2. \quad (4-17)$$

Here,  $v_k$  and  $\tilde{x}_{k|k-1}$  are both random variables with  $E(v_k^2) = R$  and  $E(\tilde{x}_{k|k-1}^2) = P_{k|k-1} = P$ . Further,  $v_k$  is not correlated with  $\tilde{x}_{k|k-1}$ , so  $E(2v_k \tilde{x}_{k|k-1}) = 0$ . Therefore, the  $\hat{MSD}$  can be further simplified to:

$$\hat{MSD} = K^2(R + P) + u_0^2 = Q + u_0^2, \quad (4-18)$$

where the relation  $K^2(R + P) = Q$  can be obtained from Eqs. 4-8 and 4-12.

Analytically, the true MSD at the shortest time lag can be calculated based on the true positions state,  $x_k$ , and Eq. 4-1 in the main text:

$$MSD = E[(x_k - x_{k-1})^2] = E[(w_k + u_0)^2] = Q + u_0^2. \quad (4-19)$$

Therefore, the MSD calculated from a filtered trajectory using the correct values of  $Q$  and  $R$  in Eq. 4-18 is equal to the true MSD in Eq. 4-19.

### 4.3 Materials and Methods

#### 4.3.1 Application of the Kalman Filter to Simulated Trajectories

The trajectory of a labeled object undergoing linear motion (e.g., Brownian motion or active movement containing thermal fluctuation) can be simulated based on Eq. 4-1 and 4-4. The effective diffusivity and temporal resolution applied to the simulation were  $0.006 \mu\text{m}^2 / \text{sec}$  and  $0.033 \text{ sec}$ , respectively, which were extracted from particle tracking experiments of 100-nm microspheres in glycerol solution. From these conditions, the variance of a one-dimensional thermal fluctuation is represented by  $Q_T$  ( $= 2 \times 0.006 \times 0.033 \mu\text{m}^2$ ). For the simulation of Brownian motion the velocity of active movement is set to zero. In each simulation, a trajectory contains 1000 time steps; and extrinsic noise with variance,  $R_T$ , is further added to each step based on Eq. 4-2 and 4-3 to mimic the positioning error resulting from the imaging process.

The Kalman filter was then applied to these simulated noisy trajectories using several values of  $Q$  and  $R$  to understand the performance of the filter as the input variance terms differed from their true values (here,  $Q_T$  and  $R_T$ ). The accuracy of the filtered trajectory was evaluated by calculating the root mean square error of positions

(RMSE) (i.e.,  $\sqrt{(\hat{x}_{k|k} - x_k)^2}$ ).

### **4.3.2 Microscopic Particle Tracking System**

A Cascade:1K EMCCD camera (Roper Scientific, Tucson, AZ) mounted on a TE 2000-E inverted microscope (Nikon, Melville, NY) with a 60×, NA 1.45, oil-immersion objective lens (Nikon) was used to acquire particle-tracking video for image analysis. The particle tracking experiments were carried out by capturing video at a rate of 30 frames per second (fps). Each image sequence is composed of 650 frames. To achieve this high temporal resolution, the “region of interest” (ROI) function in the camera was activated and the binning was set at 3-by-3 for the particle tracking in glycerol (390 nm effective pixel size) and 2-by-2 for the gliding motility assay (260 nm effective pixel size).

### **4.3.3 Particle Tracking Experiments in Glycerol Solutions**

Carboxylated polystyrene fluorospheres (Invitrogen, Carlsbad, CA) with 100-nm diameter in water were diluted into glycerol at 1/1000 volume ratio. A drop of the mixture was placed on the central area of a glass bottom dish (MatTek, Ashland, MA) for video-based particle tracking experiments. The particle tracking method was described previously<sup>75</sup>. In brief, the background noise of the raw image stack was reduced using a Gaussian kernel filter<sup>76,77</sup>. Afterward, a 2-dimensional Gaussian distribution with logarithmic weighting was used to least-square fit the particles' intensity distribution in the region contains the pixel possessing the maximum intensity and its four adjacent pixels to determine the particles' positions.

### **4.3.4 Particle Tracking Experiments in Gliding Motility Assays**

Kinesin was prepared as previously described<sup>85</sup>. Microtubules were prepared by polymerizing 20 µg biotin-labeled tubulin (Cytoskeleton Inc., Denver, CO) in 6.5 µl growth solution, containing 4 mM MgCl<sub>2</sub>, 1 mM GTP and 5% (v/v) DMSO in BRB80

buffer (80 mM PIPES, pH 6.9, 1 mM MgCl<sub>2</sub>, 1 mM EGTA) for 30 min at 37 °C. The microtubules were 100-fold diluted and stabilized in 10 μM Paclitaxel (Sigma, Saint Louis, MO). The experiments were performed in ~100 μm high and 1 cm wide flow cells assembled from two coverslips and double-stick tape<sup>86</sup>. First, BRB80 with 0.5 mg/ml casein (Sigma) was injected into the flow cell. After 5 min, it was exchanged with a kinesin solution (BRB80 with 0.5 mg/ml casein, ~10 nM kinesin and 20 μM ATP). Five min later, this was exchanged against a motility solution (0.2 mg/ml casein, 20 mM D-glucose, 20 μg/ml glucose oxidase, 8 μg/ml catalase, 10 mM dithiothreitol and 20 μM ATP in BRB80) containing 0.8 μg/ml biotinylated microtubules. Five min were allowed for microtubule attachment after which 20 nM Alexa 568-labeled streptavidin (Invitrogen) in motility solution was perfused into the flow cell and incubated for 5 min to cover all the biotin sites on the microtubules<sup>87</sup>. Finally, after three washes with motility solution, biotin-labeled 40 nm fluorospheres (Invitrogen) at 100 pM concentration in motility solution were introduced into the flow cell and the edges of the flow cell were sealed with Apiezon grease to minimize evaporation.

#### 4.4 Results

To explore the application of the Kalman filter to effectively correct the influence of measurement noise on position estimation in single particle-tracking experiments, an error-free Brownian trajectory was simulated to serve as the reference trajectory (Fig. 4-2 A). Positioning errors with increasing variance values, denoted as  $R$ , were individually added to the reference trajectory to derive 4 noisy trajectories (Fig. 4-2 B; from the left to the right,  $R = 0.0004, 0.0011, 0.004$  and  $0.04$ , respectively). In these simulated trajectories, the input parameters, including the  $R$ -values, were chosen based on typical experimental conditions<sup>75</sup>. The Kalman filter was applied to these trajectories and the

root mean square errors (RMSE) of the positions between the estimated trajectories and the error-free trajectory were determined. The application of the Kalman filter requires two input parameters, the variance of thermal fluctuation ( $Q$ ) (from process noise) and the variance of positioning error ( $R$ ) (from measurement noise), which are not known *a priori*. First, identical values for  $Q$  and  $R$  are chosen to calculate the resulting RMSE values and to determine whether Kalman filtering could improve the noisy trajectories. The results show that the Kalman filter can reduce the positioning error even if the input parameters are arbitrarily assigned (Fig. 4-2 C). However, if the true values of  $Q$  and  $R$  are utilized (known for the simulation), the positioning error of the noisy trajectories can be further reduced up to  $\sim 3$  fold (Fig. 4-2 D).

The evaluation of the Kalman filter was further extended to trajectories describing active motion. Active motion trajectories without (Fig. 4-2 E) or with positioning error (Fig. 4-2 F; from the left to the right,  $R = 0.0004, 0.0011, 0.004$  and  $0.04$ , respectively) were simulated. Either arbitrary (Fig. 4-2 G) or accurate (Fig. 4-2 H) Kalman filter input parameters were applied to the noisy trajectories to estimate the true trajectories. Again, the positioning error generated during the acquisition process was reduced, and the optimal performance of the Kalman filter depended on the correct choice of input parameters.

These simulations suggest that the Kalman filter can effectively eliminate positioning error caused by measurement noise while retaining the intrinsic thermal fluctuations if the input parameters,  $Q$  and  $R$ , are available. However, the  $Q$  and  $R$  are two independent unknowns, whose values cannot be directly determined from an acquired image. Previously, a Monte Carlo method that utilizes empirical parameters

obtained from images is developed to extract the value of  $R$ <sup>75</sup>. This value of  $R$  is a positioning error that is individually estimated for each of our imaging experiments because  $R$  depends strongly on the incident light intensity and parameters of the acquisition system. The value of  $Q$  can be determined using the Eq. 4-5<sup>75,76</sup>. Since  $S$  can be obtained from experiments, the value of  $Q$  can be obtained as  $S - 2 \times R$  (Fig. 4-3; please also see Materials and Methods). A potential shortcoming of this method is that errors in the determination of  $R$  and  $S$  directly affect the accuracy of  $Q$ .

To assess the impact of inaccurate  $Q$ - and  $R$ -values in a model system, I tracked freely diffusing 100-nm diameter carboxylated polystyrene fluorescent particles in glycerol at room temperature and an acquisition frequency of 33 frames per second. These experiments were repeated many times and the value of  $R$  was estimated using the Monte Carlo procedure for each experiment<sup>75</sup>. Comparing the resulting microrheological measurement of the viscosity of glycerol with a conventional rheological measurement validated the accuracy of  $R$ . The standard deviation of  $R$  from 20 independent simulations is less than 3%, which is a further indication of the precision of this technique. Next,  $S$  was calculated as the mean square displacement (MSD) of the particles, and the value of  $Q$  for each experiment was obtained by using the relation,  $Q_i = S_i - 2 \times R_i$ , where the subscript  $i$  represents an independent tracking experiment. A plot of  $S$  and  $Q$  against the corresponding  $R$  shows that  $S$  and  $R$  are proportional to each other while  $Q$  remains constant through different values of  $R$  (Fig. 4-4 A). This calculated  $Q$ -value was also in agreement with the theoretically calculated thermal fluctuations at room temperature,  $Q_{RT} (= 0.8 \times 10^{-3} \mu\text{m}^2)$ <sup>75</sup>. We next determined the mean and the standard deviation of  $Q$  within fixed intervals of  $R$  (Fig. 4-4 B). Although  $Q$

and  $R$  are independent, the standard deviation of  $Q$  does increase with  $R$ . Since the experimental values of  $Q$  and  $R$  can be obtained, we can evaluate the performance of the Kalman filter on measured trajectories using the experimentally determined  $Q$  and  $R$ .

For the linear dynamic model, it is easily shown that the Kalman gain is determined only by the ratio of  $Q$  to  $R$ , and not the individual  $Q$ - and  $R$ -values (see Eq. 4-14). Thus, the performance of Kalman filtering is described by the plot of RMSE vs. normalized  $Q/R$  ( $= (Q/R)/(Q_T/R_T) = (Q/R)/(Q/R)_T$ ), where the  $Q_T$  and  $R_T$  represent the true variances of thermal fluctuation and positioning error in the acquired image, respectively (Fig. 4-4 C). As expected, the minimum RMSE value always occurs at normalized  $Q/R = 1$ , where the Kalman filter utilizes the accurate input ratio for the parameters,  $Q$  and  $R$ . Since the determination of the  $Q$ -value using the procedure described above has some uncertainty (green region: one standard deviation around mean of  $Q$ ; red region: two standard deviations around the mean), the RMSE values obtained using the experimentally determined  $Q/R$  tend to be slightly larger than the optimum. These RMSE values can be compared to the RMSE value at very large normalized  $Q/R$  (e.g.  $10^4$ ). In this region, the Kalman filter assumes minimal measurement noise and places a much greater reliance on the measurements by making minimal changes to the measured trajectory. Therefore, the RMSE values at very large normalized  $Q/R$  are representative of the unfiltered RMSE values. A comparison shows that the experimentally obtained  $R$ - and  $Q$ - values lead the Kalman filter to estimate more accurate trajectories with smaller RMSE values when compared to the RMSE values of the original trajectory.

Based on the experimental data, the percentage of RMSE improvement after applying the Kalman filter can be quantified (Fig. 4-4 D). Using the mean value of  $R$  in each  $R$ -interval and the corresponding  $Q$  at the mean  $\pm$  one standard deviation as the input parameters of the Kalman filter, the RMSE of the filtered trajectories can be calculated and compared to the minimal RMSE value obtained for  $Q/R$  equal to  $(Q/R)_T$ . The data ( $\blacklozenge$ : left and  $\blacklozenge$ : right bound in Fig. 4 C) suggests that within the standard deviation (68.2%) of the  $Q$ -value, the Kalman filter achieves at least 82% of the maximal reduction in RMSE value. First considering that an accurate estimate of  $R$  can be obtained in the experiment using the Monte Carlo simulation technique, secondly that the estimate of  $Q/R$  determined in real experiments has a limited range (e.g., normalized  $Q/R$  values vary from  $\sim 0.79$  to  $1.16$  and  $\sim 0.63$  to  $2.3$  for  $R \sim 6 \times 10^{-4}$  and  $3.4 \times 10^{-3} \mu\text{m}^2$ , respectively, in Fig. 4 B), and finally that the filtered RMSE value for input parameters,  $Q$  and  $R$ , in this limited range is very close to the minimum RMSE value obtained for the optimal  $Q/R$ . It concludes that the application of the Kalman filter as described can reliably reduce the positioning error generated in the image acquisition process.

To demonstrate the application of the Kalman filter to experimental data of a purely diffusive process, particle tracking of 100-nm carboxylated polystyrene fluorescent microspheres in glycerol was performed and the MSD profiles were calculated from the tracking trajectories (see Fig 4-5). New MSD profiles calculated from the Kalman filtered trajectories of the microspheres demonstrated the successful removal of extrinsic noise by the Kalman filter.

We further applied the Kalman filter to an active transport process by estimating a more accurate trajectory of beads attached to a microtubule gliding on surface-adhered kinesin-1 motors (Fig. 4-6 A). These position data and the extracted parameters,  $R$  and  $Q$ , from the images were used as input for the Kalman filter, and the estimated trajectory for the microtubule was obtained (Fig. 4-6 B). The average distance covered as a function of the time between frames (Fig. 4-6 C) and the variance of the fluctuations around this average distance as a function of the time lag (Fig. 4-6 D) show the expected linear behavior<sup>82, 88, 89</sup> for the filtered trajectory, while system noise distorts the unfiltered quantities. If the microtubules were stationary objects, the position variance of the attached beads would not display this linear increase. However, the active movement of the microtubules during the gliding motility assays will directly affect the observed position of the attached beads. In essence, the gliding motion is thought to consist of a movement with constant velocity (caused by the active transport by the surface-adhered motors) superimposed with a diffusive movement against a high drag caused by “protein friction” (motor binding events which do not contribute a forward force). Thus, it is the diffusive movement of the microtubules and not of the attached beads that causes the linearly increasing positional variance of the beads. Previous studies of gliding cytoskeletal filaments, such as actin filaments and microtubules, have also interpreted the increasing positional variance as a result of protein friction<sup>82, 90-95</sup>.

The glycerol and *in vitro* gliding motility studies show that the Kalman filter can restore particle trajectories from diffusive as well as active transport, providing a more accurate picture of the underlying dynamics. To further verify the results from the motility studies, an independent method to correct for trajectory error was performed

and compared to the Kalman filtered MSD values and the raw data. The MSD profiles from the two different methods shared an approximate 5-fold decrease in MSD value from the raw data and were in good agreement when directly overlaid (Fig. 4-6 E). Another way to verify the success of Kalman filtering is to analyze the autocorrelation function (ACF) of the innovation residual of the Kalman filter ( $z_k - \hat{x}_k$ ; observed position - predicted position). Theoretically, the innovation residue should be Gaussian white noise; hence, the signature of its ACF will be independent of time lag, which is demonstrated by a value of unity at 0 and a value of 0 for all other time lag (Fig. 4-6 F)<sup>96</sup>. Through these separate analyses of the Kalman filtering of the gliding motility assay, which are independent of the stochastic model used, I can solidly conclude that the Kalman filter can be successfully applied to this *in vitro* system.

#### 4.6 Discussion

The application of the Kalman filter to biological systems will encounter several challenges that must be overcome. Subcellular dynamics are often complicated and effective models that can faithfully describe them are usually unavailable. Many factors such as the thermal fluctuations, the steric effects from heterogeneous cellular architecture and the dynamics of the cytoskeleton reorganization contribute to the complexity of the dynamic movement of a micron- or submicron-scaled tracer inside a living cell. Therefore, the first step to using a Kalman filter for this type of approach is to determine the appropriate stochastic model describing the motion of a subcellular object. Such a model would highly depend on several factors such as diffusivity, cell cycle stage, microenvironmental conditions and composition. If the model justifies the application of a linear filter, the Kalman filter can be applied using the same

methodology as the *in vitro* systems discussed in this work. With the correct stochastic model in place, the Kalman filter could become a powerful tool to reduce measurement noise and reveal the real-time dynamic interactions between a particle and its microenvironment.

Another challenge facing the application of the Kalman filter to intracellular dynamics is the presence of photobleaching effects or big movements out of the focal plane in particle tracking experiments. For typical particles like quantum dots and 100-nm diameter fluorescence microspheres, which possess  $Q/R$  values within the range studied here, the variance of the positioning error ( $R$ ) is assumed to be unchanged during the observation period in these *in vitro* studies. However, these conditions may not be fulfilled when studying the dynamics of a single molecule in living cells at 30 fps due to the large mobility of the probing molecule. The reported diffusivity of GFP in cytoplasm is  $20 \mu\text{m}^2/\text{s}$  and the focal depth  $\sim 1 \mu\text{m}$ . Thus, the time required for the GFP to diffuse out of the focal plane is  $\sim 0.05 \text{ s}$  ( $\sim L^2/D$ ). In that case, the  $R$ -value would be a function of the molecular position in the  $z$ -direction and change dramatically if the temporal resolution is not correspondingly higher than 30 fps. Photobleaching effects would also change the  $R$ -value because the decreasing intensity causes a gradual increase in positioning error. As the temporal resolution is increased to offset movements out of the focal plane, the acquired images would be correspondingly dimmer unless the light source intensity was increased, which would further aggravate photobleaching problems.

This trade-off between temporal and spatial resolution has limited the ability to further explore the cellular dynamic process of subcellular components and intracellular

microrheology<sup>38, 42, 43, 64, 97</sup>. Video-based microscopy studies have provided a qualitative understanding of this issue<sup>98</sup>, but an optimal balance of temporal and spatial resolution has not yet been fully developed. Recent developments in photon detection techniques allow us to track object movement with high temporal resolution<sup>99</sup>, which would help to compensate for movements out of the focal plane. As these types of techniques develop and a more comprehensive knowledge of spatio-temporal resolution emerges, problems associated with photobleaching effects and movements out of the focal plane can be overcome. High temporal resolution could then be utilized in a particle tracking experiment at the expense of some degree of spatial resolution that could later be restored analytically by proper use of the Kalman filter, increasing the capacity to identify and quantitatively characterize subtle intracellular motion.

I characterized the performance of the Kalman filter in estimating the native trajectory of particles diffusing within a glycerol solution and the transport process of microtubules *in vitro*. I demonstrate that the Kalman filter is an effective tool to eliminate positioning error incorporated into the real trajectory during image acquisition while preserving the inherent thermal fluctuations, and that the success of the Kalman filter depends on the correct setting for the parameter describing  $Q/R$ . Kalman filtering can preserve the native fluctuations while removing the measurement noise; hence it greatly enhances the reliability of an estimated trajectory.

I have shown that the value of  $R$  in a particle tracking experiment can be extracted using a Monte Carlo simulation technique<sup>75</sup>. The extracted value of  $R$  is highly reproducible and successfully corrects the static error of noisy MSD curves. Furthermore, by using the values of  $Q$  and  $R$  extracted from experiments, the individual

trajectory resulting from the Kalman filter is optimized. The reliability of Kalman filter in predicting the trajectory can be assessed by the RMSE computation, which is compared to a simulated, true trajectory. The trajectory estimation from the Kalman filter using the extracted values of  $Q$  and  $R$  can lead to a significant reduction of the RMSE value, close to the minimal value achievable with exact knowledge of  $Q$  and  $R$ . At this minimum, the estimated trajectory carries a MSD equal to the MSD obtained from the true trajectory which can be proved mathematically as well (see section 4.2). Therefore, it is concluded that Kalman filter can effectively improve the video-based particle-tracking trajectory in the *in vitro* systems examined.

#### **4.7 Conclusion**

In summary, the purpose of this study is to take a first step and introduce the application of the Kalman filter to biology and biophysics. The Kalman filter has evolved since its initial development into an extremely powerful tool used in many applications, even in the analysis of the stock market<sup>44</sup>. This work suggests that the Kalman filtering approach can be utilized for the investigation of the *in vitro* systems studied here and *in vivo* systems in the future under careful consideration of its limitations.

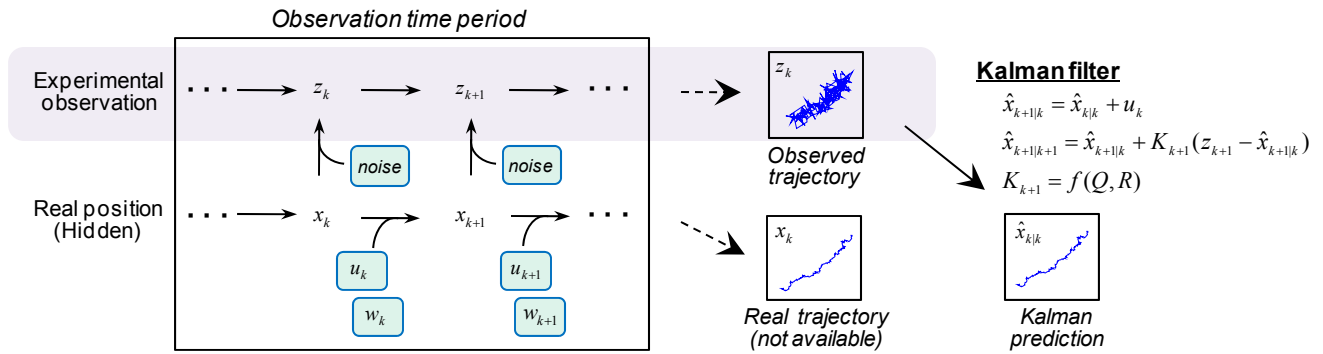


Figure 4-1. Schematic illustration of the principle of Kalman filter in estimating the accurate trajectory in a cellular dynamic process. The relation between adjacent steps of a trajectory is  $x_{k+1} = x_k + u_k + w_k$ , where the occurring displacements before the next monitored time for the particle in  $x_k$  position are determined by its projective movement displacement,  $u_k$ , and a random movement generated by thermal fluctuation,  $w_k$ . Here, the subscript  $k$  represents the  $k$ -th step of the tracking trajectory. In tracking experiments, the real particle position,  $x_{k+1}$ , is recorded as  $z_{k+1}$  due to the positioning error. The Kalman filter is an established algorithm to restore the correct trajectory for a linear process.

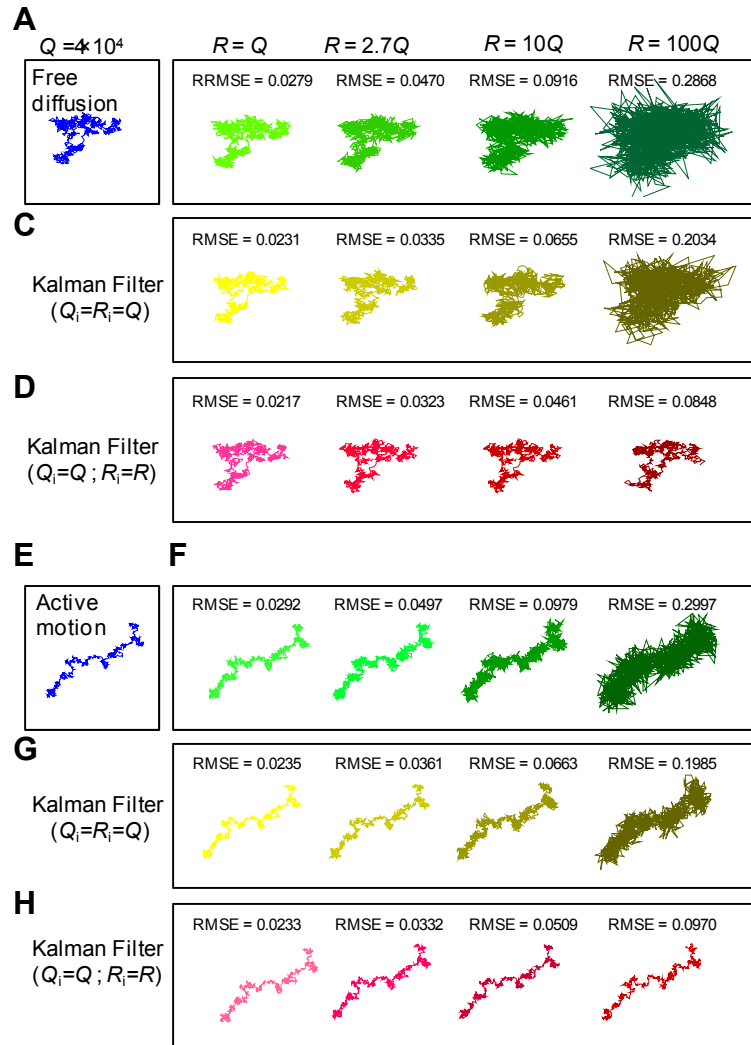


Figure 4-2. Estimation of the true trajectory from positioning errors using Kalman filter (A) A simulated Brownian motion trajectory is represented without positioning error. (B) Increasing degrees (from left to right) of positioning error (quantified by its variance  $R$ ) are added to the simulated trajectory. Higher  $R$ -values yield noisier trajectories. (C) The Kalman filter removes some extrinsic noise under an arbitrary setting of the input parameters  $R_i$  and  $Q_i$ , e.g.  $Q_i = R_i = Q$  where  $Q$  is the thermal fluctuation variance. (D) The Kalman filter restores the noisy trajectories if the correct  $Q$ - and  $R$ -value are used as input parameters  $Q_i$  and  $R_i$ . (E) A simulated active motion trajectory is represented without positioning error. (F) Increasing degrees of positioning error are added to the active motion trajectory. (G) The Kalman filter improves the noisy trajectories under the setting  $Q = R$ . (H) The Kalman filter restores the noisy trajectories under the correct  $Q$  and  $R$  setting.

**Implementing Kalman filter to obtain the resolution beyond optical limitation**

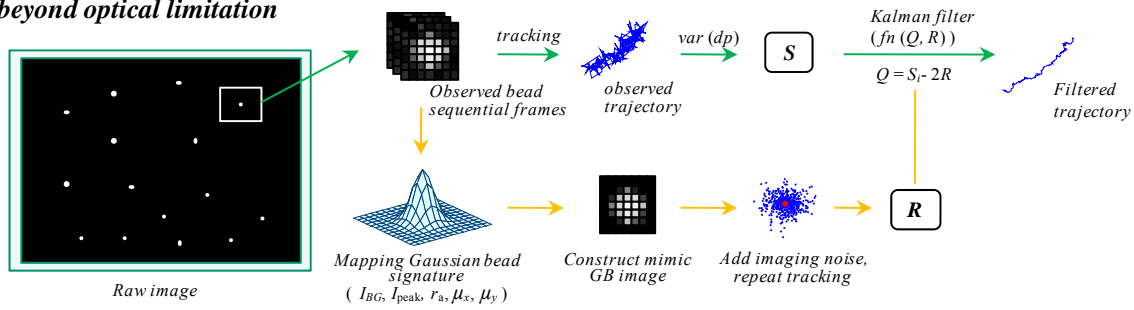


Figure 4-3. Schematic illustration of the procedure of implementing Kalman filter into a microscopic particle tracking system to improve the spatial resolution. The acquired images are used to extract the parameters to simulate Gaussian particle, which is applied to the particle-tracking algorithm to determine the variance of positioning error ( $R$ ). The  $R$ -value and corresponding  $Q$ -value, determined by the MSD of the tracking trajectory and  $R$ -value, then be used as the input parameters for Kalman filter to restore the true trajectory.

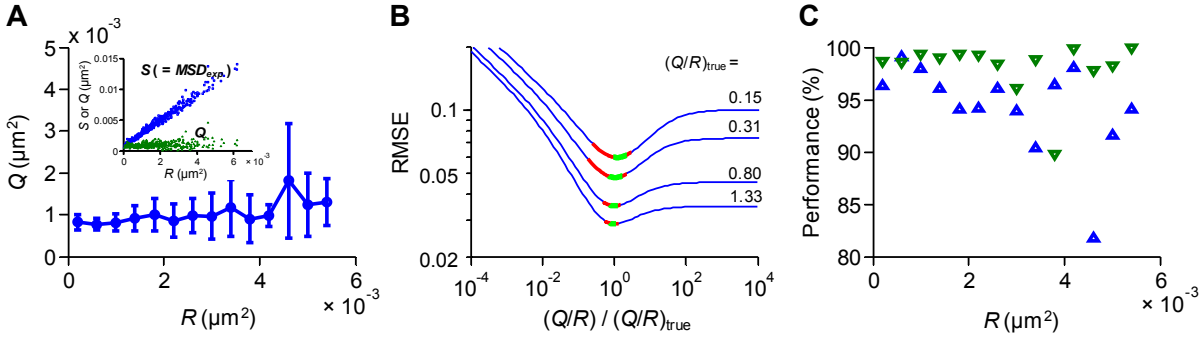


Figure 4-4. Characterization of the performance of Kalman filter on estimating particle tracking trajectories (A) The variance of thermal fluctuation ( $Q$ ) can be extracted from the variance of displacement ( $S$ ) and the variance of positioning error ( $R$ ) using the relationship,  $Q = S - 2 \times R$ . The mean of  $Q$  is estimated for different intervals of  $R$ , with an interval size of  $0.4 \times 10^{-3} \mu\text{m}^2$ . The error bar represents the standard deviation of  $Q$ . The resolution of  $Q$  decreases with increasing of  $R$ . *Inset*: The trajectories contain 504 data points from particle tracking in glycerol described in the methods section. (B) Kalman filter performance is determined by the accurate  $Q/R$  value. Using the experimental  $R$ -values and their corresponding ranges of  $Q$ -value in simulations, the root mean square error (RMSE) of the Kalman filter-estimating trajectories, compared to the simulated true trajectory, can be obtained. The green and red region represents the RMSE value for  $Q$ -value within one (green) or two (red) standard deviations of the mean. (C) The performance of the Kalman filter in estimating the true trajectory measured by the RMSE reduction relative to the maximal RMSE reduction achieved for  $Q/R = (Q/R)_T$ . At the minimal RMSE value, the estimating trajectory carries a MSD value equal to the true trajectory (see supporting material). The filtered trajectory is identical to the unfiltered trajectory if there is no positioning error ( $R = 0$ ) or if no improvement has been achieved which occurs in for very large normalized  $Q/R$ . Thus, the RMSE value at large  $Q/R$  represents the original RMSE value of the tracked trajectory. The maximum improvement of the RMSE value thus is equal to the difference between the RMSE value at large  $Q/R$  and the minimal RMSE value in the RMSE- $Q/R$  curve.

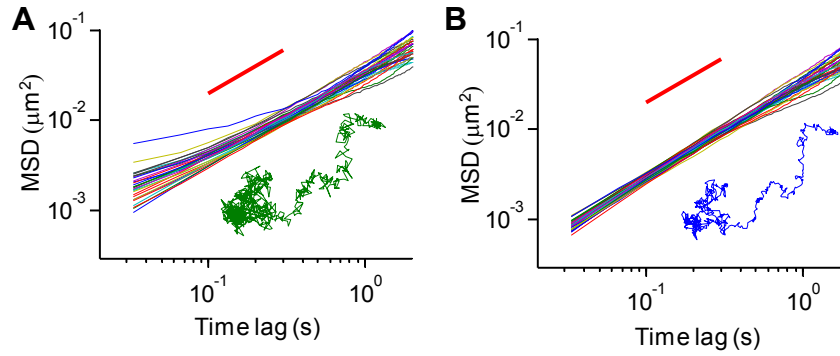


Figure 4-5. Improving the positioning error of particle tracking in glycerol solution (A) The MSD curves were obtained by particle tracking of 100-nm carboxylated polystyrene fluorescent microspheres in glycerol, 31 microspheres were tracked. (B) The MSD curves were calculated from the filtered trajectories. *Insets* in (A) and (B) represent one of the trajectories before and after application of the Kalman filter, respectively. Results from tracking a 20-nm biotinylated nanosphere attached to a microtubule in a gliding motility assay at 30 fps.

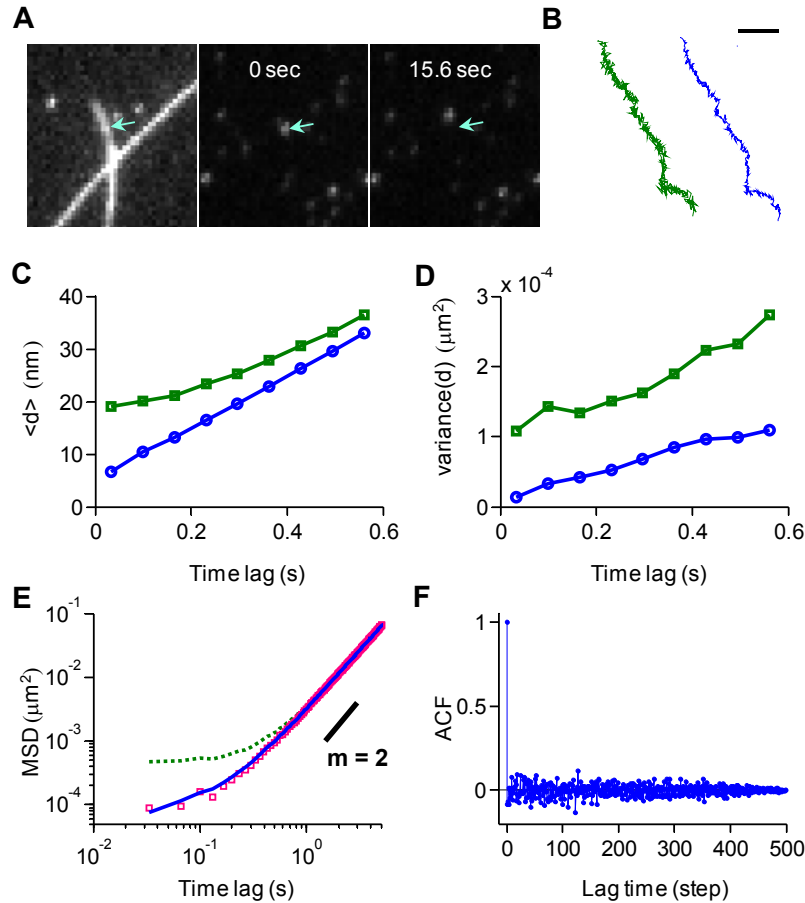


Figure 4-6. Improving the positioning error of particle tracking in gliding motility assays using Kalman filter (A) Images of a gliding motility assay. Images from left to right represent the microtubule, the nanosphere at 0 sec and the nanosphere at time 15.6 sec, respectively. The arrow indicates the initial position of the nanosphere, which is moving with a microtubule. (B) Observed trajectory (left) and filtered trajectory (right) of this nanosphere during the observation time period (15.6 sec). Scale bar: 200 nm. (C) Average of nanosphere displacement as a function of time interval. Removal of noise reduces the displacement at small time intervals of the filtered trajectory (○) relative to the raw trajectory (□), as expected for movement with constant velocity. (D) Variance of nanosphere displacement as a function of time interval for the filtered (○) and raw (□) trajectory. Removal of measurement noise yields the expected linear function starting at the origin and enables a correct estimate of the motional diffusion coefficient. (E) MSD from the different particle trajectories for different time lag is plotted. The value of the observed MSD (dashed line) is roughly 5 fold higher in comparison to MSD values with static error removed (solid line) and MSD values calculated from the Kalman filtered trajectory (□). (F) The innovation residual of the Kalman filter ( $z_k - \hat{x}_k$  or the difference between observed and predicted positions) is theoretically Gaussian white noise. The autocorrelation function (ACF) of innovation residual is plotted against different time lag. Accordingly, the ACF is independent of lag time, which is a feature of Gaussian white noise.

## CHAPTER 5 CHARACTERIZATION OF THE NAC-1 NUCLEAR BODY DYNAMICS AND CHROMATIN ASSOCIATION

### 5.1 Background

In this chapter, the methods described in the prior chapters are further used to study intra-nuclear dynamics. The cell nucleus plays a central role in mediating cell function through gene regulation. Thanks to the completion of the human genome project, the full sequence of the human genome has been unveiled<sup>47</sup>. However, it remains unclear how highly dynamic cell physiology can be governed strictly by gene regulation<sup>50, 56</sup>. Variation of gene expression profiles in different types of cells and diseases suggests that a complicated system should exist in the nucleus to regulate the genome function<sup>100, 101</sup>, and that dynamic changes in nuclear organization and architecture may play a key role in gene expression<sup>48</sup>.

The evolution of a cancer cell involves a complicated, multi-step process containing many unidentified factors that may alter gene expression<sup>101, 102</sup>. The detailed mechanism of gene regulation remains unknown; nevertheless, the alteration of nuclear architecture has been observed in the progression of cancer cells<sup>59, 101</sup>. Hence, the changes in nuclear architecture might determine the gene accessibility of transcription factors<sup>52</sup> as a means to mediate gene transcription and promote cancer development. Presently, ovarian cancer is one of the most lethal gynecological malignant diseases in the United States. In the tumorigenesis of ovarian cancer, the nucleus accumbens-1 (NAC-1) protein has been recently identified as one of the up-regulated genes<sup>103</sup>. NAC-1 is located in the nucleus and it forms homodimers via the BTB/POZ domain, which is reported to be an essential process for tumor cell growth<sup>104</sup>. The over-expression of NAC-1 is tightly associated with the development of chemoresistance in ovarian cancer

cells<sup>105, 106</sup>. Interestingly, high expression level of NAC-1 causes the formation of distinct, dense body-like structures in the nucleus<sup>104</sup>. Aside from chromatin, the nucleus possesses many other organelles such as nucleoli, nuclear speckles, Cajal bodies and PML bodies<sup>50, 53</sup>. These known nuclear bodies are believed to be associated with gene regulation that governs important cell functions<sup>49, 55, 107</sup>. For instance, Cajal bodies are associated with RNA synthesis and RNP assembly<sup>49</sup>. Thus, it is probable that the newly discovered NAC-1 NB is also involved with the genome regulation in the nucleus.

Recently, two downstream transcriptional targets of NAC-1 have been identified: Gadd45-gamma-interacting protein 1 (Gadd45gip1) and Gadd45-gamma. They are each associated with the Gadd45 pathway and their expression is down-regulated by NAC-1<sup>106</sup>. When a dominant-negative form of the NAC-1 protein containing only the BTB/POZ domain is introduced into cells, the nuclear body is disrupted and the expression of both Gadd45gip1 and Gadd45-gamma increases. This indicates that the intact structure of NAC-1 NB is involved in the regulation of transcription as well. Yet, the detailed mechanism of NAC-1 NB-controlled gene transcription regulation is still unknown.

This knowledge about the nuclear body is mainly available through the characterization of its components at the protein level<sup>50</sup>. However, the real time interactions of the intact nuclear body with chromatin are not well understood. For example, it is known in detail that the PML NB is disrupted in acute promyelocytic leukemia (APL) -blasts as a consequence of the dominant-negative action of the PML-RAR $\alpha$  fusion protein over PML NB through direct physical interactions. The oncogenic PML-RAR $\alpha$  protein, which induces APL, is generated by the fusion of the gene encoding

PML protein and the gene encoding retinoic acid receptor  $\alpha$ . When the PML NB is able to be reformed, resulting from treatment with retinoic acid, the aberrant phenotype can be reversed<sup>108</sup>. However, the true function of the PML NB in the nucleus still remains as an open question. In this study, the short time dynamics of NAC-1 NB is examined by directly tracking the NAC-1 NB movement to characterize their interaction with chromatin.

While examining the short time dynamics of NB, the limited photon integrating time is important to consider. An adequate spatial resolution remains necessary to avoid tracking with great amount of error that could bias measurements and lead to misinterpretation of the results. Through careful application of the method described in the prior chapters, trustworthy NB dynamics can be acquired. In this work, confocal microscopy is used to examine the structure of NAC-1 NB and its location in the nucleus. The movement of NB is measured for characterizing their mobility at short time scales. Finally, drug treatments are applied to examine the change in NAC-1NB dynamics in response to different cellular perturbations, including transcription inhibition, ATP reduction, and cytoskeleton disruption.

## **5.2 Methods and Results**

### **5.2.1 Characterization of NAC-1 NB in nucleus**

Since NAC-1 NB was a newly discovered nuclear structure, we first studied the nuclear location of NAC-1 NB. RK-3E cells stably expressing the GFP-NAC-1 were stained by propidium iodide (PI; Sigma, St. Louis, MO) to label the chromatin region. Confocal microscopy (EZ-C1, Nikon, Melville, NY) was used to acquire images using 30  $\mu\text{m}$  pinhole to achieve better localization of NAC-1 NB in the chromatin cluster. The

images from the stained-nuclei show that the NAC-1 NB is spatially excluded from the DNA dense regions (Fig. 5-1). This result indicates that NAC-1 NBs are located in the interchromatin compartments, where most nucleus organelles, including PML and Cajal bodies, are located. However, unlike PML proteins that form a ring-like structure in the PML body, the NAC-1 proteins have a more homogeneous distribution in NAC-1 NB <sup>107</sup>.

Through observing the cell in interphase, it is found that NAC-1 NBs possess different sizes. This result was supported by previous electron microscopy study, which showed that the size of NAC-1 was distributed in the range of 0.2 -1.8  $\mu\text{m}$  <sup>104</sup>. A sequential observation for a 24-hour period on the same batch of cells further revealed that the size of the NAC-1 NBs correspondently grows with the progression of cell cycle until mitosis, in which the NBs dissolve (data not shown).

The kinetics of the NAC-1 NB was assessed by fluorescence recovery after bleaching (FRAP). The pinhole size of the confocal module was set to the maximum (150  $\mu\text{m}$ ) to minimize the out-of-focus effect from the z-direction movement of NB. The bleaching of the NAC-1 NB was operated on a region of interest (ROI) with 1  $\mu\text{m}$   $\times$  1  $\mu\text{m}$  squared size to document the recovery of intensity. The intensity of the ROI at different onset time after the photobleaching (denoted as  $I_{ROI}$ ) was further normalized (denoted as  $I'$ ) by the intensity prior to and right after photobleaching (denoted as  $I_{prior}$  and  $I_{bleach}$  respectively) as:

$$I' = (I_{ROI} - I_{bleach}) / (I_{prior} - I_{bleach}) . \quad (5-1)$$

FRAP analysis showed that the recovery of NAC-1 NB intensity reaches ~50% after few minutes (Fig. 5-2). This recovery rate was similar to both PML and Cajal bodies, suggesting that NAC-1 NBs possess a similar assembly kinetics as PML and

Cajal bodies<sup>107</sup>. In addition, NAC-1 NBs presumably possessed a stable core structure, judging from the 50% of immobile fraction that won't be replaced by fluorescent form of NAC-1 after Photobleaching.

### 5.2.2 Typical Motion of NAC-1 NB in Nucleus

The dynamics of NAC-1 NB were studied by single particle tracking method with the experimental setup described in section 4.3.2. To minimize the effect of dynamic error, the exposure time was reduced to 6 ms. The static error ( $\epsilon_s$ ) of each measured MSD was estimated using method described in chapter 2. Further, to exclude the unreliable data, in which the resolution is insufficient to estimate static error, a threshold for the signal-to-noise ratio (SNR) was chosen to be 0.2. The SNR was determined by following equation,

$$\sqrt{(MSD_{\text{exp}} - \epsilon_s) / \epsilon_s} \quad (5-2)$$

This threshold value was selected based on the minimum resolution that the static error can still be successfully estimated.

The MSD values of the tracked NAC-1 NBs obtained from only x- or y-direction were similar, suggesting that NAC-1 NBs have isotropic motion in x-y plane. Therefore, the 2-dimensional MSD profiles in x-y plane were analyzed in different time lags from 168 NAC-1 NBs in 21 cells and plotted in the logarithmic scale in Fig. 5-3A. The results showed NAC-1 NB undergoes a sub-diffusive motion in short time intervals (time lag ( $\tau$ ) < 0.3s), where the sub-diffusive motion coefficient ( $\alpha \equiv d(\text{MSD})/d\tau$ ) is less than 0.6. The motion became more free diffusive ( $\alpha = 1$ ) if the probing time lag increased. The distribution of the motion coefficient at three different time lag intervals, 0.1s – 0.3s, 0.3-1s and 1s-5s, showed an average coefficient of 0.5, 0.58 and 0.96, respectively (Fig. 5-

3B). At large time lag ( $\tau > 5s$ ), some MSDs show the trend of directed motion (which has the signature,  $\alpha > 1$ ). The arrows, indicating the displacement at large time lag ( $\tau = 5s$ ), implied that the NBs have consistently synchronized movements in a nucleus (Fig. 5-4). Together, this result suggested the active movement, indicating by the motion coefficient derived from the MSD data for a long time lag that it was from convective nucleus movement. Taken together, from the MSD analysis, it suggested that the movement of NAC-1 NBs was dominated by random forces in short time, and the active motion of the bulk nucleus has significantly influenced the random motion of NAC-1 NBs in the longer time period.

To further identify whether the magnitude of the bulk nucleus active motion affects the short time measurement, the correlated coefficient ( $\rho_{ij} \equiv 2 \langle dx_i \times dx_j \rangle / (\langle dx_i^2 \rangle + \langle dx_j^2 \rangle)$ ), where  $dx_i$  and  $dx_j$  represent the displacements from distinct nuclear bodies, was applied to analyze a couple of nuclear bodies in a nucleus. When  $\rho_{ij}$  approximated a value of 1, it represented perfect synchronized movement, possibly as a result of the nucleus bulk movement. On the other hand when  $\rho_{ij} \sim 0$ , it represented that the displacements from two different objects are uncorrelated motions in the nucleus.

From this analysis, the result suggested the NB movements are not significantly correlated ( $\rho_{ij} < 0.2$ ) at shorter time scale ( $\tau < 1s$ ). However, the correlated coefficient between different displacements increased to 0.6 when time lag was over 10 sec. This further supported the previous conclusion from the MSD analysis that NAC-1 NB has more directed mobility via the motion of the nucleus. On the other hand, the contribution of the nucleus convective movement was limited for the NBs at a shorter time frame and

the NAC-1 NB movement was mainly dominated by its interaction with the surrounding chromatin.

The size distribution of the NAC-1 NB in the nucleus had been addressed in section 5.2.1. Here, I further examined the role of size on NB mobility. The relative size of NBs was estimated from a sequential z-stack of fluorescent images, captured right after particle tracking of the same NBs. In general, an image in which the object of interest has the brightest intensity in a stack of sequential z-dimensional scan was the image taken closest to the focal plane. Thus, an image having the brightest NB of interest in the sequential Z-dimensional scan was chosen to measure the size of the specific NB by a 2-D Gaussian fit (Eq. 3-1). Even though sizes determined by this method could not represent the true size of individual NBs, the size of an NB estimated from this method was used to establish the relative difference in size when compared to other NBs. Cross-comparing the estimated size of NB by this method with the 3D image from confocal microscopy further supports the eligibility of this method (Fig. 5-5). During the required time period, which is ~20 sec, to scan and acquire sequential images in the z-direction, the distance an NAC-1 NB can move was less than 300nm. Hence, the position of a NB being monitored in tracking experiment can directly correspond to the z sequential images and the relative size of the NB can be assessed.

From the above measurements, the scatter plot of the NB size vs. MSD value at a lag time of 0.1 sec indicated that these two variables are negatively correlated with a correlation coefficient ( $\gamma$ ) equal to -0.6 (Fig. 5-6A). A similar analysis also suggested that the MSD slope negatively correlates with the MSD value at a lag time of 0.1 sec ( $\gamma = -0.5$ ) (Fig. 5-6B). In other words, NAC-1 NBs with a larger size usually possessed

smaller MSDs and lesser sub-diffusive effects in the short time lag. This correlation was not found in long time lag presumably because their motion is dominated by the bulk nucleus convective motion. The correlation between a NBs' mobility and its location was also examined and no significant direction-dependence was found on the monitored plane (data no shown). This result suggested that the NAC-1 NBs in a nucleus are enclosed by a uniform architecture within the interchromatin region.

### **5.2.3 NAC-1 NB Dynamics Relates to the Chromatin Architecture and ATP Level**

It is known that the ATP is required to maintain the chromatin structure, and in ATP deficient cells, the chromatin is condensed and less dynamic<sup>5</sup>. Thus I further studied the dynamics of NAC-1 NB in the nucleus with the depletion of ATP. The ATP level in a cell was reduced by the addition of the cellular respiration inhibitor, sodium azide (10mM), alone with the glycolysis inhibitor, 2-deoxy glucose (6mM) for 1hr. The morphology of NAC-1 NB did not significantly alter after drug treatment. However, the values of the effective diffusivity ( $D_{\text{eff}} \equiv \text{MSD}/4\tau$ ) of NAC-1 NB at 0.1s time lag increased ~3.5 times (Fig. 5-7A). However, the ATP depletion did not change the sub-diffusive state of NAC-1 NB. This result suggested that the association between NAC-1 NB and chromatin, which potentially causes the sub-diffusive effect, is not ATP-dependent.

Furthermore, when cells were treated with 1ug/ml Actinomycin D (ActD), which binds to DNA by intercalation<sup>109</sup>, it had the opposite effect on the  $D_{\text{eff}}$  of the NAC-1 NB, which reduced ~ 2 fold 30mins after the treatment (Fig. 5-7A). After 1hr, only less than 5% of NBs had a movement amplitude that was above the detection limitation (<5nm). This suggested the chromatin structure surrounding the NAC-1 NB was responsive to the ActD. Since ActD is known as a transcription inhibitor that can bind to the active sites of chromatin to prevent the elongation of mRNA, it was reasonable to assume that

the mechanical properties of the DNA string were enhanced by the intercalation effect of ActD. The mechanical changes of chromatin could contribute to the loss of the mobility of NAC-1 NB after treatment. Moreover, this result could also lead to the hypothesis that the NAC-1 NBs are located in a gene rich region. Unlike ActD, another DNA binding molecule Hoechst 33342 (1mg/ml) that binds to the DNA A-T grooves had little effect on the mobility of NAC-1 after 1hr incubation (Fig. 5-7B). Hence, this result indicated that either the A-T groove binding dye had little effect on the chromatin mechanics and dynamics, or the effect will not change the mobility of NAC-1 NB.

Whether the intact cytoskeleton structure could affect the dynamics of NAC-1 was also studied. Microtubule (MT) and actin were disrupted by nocodazole (NOC) (1 $\mu$ M, 30min) and latrunculin B (LatB) (100nM, 30min), respectively. MT Disruption did not alter the  $D_{\text{eff}}$  of NAC-1 NB. However, the latrunculin B treatment resulted in actin depolymerization and gave rise to a rounded cell shape. As a result, the  $D_{\text{eff}}$  value of NAC-1 NB in short time lag ( $\tau = 0.1$  s) increased  $\sim 2$  times (Fig. 5-7B). This result suggested that the integrity of actin cytoskeleton can affect the NAC-1 NB dynamics directly or through the dynamics of chromatin. Since it is known that the actin cytoskeleton physically links to nucleus to maintain the nucleus integrity, disruption of the actin cytoskeleton could potentially affect the stability of the nuclear structure as suggested by the increase of NAC-1 NB mobility after actin disruption. Another possible mechanism for the LatB treatment to affect the NAC-1 NB motion was through the disruption of nuclear actin, which potentially has a role in maintaining the nucleoskeleton or mediating intranuclear transcription.

The NAC-1 NBs' motion coefficient,  $a$ , at short time lag (0.1 - 0.3s) was also measured before and after different drug treatments (Fig. 5-7C). The ActD and LatB treatments were found to significantly increase sub-diffusivity and the motion coefficient dropped ~50% and ~60%, respectively, after the treatment. Yet, these two drugs possessed opposite effects on the mobility of NAC-1 NB. This result suggested that ActD and LatB treatments affect the chromatin-NAC-1 NB interaction through different mechanisms. Hypothetically, ActD treatment could stiffen the chromatin that is associated with NAC-1. Hence, the NAC-1 NB motion was well confined in the stiffer chromatin environment, which lowers the motion coefficient to a more sub-diffusive state. In contrast, LatB treatment increased the mobility of the NAC-1 NB (as the values of MSD increased) but decrease the motion coefficient. The possible explanation for this phenomenon was that the chromatin-NAC-1 NB interaction was reduced through nucleoskeleton disruption. The other possibility was that the disruption of the actin cytoskeleton increases the diffusivity of the whole nucleus, which also makes the mobility of all the NBs increase. Yet, the rounded nucleus could decrease the space of interchromatin in the x-y plane and cause the NAC-1 NB to quickly reach a diffusion barrier (or corral) within the observing time lag.

The changes of diffusion patterns of NAC-1 NB over time in response to drug treatments were characterized from their relation between MSD and lag time (Fig. 5-8). In a normal untreated cell, the NAC-1 NB showed a subdiffusive behavior in short time lag ( $a \sim 0.5$ ) and gradually became diffusive and eventually had directed movement as mentioned in previous section. After ATP depletion, the motion of NAC-1 NBs was subdiffusive regardless of the time lag range (from 33ms to 10s) (Fig. 5-8A). This

indicated that the directed movement of the nucleus is no longer dominant in the long time lag, considering the  $\sim 0.5$  sub-diffusive coefficient at larger time lag and the less synchronized NB movement in 10s (Fig. 5-8A, *inset*). This further suggested that the directional movement of the nucleus requires ATP.

In ActD treated cells, NAC-1 NBs showed a strong sub-diffusive response ( $\alpha < 0.25$ ) over short time lag ( $\tau < 0.2$  s) and dramatically progressed to directed motion (Fig. 5-8B). Hence, after 0.2 sec the MSD is dominated by the directed movement from bulk nucleus with higher magnitude comparing the state before treatment. The 10 sec displacements of NAC-1 NBs showed the augmented degree of directional motion, which was consistent with the MSD result (Fig. 5-8A, *inset*).

Binding the DNA by H33342 did not substantially affect the diffusion behavior of NAC-1 NB, but the magnitudes of the directed motion lowered  $\sim 5$  times, which is estimated from the MSD values at time lag = 10 sec (Fig. 5-8C). Since a prolonged exposure to H33342 can cause cell death, this result suggested cells respond to the H33342 profoundly, and the change in the nucleus mobility may act as a significant marker to address the cell death.

The disruption of the actin cytoskeleton increased the MSD values of NAC-1 NB over all observed time lag (Fig. 5-8D). However, it was speculated that multiple mechanisms could be involved in this phenomenon. In short time lag, the MSD increase could be possibly caused from the reduction of the chromatin-NAC-1 NB interaction as previous discussed. As the time lag increased, disruption by the actin cytoskeleton seemingly became more prominent because the nucleus more easily moved within the cytoplasm due to the loss of anchorage to the actin cytoskeleton. Thus, the bulk motion

of the nucleus would cause a larger degree of movement of the NAC-1 NBs and this would explain the increased MSD over long lag time. Meanwhile, disruption of NOC (Fig. 5-8E) did not show a significant change in MSD, suggesting that the nuclear body dynamics and nucleus movement in the observation time period is less sensitive to the MT.

### 5.3 Discussion and Conclusion

In this chapter, I studied the dynamics of the oncogenic NAC-1 NBs to gain insights for chromatin-NAC1-NB interaction. The results suggested that the NAC-1 NBs are located in chromatin-poor regions or in the interchromatin area of the nucleus. Chromatin-NAC-1 NB interactions can be probed by NAC-1 NB tracking at the short time lag (0.1-0.3 sec). NAC-1 NB movement in longer time lag is more complicated since the bulk movement of the nucleus becomes a dominant factor for NAC-1 NB motion. The MSD of NAC-1 NB in short time lag suggested a sub-diffusive motion ( $\alpha \sim 0.5$ ), suggesting the chromatin-NAC-1 NB interaction can affect the motion of NAC-1 NBs. The sub-diffusive pattern of NAC-1 NB becomes weak with increasing time lag as the bulk motion of the nucleus takes over the local motion of NAC-1 NBs.

Drug treatment experiments suggested that the mobility of NAC-1 NB is governed by many factors, including the ATP level, the chromatin structure, the chromatin-NAC-1 NB interaction, and the integrity of the cytoskeleton. However, even though the data supported that the chromatin-NAC-1 NB interaction plays an important role in the NAC-1 dynamics, the association of chromatin and NAC-1 NB to gene regulation is unclear. Incorporating protein modification into this type approach could potentially yield more insight into this question.

The dynamic study of nuclear organelles implies a potential method to probe the chromatin architecture. However, nuclear organelles may not be ideal targets since their chemical properties and reactivity to chromatin may be mediated by several factors thereby complicating the mobility of nuclear organelles. To better characterize chromatin dynamics, it is desirable to bypass chemical interaction effects. This can be achieved by using an inert tracer, and microrheology may be used to estimate the mechanical properties of a nucleus. Though particles can be directly injected into the nucleus by microinjection, the nucleus may be damaged, which is difficult to identify. MX-1 protein possesses a nucleus-locating sequence and forms nuclear bodies with a crystal-like structure inside the nucleus<sup>5</sup>. A MX-1 protein mediated marker may offer a way to better examine the chromatin architecture.

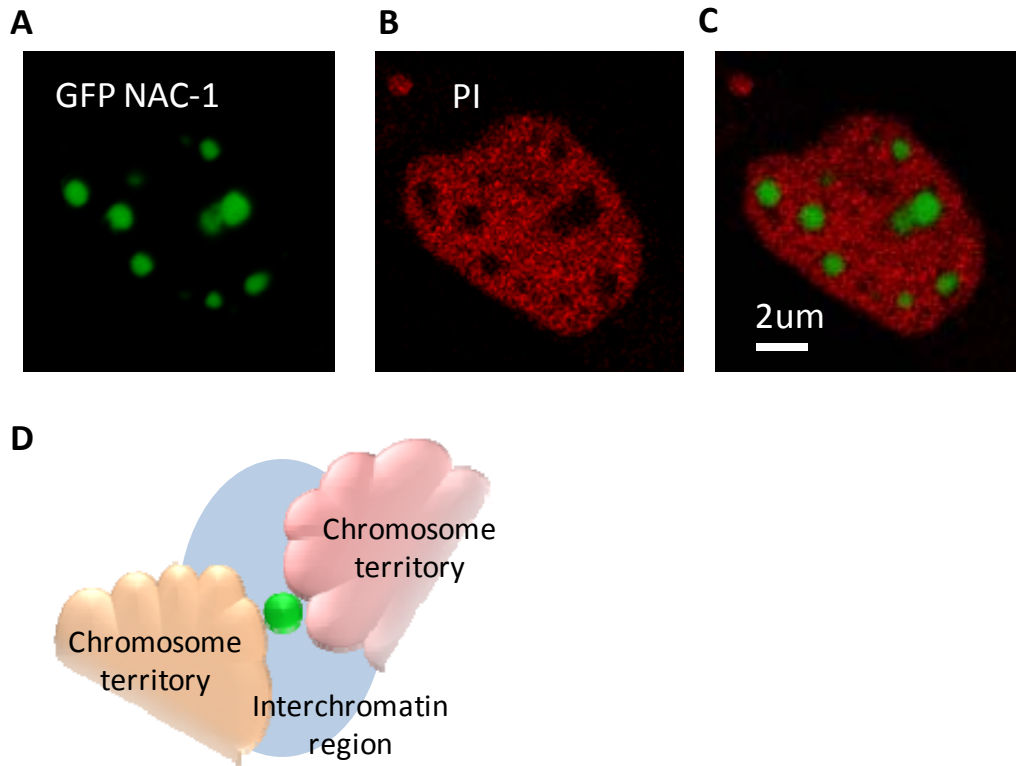


Figure 5-1. Fix and stain images show the location of NAC-1 NB in a nucleus. Confocal sections of GFP labeled NAC-1 NB (A), PI stained Chromatin (B), and the overlaid images (C) showing that the NAC-1 NB is located in chromatin-poor regions. (D) A cartoon demonstrates the NAC-1 NB location in the nucleus.

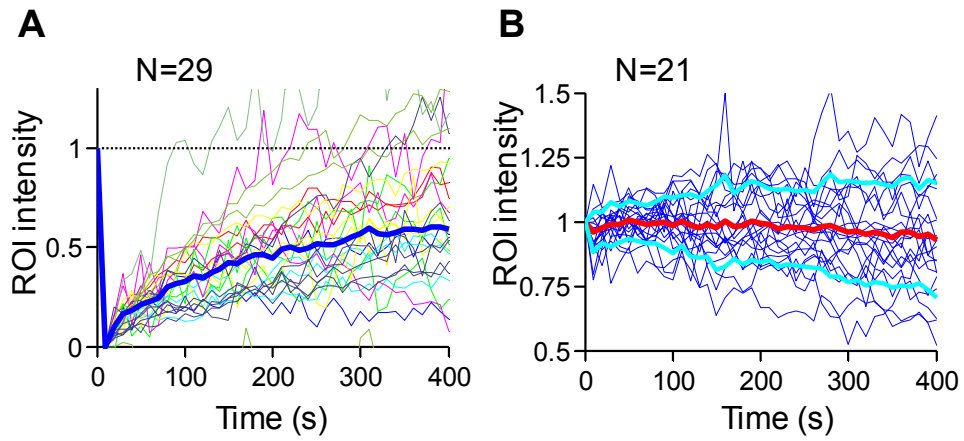


Figure 5-2. Dynamics structure of NAC-1 NBs was analyzed by Fluorescence recovery after Photobleaching. (A) NAC-1 NBs is bleached and its fluorescent Intensity in a 1 $\mu$ m \*1 $\mu$ m region of interest spot is measured over 400s. The thick blue line shows the mean of the recovery curve. (B) A control experiment shows no significant amount of fluorescence bleaching during the observation time period. The red line indicates the mean of intensity value over time.

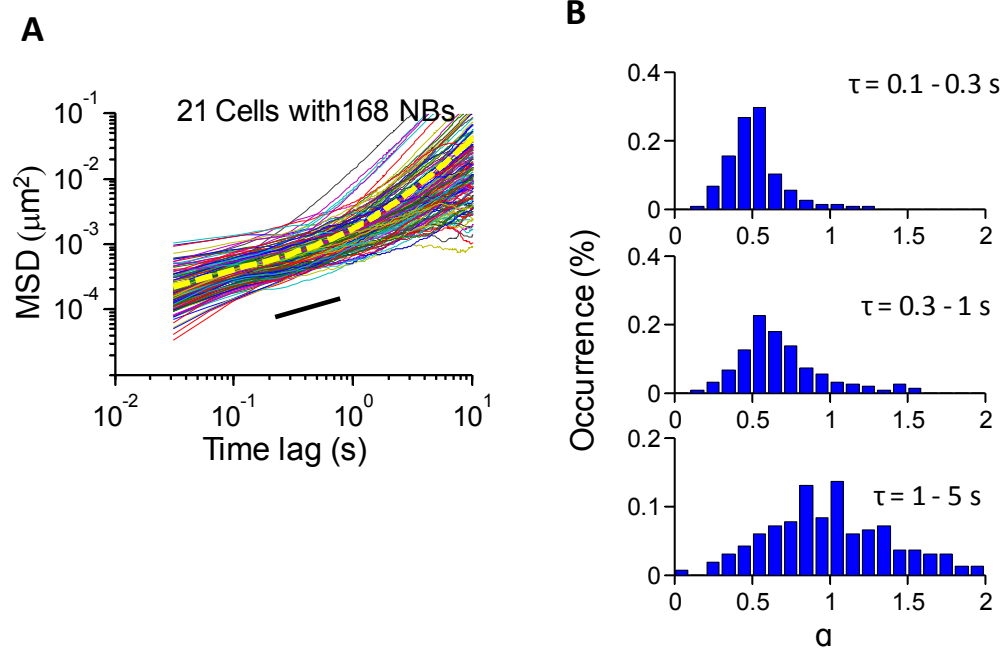


Figure 5-3. Characterization of NAC-1 NB dynamics from their MSD responses. (A) MSD result of NAC-1 NB (N=168) from 21 cells were plotted against the time lag. The yellow dashed line represents the mean value of MSD and the black line indicates an MSD slope of 0.5. (B) Histogram of subdiffusion coefficient ( $\alpha$ ) over different time lag ranges (from top to bottom, 0.1-0.3s, 0.3-1s, 1-5s) showing how the mean and distribution of  $\alpha$  increase with time lag.

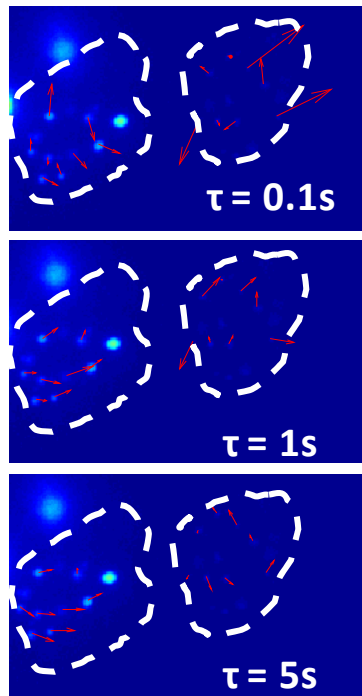


Figure 5-4. A vector map shows the NB Movement over three different time scales, 0.1s, 1s and 5s (from top to bottom). Synchronized NB movement is found in the same nucleus. Enclosed dash lines indicate the location of the nucleus.

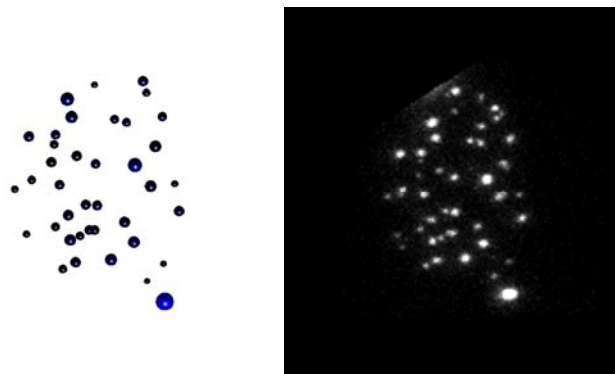


Figure 5-5. Reconstructed NAC-1 NB image (left) where the NB size represent the estimate of NAC-1 NBs size from wide filed z-stack images. The result agrees with the z-projection image from confocal microscopy (right).

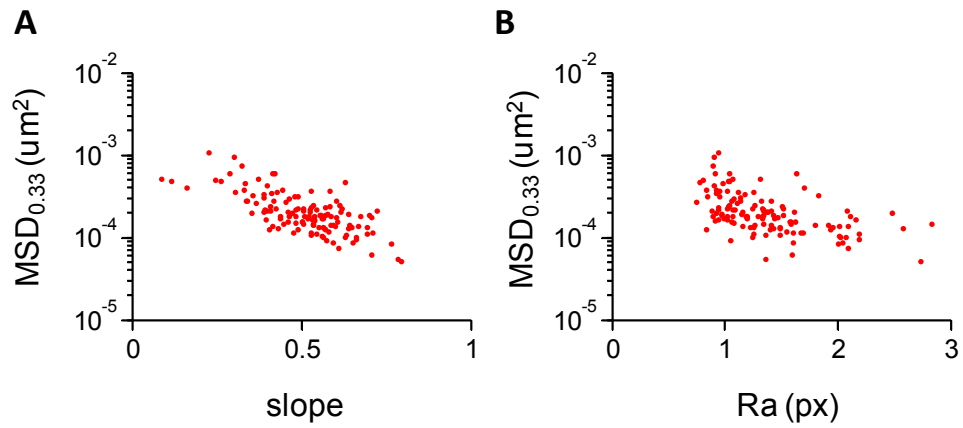


Figure 5-6. NAC-1 NB mobility is associated with its size (A) A scatter plot of MSD values at 0.33s and their slopes show that they are negatively correlated with a correlation coefficient of -0.6. (N=82). (B) MSD values are also negatively correlated with size. (correlation coefficient = -0.5)

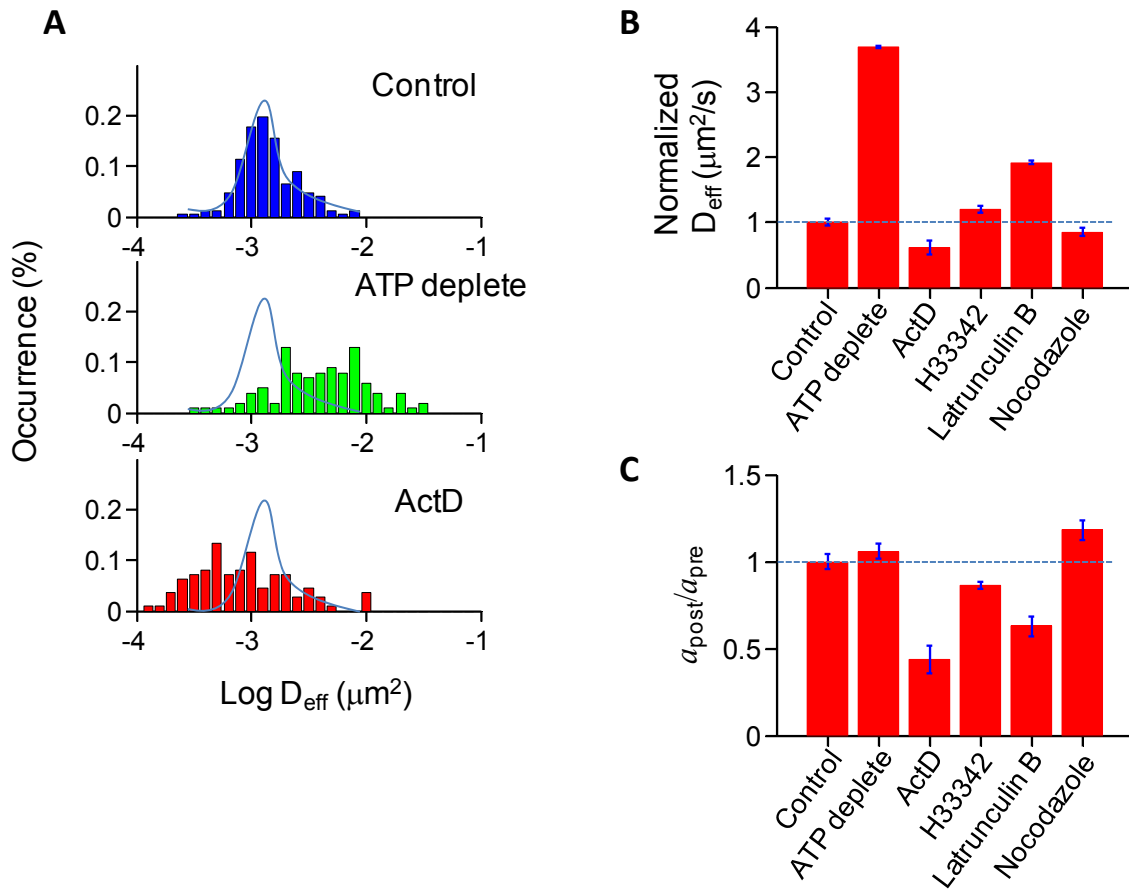


Figure 5-7. Drug treatment affects NAC-1 NB kinetics. (A) Effective diffusivity ( $\equiv \text{MSD}/4\tau$ ) of NAC-1 NB at 0.1s increases after ATP depletion but decreases in ActD treatment. The blue lines sketch the distribution of effective diffusivity in the control condition. (B) A bar plot shows the change of effective diffusivity after different drug treatments. The change in effective diffusivity is normalized to the control. (C) A bar plot shows the sub-diffusion coefficient change. The value is normalized by its sub-diffusion prior to treatment. Error bars represent the standard error of the mean.

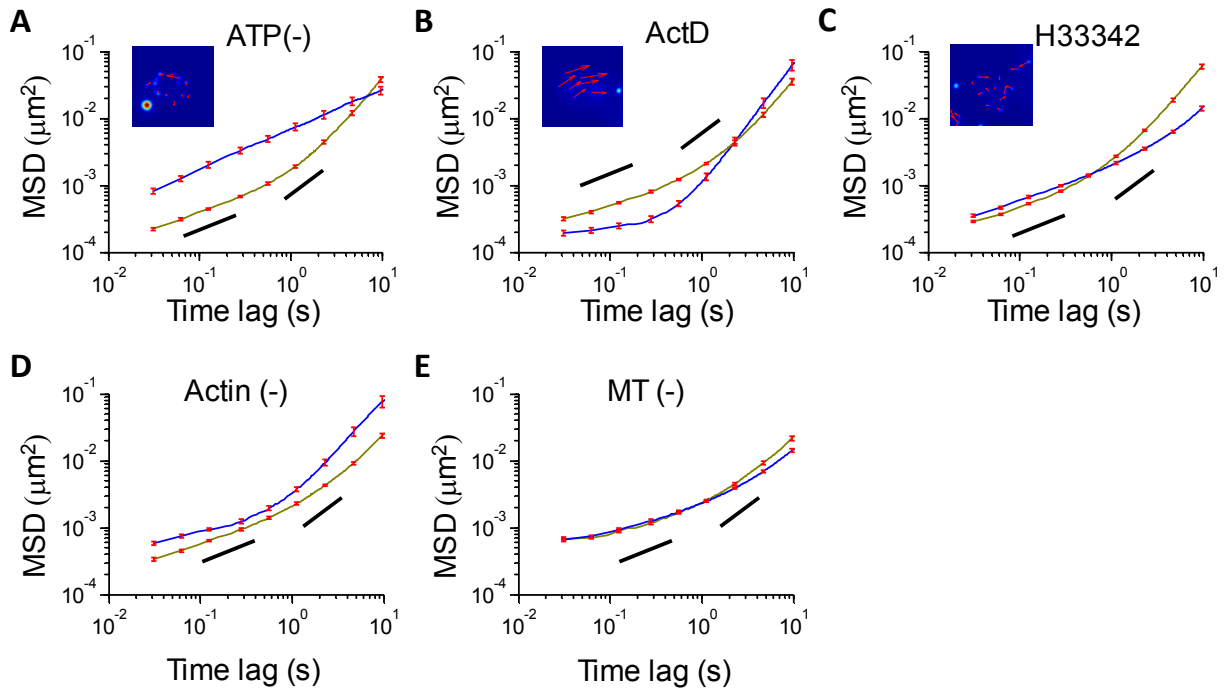


Figure 5-8. MSD plots show the NAC-1 NB dynamics over time in response to drug treatment. MSDs of NAC-1 NBs prior to (yellow) and after treatment (blue) with ATP depletion(A), ActD(B), H33342(C), latrunculin B (D) and nocodazole (E). Black bar indicate the slope of 0.5 and 1. Inset images in (A-C) show the typical movement of NB over 10 seconds after treatment. Error bars represent the standard error of the mean.

## CHAPTER 6 CONCLUSIONS

### **6.1 Accurate MSD Estimation in Video-Based Tracking**

MSD inaccuracy due to static error is ubiquitous in CCD camera-based particle tracking systems. However, the complex interplay between multiple tracking parameters had precluded the development of a practical method to minimize the errors. The correction approach explained herein significantly minimizes static error. This approach circumvents the complication of direct static error calculation by employing a simulation-based method to correct experimental particle tracking measurements. This considerably enhances the accuracy of the MSD and improves the subsequent estimation of diffusivity as well as rheological properties. This correction technique is not limited to the particular system used herein, but is broadly applicable to any tracking system. The transition to another system requires simple steps of determining the correlation between the pixel signal and noise, and appropriately selecting correct tracking parameters. By closely following the methodology described herein, static error can be significantly eliminated, leading to a greater clarity when interpreting the MSD values from a particle tracking experiment. In conclusion, this method greatly advances the application of single particle tracking in practice.

### **6.2 Optimizing Image Acquisition**

By thoroughly deciphering the photon sensing mechanism of the EM-CCD camera, I am able to successfully characterize the performance of this type of photon detector. Due to the various applications of an EM-CCD camera in addition to particle tracking, specific settings may be used to fulfill different demands. With an understanding of the performance of this photon detector, the resolution of image-based

biophysical methods can be assessed by the Monte Carlo method to find the optimum settings for subsequent experiments.

### **6.3 Optimum Estimation of Biophysical Properties**

The estimation of biophysical properties is always affected by noise that deviates observations from their true value. Obtaining an image using the optimum resolution decreases, but does not remove the noise from the image. Thus, biophysical properties estimated from images are consequently deviated from the true state. With an understanding of the noise within the measurement systems, I learn the effect of this noise on the resolution of biophysical property estimation by using a Monte Carlo method. This method is flexible and can be adapted to be suitable even when the image contains heterogeneous intensity values. The knowledge of the variation in real biophysical property estimations empowers us to make an optimum estimation from the observed set of noisy data. In this work, the observed noisy trajectory serves as an example to demonstrate that with the adequate model and estimate of position variation, the root mean square error of estimated positions can be significantly decreased. In another words, the resolution of a measured trajectory can increase by roughly three times. This method is very effective and I believe it can be further applied to the estimation of many other cellular properties.

### **6.4 Dynamics of Nuclear Organelles Associated with Chromatin Structure**

One popular scheme for the function of nuclear organelles is that they are involved in gene expression regulation by acting as a nuclear hub for protein storage. In this dissertation, I have examined the dynamics of a newly discovered nucleus body, NAC-1 NB, and have found that its dynamics are strongly related to the surrounding chromatin structure. These studies further show that the dynamics of NAC-1 NB are related to

various factors, including NB size, the association to chromatin, chromatin structure, and the cytoskeleton. Different drug treatments to the nucleus can induce different modulated effects, which can be successfully assessed by the MSD of NAC-1 NB. My results indicate that the NAC-1 NB is associated with chromatin in the inter-chromatin space. Through this investigation, I propose an alternative view of how the NB dynamics can contribute to gene expression regulation.

## LIST OF REFERENCES

1. Wieser, S., Moertelmaier, M., Fuerbauer, E., Stockinger, H. & Schutz, G.J. (Un)confined diffusion of CD59 in the plasma membrane determined by high-resolution single molecule microscopy. *Biophysical Journal* **92**, 3719-3728 (2007).
2. Saxton, M.J. & Jacobson, K. Single-particle tracking: Applications to membrane dynamics. *Annual Review of Biophysics and Biomolecular Structure* **26**, 373-399 (1997).
3. Lee, J.S.H. *et al.* Ballistic intracellular nanorheology reveals ROCK-hard cytoplasmic stiffening response to fluid flow. *Journal of Cell Science* **119**, 1760-1768 (2006).
4. Kole, T.P., Tseng, Y., Huang, L., Katz, J.L. & Wirtz, D. Rho kinase regulates the intracellular micromechanical response of adherent cells to rho activation. *Molecular Biology of the Cell* **15**, 3475-3484 (2004).
5. Gorisch, S.M. *et al.* Nuclear body movement is determined by chromatin accessibility and dynamics. *Proceedings of the National Academy of Sciences of the United States of America* **101**, 13221-13226 (2004).
6. Jin, S., Haggie, P.M. & Verkman, A.S. Single-particle tracking of membrane protein diffusion in a potential: Simulation, detection, and application to confined diffusion of CFTR Cl<sup>-</sup> channels. *Biophysical Journal* **93**, 1079-1088 (2007).
7. Cabal, G.G. *et al.* SAGA interacting factors confine sub-diffusion of transcribed genes to the nuclear envelope. *Nature* **441**, 770-773 (2006).
8. Apgar, J. *et al.* Multiple-particle tracking measurements of heterogeneities in solutions of actin filaments and actin bundles. *Biophysical Journal* **79**, 1095-1106 (2000).
9. Borgdorff, A.J. & Choquet, D. Regulation of AMPA receptor lateral movements. *Nature* **417**, 649-653 (2002).
10. Haft, D. & Edidin, M. Cell Biology - Modes of Particle-Transport. *Nature* **340**, 262-263 (1989).
11. Martin, D.S., Forstner, M.B. & Kas, J.A. Apparent subdiffusion inherent to single particle tracking. *Biophysical Journal* **83**, 2109-2117 (2002).
12. Savin, T. & Doyle, P.S. Static and dynamic errors in particle tracking microrheology. *Biophysical Journal* **88**, 623-638 (2005).

13. Thompson, R.E., Larson, D.R. & Webb, W.W. Precise nanometer localization analysis for individual fluorescent probes. *Biophysical Journal* **82**, 2775-2783 (2002).
14. Cheezum, M.K., Walker, W.F. & Guilford, W.H. Quantitative comparison of algorithms for tracking single fluorescent particles. *Biophysical Journal* **81**, 2378-2388 (2001).
15. Gonzalez, R.C. & Woods, R.E. *Digital image processing*, Edn. 2nd. (Prentice Hall, Upper Saddle River, N.J.; 2002).
16. McWhirter, I. Electron Multiplying CCDs - New Technology for Low Light Level Imaging. *Proceedings of 33rd Annual European Meeting on Atmospheric Studies by Optical Methods IRF Sci. Rep.*, **292**, 61-66 (2008).
17. Jonas, M., Huang, H., Kamm, R.D. & So, P.T. Fast fluorescence laser tracking microrheometry. I: instrument development. *Biophysical journal* **94**, 1459-1469 (2008).
18. Chen, Y., Muller, J.D., So, P.T. & Gratton, E. The photon counting histogram in fluorescence fluctuation spectroscopy. *Biophysical journal* **77**, 553-567 (1999).
19. Yildiz, A., Tomishige, M., Vale, R.D. & Selvin, P.R. Kinesin walks hand-over-hand. *Science (New York, N. Y)* **303**, 676-678 (2004).
20. Unruh, J.R. & Gratton, E. Analysis of molecular concentration and brightness from fluorescence fluctuation data with an electron multiplied CCD camera. *Biophysical journal* **95**, 5385-5398 (2008).
21. Hyneczek, J. Impactron-a new solid state image intensifier. *IEEE Transactions on Electron Devices* **48**, 2238-2241 (2001).
22. Detmer, S.A. & Chan, D.C. Functions and dysfunctions of mitochondrial dynamics. *Nat Rev Mol Cell Biol* **8**, 870-879 (2007).
23. Saftig, P. & Klumperman, J. Lysosome biogenesis and lysosomal membrane proteins: trafficking meets function. *Nat Rev Mol Cell Biol* **10**, 623-635 (2009).
24. Etienne-Manneville, S. & Hall, A. Rho GTPases in cell biology. *Nature* **420**, 629-635 (2002).
25. Goldberg, M.B. & Theriot, J.A. Shigella flexneri surface protein IcsA is sufficient to direct actin-based motility. *Proceedings of the National Academy of Sciences of the United States of America* **92**, 6572-6576 (1995).
26. Hua, W., Young, E.C., Fleming, M.L. & Gelles, J. Coupling of kinesin steps to ATP hydrolysis. *Nature* **388**, 390-393 (1997).

27. Bianco, P.R. & Kowalczykowski, S.C. Translocation step size and mechanism of the RecBC DNA helicase. *Nature* **405**, 368-372 (2000).
28. Murphy, C.T., Rock, R.S. & Spudich, J.A. A myosin II mutation uncouples ATPase activity from motility and shortens step size. *Nature cell biology* **3**, 311-315 (2001).
29. Kural, C. *et al.* Kinesin and dynein move a peroxisome in vivo: a tug-of-war or coordinated movement? *Science (New York, N.Y)* **308**, 1469-1472 (2005).
30. Kocks, C. *et al.* L. monocytogenes-induced actin assembly requires the actA gene product, a surface protein. *Cell* **68**, 521-531 (1992).
31. Southwick, F.S. & Purich, D.L. Arrest of *Listeria* movement in host cells by a bacterial ActA analogue: implications for actin-based motility. *Proceedings of the National Academy of Sciences of the United States of America* **91**, 5168-5172 (1994).
32. Levi, V., Ruan, Q., Plutz, M., Belmont, A.S. & Gratton, E. Chromatin dynamics in interphase cells revealed by tracking in a two-photon excitation microscope. *Biophysical journal* **89**, 4275-4285 (2005).
33. van der Schaar, H.M. *et al.* Characterization of the early events in dengue virus cell entry by biochemical assays and single-virus tracking. *Journal of virology* **81**, 12019-12028 (2007).
34. Brandenburg, B. & Zhuang, X. Virus trafficking - learning from single-virus tracking. *Nat Rev Microbiol* **5**, 197-208 (2007).
35. Ruan, G., Agrawal, A., Marcus, A.I. & Nie, S. Imaging and tracking of tat peptide-conjugated quantum dots in living cells: new insights into nanoparticle uptake, intracellular transport, and vesicle shedding. *Journal of the American Chemical Society* **129**, 14759-14766 (2007).
36. Wieser, S., Moertelmaier, M., Fuerbauer, E., Stockinger, H. & Schutz, G.J. (Un)confined diffusion of CD59 in the plasma membrane determined by high-resolution single molecule microscopy. *Biophysical journal* **92**, 3719-3728 (2007).
37. Salman, H. *et al.* Nuclear localization signal peptides induce molecular delivery along microtubules. *Biophysical journal* **89**, 2134-2145 (2005).
38. Xu, J.Y., Tseng, Y., Carriere, C.J. & Wirtz, D. Microheterogeneity and microrheology of wheat gliadin suspensions studied by multiple-particle tracking. *Biomacromolecules* **3**, 92-99 (2002).
39. Mason, T.G., Ganesan, K., vanZanten, J.H., Wirtz, D. & Kuo, S.C. Particle tracking microrheology of complex fluids. *Physical review letters* **79**, 3282-3285 (1997).

40. Apgar, J. *et al.* Multiple-particle tracking measurements of heterogeneities in solutions of actin filaments and actin bundles. *Biophysical journal* **79**, 1095-1106 (2000).
41. Kole, T.P., Tseng, Y., Huang, L., Katz, J.L. & Wirtz, D. Rho kinase regulates the intracellular micromechanical response of adherent cells to rho activation. *Molecular biology of the cell* **15**, 3475-3484 (2004).
42. Lee, J.S. *et al.* Ballistic intracellular nanorheology reveals ROCK-hard cytoplasmic stiffening response to fluid flow. *Journal of cell science* **119**, 1760-1768 (2006).
43. Panorchan, P., Lee, J.S., Kole, T.P., Tseng, Y. & Wirtz, D. Microrheology and ROCK signaling of human endothelial cells embedded in a 3D matrix. *Biophysical journal* **91**, 3499-3507 (2006).
44. Zarchan, P. & Musoff, H. *Fundamentals of Kalman filtering: a practical approach*, Edn. 3. (American Institute of Aeronautics and Astronautics, Reston, VA; 2009).
45. Ramachandra, K. *Kalman Filtering Techniques for Radar Tracking*. (Marcel Dekker, New York, NY; 2000).
46. Ionides, E.L., Fang, K.S., Isseroff, R.R. & Oster, G.F. Stochastic models for cell motion and taxis. *Journal of mathematical biology* **48**, 23-37 (2004).
47. Adams, M.D. *et al.* Complementary-DNA Sequencing - Expressed Sequence Tags and Human Genome Project. *Science* **252**, 1651-1656 (1991).
48. Berezney, R., Malyavantham, K.S., Pliss, A., Bhattacharya, S. & Acharya, R. Spatio-temporal dynamics of genomic organization and function in the mammalian cell nucleus. *Advances in Enzyme Regulation, Vol 45* **45**, 17-26 (2005).
49. Branco, M.R. & Pombo, A. Chromosome organization: new facts, new models. *Trends in Cell Biology* **17**, 127-134 (2007).
50. Cremer, T. & Cremer, C. Chromosome territories, nuclear architecture and gene regulation in mammalian cells. *Nature Reviews Genetics* **2**, 292-301 (2001).
51. Lamond, A.I. & Earnshaw, W.C. Structure and function in the nucleus. *Science* **280**, 547-553 (1998).
52. Egger, G., Liang, G.N., Aparicio, A. & Jones, P.A. Epigenetics in human disease and prospects for epigenetic therapy. *Nature* **429**, 457-463 (2004).
53. Handwerger, K.E. & Gall, J.G. Subnuclear organelles: new insights into form and function. *Trends in Cell Biology* **16**, 19-26 (2006).

54. Gruenbaum, Y., Margalit, A., Goldman, R.D., Shumaker, D.K. & Wilson, K.L. The nuclear lamina comes of age. *Nature Reviews Molecular Cell Biology* **6**, 21-31 (2005).
55. Zhong, S., Salomoni, P. & Pandolfi, P.P. The transcriptional role of PML and the nuclear body. *Nature Cell Biology* **2**, E85-E90 (2000).
56. Laptenko, O. & Prives, C. Transcriptional regulation by p53: one protein, many possibilities. *Cell Death and Differentiation* **13**, 951-961 (2006).
57. Rideout, W.M., Eggan, K. & Jaenisch, R. Nuclear cloning and epigenetic reprogramming of the genome. *Science* **293**, 1093-1098 (2001).
58. Grewal, S.I.S. & Moazed, D. Heterochromatin and epigenetic control of gene expression. *Science* **301**, 798-802 (2003).
59. Lyko, F. & Brown, R. DNA methyltransferase inhibitors and the development of epigenetic cancer therapies. *Journal of the National Cancer Institute* **97**, 1498-1506 (2005).
60. Hong, Q.A., Sheetz, M.P. & Elson, E.L. Single-Particle Tracking - Analysis of Diffusion and Flow in 2-Dimensional Systems. *Biophysical Journal* **60**, 910-921 (1991).
61. Reibel, Y., Jung, M., Bouhifd, M., Cunin, B. & Draman, C. CCD or CMOS camera noise characterisation. *European Physical Journal-Applied Physics* **21**, 75-80 (2003).
62. Xu, J.Y., Viasnoff, V. & Wirtz, D. Compliance of actin filament networks measured by particle-tracking microrheology and diffusing wave spectroscopy. *Rheologica Acta* **37**, 387-398 (1998).
63. Speidel, M., Jonas, A. & Florin, E.L. Three-dimensional tracking of fluorescent nanoparticles with subnanometer precision by use of off-focus imaging. *Optics Letters* **28**, 69-71 (2003).
64. Kole, T.P., Tseng, Y., Jiang, I., Katz, J.L. & Wirtz, D. Intracellular mechanics of migrating fibroblasts. *Molecular Biology of the Cell* **16**, 328-338 (2005).
65. Eskiw, C.H., Dellaire, G., Mymryk, J.S. & Bazett-Jones, D.P. Size, position and dynamic behavior of PML nuclear bodies following cell stress as a paradigm for supramolecular trafficking and assembly. *Journal of cell science* **116**, 4455-4466 (2003).
66. Gerencser, A.A., Doczi, J., Torocsik, B., Bossy-Wetzel, E. & Adam-Vizi, V. Mitochondrial swelling measurement in situ by optimized spatial filtering: astrocyte-neuron differences. *Biophysical journal* **95**, 2583-2598 (2008).

67. Gorisch, S.M. *et al.* Nuclear body movement is determined by chromatin accessibility and dynamics. *Proceedings of the National Academy of Sciences of the United States of America* **101**, 13221-13226 (2004).
68. Levitan, E.S., Lanni, F. & Shakiryanova, D. In vivo imaging of vesicle motion and release at the Drosophila neuromuscular junction. *Nature protocols* **2**, 1117-1125 (2007).
69. Bakal, C., Aach, J., Church, G. & Perrimon, N. Quantitative morphological signatures define local signaling networks regulating cell morphology. *Science (New York, N.Y)* **316**, 1753-1756 (2007).
70. Benoit, M., Gabriel, D., Gerisch, G. & Gaub, H.E. Discrete interactions in cell adhesion measured by single-molecule force spectroscopy. *Nature cell biology* **2**, 313-317 (2000).
71. Fink, G. *et al.* The mitotic kinesin-14 Ncd drives directional microtubule-microtubule sliding. *Nature cell biology* **11**, 717-723 (2009).
72. Zhang, L., Neves, L., Lundeen, J.S. & Walmsley, I.A. A Characterization of the Single-photon Sensitivity of an Electron Multiplying Charge-Coupled Device. *J. Phys. B: At. Mol. Opt. Phys.* **42**, 114011 (2009).
73. Robbins, M.S. & Hadwen, B.J. The noise performance of electron multiplying charge-coupled devices. *IEEE Transactions on Electron Devices* **50**, 1227-1232 (2003).
74. Li, S. *et al.* Identification of GW182 and its novel isoform TNGW1 as translational repressors in Ago2-mediated silencing. *Journal of cell science* **121**, 4134-4144 (2008).
75. Wu, P.H., Arce, S.H., Burney, P.R. & Tseng, Y. A novel approach to high accuracy of video-based microrheology. *Biophysical journal* **96**, 5103-5111 (2009).
76. Savin, T. & Doyle, P.S. Static and dynamic errors in particle tracking microrheology. *Biophysical journal* **88**, 623-638 (2005).
77. Gonzalez, R.C. & Woods, R.E. *Digital Image Processing*, Edn. 2nd. (Prentice Hall, Upper Saddle River, NJ; 2002).
78. Reibel, Y., Jung, M., Bouhifd, M., Cunin, B. & Draman, C. CCD or CMOS Camera Noise Characterisation. *Eur. Phys. J. AP* **21**, 75-80 (2003).
79. Mullikin, J.C. *et al.* Methods For CCD Camera Characterization. *SPIE Image Acquisition and Scientific Imaging Systems* **2173**, 73-84 (1994).

80. Weidtkamp-Peters, S. *et al.* Dynamics of component exchange at PML nuclear bodies. *Journal of cell science* **121**, 2731-2743 (2008).
81. Kannan, B. *et al.* Spatially resolved total internal reflection fluorescence correlation microscopy using an electron multiplying charge-coupled device camera. *Analytical chemistry* **79**, 4463-4470 (2007).
82. Imafuku, Y., Toyoshima, Y.Y. & Tawada, K. Fluctuation in the microtubule sliding movement driven by kinesin in vitro. *Biophysical journal* **70**, 878-886 (1996).
83. Gibbons, F., Chauwin, J.F., Desposito, M. & Jose, J.V. A dynamical model of kinesin-microtubule motility assays. *Biophysical journal* **80**, 2515-2526 (2001).
84. Kalman, R.E. A new approach to linear filtering and prediction problems *Journal of Basic Engineering* **82**, 35-45 (1960).
85. Coy, D.L., Wagenbach, M. & Howard, J. Kinesin takes one 8-nm step for each ATP that it hydrolyzes. *The Journal of biological chemistry* **274**, 3667-3671 (1999).
86. Howard, J., Hunt, A.J. & Baek, S. Assay of microtubule movement driven by single kinesin molecules. *Methods in cell biology* **39**, 137-147 (1993).
87. Ramachandran, S., Ernst, K.H., Bachand, G.D., Vogel, V. & Hess, H. Selective loading of kinesin-powered molecular shuttles with protein cargo and its application to biosensing. *Small (Weinheim an der Bergstrasse, Germany)* **2**, 330-334 (2006).
88. Leduc, C., Ruhnnow, F., Howard, J. & Diez, S. Detection of fractional steps in cargo movement by the collective operation of kinesin-1 motors. *Proceedings of the National Academy of Sciences of the United States of America* **104**, 10847-10852 (2007).
89. Nitta, T. & Hess, H. Dispersion in active transport by kinesin-powered molecular shuttles. *Nano letters* **5**, 1337-1342 (2005).
90. Tawada, K. & Sekimoto, K. Protein friction exerted by motor enzymes through a weak-binding interaction. *Journal of theoretical biology* **150**, 193-200 (1991).
91. Tawada, K. & Sekimoto, K. A physical model of ATP-induced actin-myosin movement in vitro. *Biophysical journal* **59**, 343-356 (1991).
92. Sekimoto, K. & Tawada, K. Extended time correlation of in vitro motility by motor protein. *Physical review letters* **75**, 180-183 (1995).
93. Imafuku, Y., Toyoshima, Y.Y. & Tawada, K. Monte Carlo study for fluctuation analysis of the in vitro motility driven by protein motors. *Biophysical chemistry* **59**, 139-153 (1996).

94. Imafuku, Y., Emoto, Y. & Tawada, K. A protein friction model of the actin sliding movement generated by myosin in mixtures of MgATP and MgGTP in vitro. *Journal of theoretical biology* **199**, 359-370 (1999).
95. Sekimoto, K. & Tawada, K. Fluctuations in sliding motion generated by independent and random actions of protein motors. *Biophysical chemistry* **89**, 95-99 (2001).
96. Stengel, R.F. in *Stochastic optimal control: Theory and application* pp. 400 (Wiley, New York, NY; 1986).
97. Lee, J.S. *et al.* Nuclear lamin a/c deficiency induces defects in cell mechanics, polarization, and migration. *Biophysical journal* **93**, 2542-2552 (2007).
98. Jaqaman, K. & Danuser, G. Computational image analysis of cellular dynamics: A case study based on particle tracking. *Cold Spring Harbor Protocol* **2009**, top65 (2009).
99. McMahon, M.D., Berglund, A.J., Carmichael, P., McClelland, J.J. & Liddle, J.A. 3D particle trajectories observed by orthogonal tracking microscopy. *ACS nano* **3**, 609-614 (2009).
100. Ershler, W.B. & Keller, E.T. Age-associated increased interleukin-6 gene expression, late-life diseases, and frailty. *Annual Review of Medicine* **51**, 245-270 (2000).
101. Baylin, S.B. & Ohm, J.E. Epigenetic gene silencing in cancer - a mechanism for early oncogenic pathway addiction? *Nature Reviews Cancer* **6**, 107-116 (2006).
102. Jones, P.A. & Baylin, S.B. The fundamental role of epigenetic events in cancer. *Nature Reviews Genetics* **3**, 415-428 (2002).
103. Jemal, A. *et al.* Cancer statistics, 2007. *Ca-a Cancer Journal for Clinicians* **57**, 43-66 (2007).
104. Nakayama, K. *et al.* A BTB/POZ protein, NAC-1, is related to tumor recurrence and is essential for tumor growth and survival. *Proceedings of the National Academy of Sciences of the United States of America* **103**, 18739-18744 (2006).
105. Jinawath, N. *et al.* NAC-1, a potential stem cell pluripotency factor, contributes to paclitaxel resistance in ovarian cancer through inactivating Gadd45 pathway. *Oncogene* **28**, 1941-1948 (2009).
106. Nakayama, K., Nakayama, N., Wang, T.L. & Shih, I.M. NAC-1 controls cell growth and survival by repressing transcription of Gadd45GIP1, a candidate tumor suppressor. *Cancer Research* **67**, 8058-8064 (2007).

107. Bernardi, R. & Pandolfi, P.P. Structure, dynamics and functions of promyelocytic leukaemia nuclear bodies. *Nature Reviews Molecular Cell Biology* **8**, 1006-1016 (2007).
108. Kakizuka, A. *et al.* Chromosomal Translocation T(15-17) in Human Acute Promyelocytic Leukemia Fuses Rar-Alpha with a Novel Putative Transcription Factor, Pml. *Cell* **66**, 663-674 (1991).
109. JaresErijman, E.A. *et al.* Binding of actinomycin D to single-stranded DNA. *Nucleosides & Nucleotides* **16**, 661-667 (1997).

## BIOGRAPHICAL SKETCH

Pei-Hsun was born in 1981 in Kaohsiung, Taiwan. The younger of two children, he grew up mostly in Kaohsiung, graduating from Kaohsiung Senior High School in 1999. He earned his B.S. in Chemical Engineering from the National Taiwan University (NTU) in 2003. From 2003 to 2004, he served as soldier in Taiwan Army and until 2005 he worked for Samsung Corporation as salesmen to develop the international solar cell business.

In 2005 fall, he enrolled in the Ph.D. program in the Department of Chemical Engineering at University of Florida. He joined Dr. Yiider Tseng's research group and focused on development of high throughput method in characterizing and study the living cell in real time. He earned his Doctor of Philosophy degree in chemical engineering in May 2010. He had more than 5 presentations in conferences. He is an author or coauthor of more than 4 papers published in peer-reviewed journals.